MAPPING AND UNDERSTANDING THE MEAN SURFACE CIRCULATION OF THE NORTH ATLANTIC: INSIGHTS FROM NEW GEODETIC AND OCEANOGRAPHIC MEASUREMENTS

by

Simon Higginson

Submitted in partial fulfillment of the requirements
for the degree of Doctor of Philosophy

at

Dalhousie University
Halifax, Nova Scotia
May 2012

DALHOUSIE UNIVERSITY

DEPARTMENT OF OCEANOGRAPHY

The undersigned hereby certify that they have read and recommend to the Faculty of Graduate Studies for acceptance a thesis entitled "MAPPING AND UNDERSTANDING THE MEAN SURFACE CIRCULATION OF THE NORTH ATLANTIC: INSIGHTS FROM NEW GEODETIC AND OCEANOGRAPHIC MEASUREMENTS" by Simon Higginson in partial fulfillment of the requirements for the degree of Doctor of Philosophy.

Dated: May 7, 2012

External Examiner: _____

Research Supervisor: _____

Examining Committee: _____

_____

_____

_____

Departmental Representative: _____

DALHOUSIE UNIVERSITY

DATE: May 7, 2012

AUTHOR: Simon Higginson

TITLE: MAPPING AND UNDERSTANDING THE MEAN SURFACE CIRCULATION OF THE NORTH ATLANTIC: INSIGHTS FROM NEW GEODETIC AND OCEANOGRAPHIC MEASUREMENTS

DEPARTMENT OR SCHOOL: Department of Oceanography

DEGREE: PhD CONVOCATION: October YEAR: 2012

_____

Signature of Author

To Catherine and the boys

TABLE OF CONTENTS

LIST OF TABLES

LIST OF FIGURES

ABSTRACT

The mean dynamic topography (MDT) of the ocean is closely related to the mean surface circulation. The objective of this thesis is to produce estimates of the MDT for the North Atlantic using newly available data from ocean and gravity observing systems, to evaluate these new estimates and so improve our understanding of the circulation.

Oceanographic estimates of the MDT are based on the mean temperature and salinity (TS) fields of the ocean. These are typically averages from sparse observations collected over many decades. The ocean is a non-stationary system so it is more appropriate to define the mean for shorter, specific periods. Whilst the Argo observing system has increased the frequency and resolution of in situ oceanographic measurements, high frequency (eddy) variability remains. A new technique is described for removing this variability using satellite altimeter measurements of the sea surface height. A new TS mean is produced, relating to the period from 2000 to 2007, and this is used to map a new oceanographic estimate of the MDT using an ocean circulation model.

New geodetic estimates of the MDT are produced using geoid models that incorporate gravity measurements from the ongoing GRACE and GOCE satellite missions. These are compared with the new oceanographic estimate and validated against independent observations such as drifter speeds. The geodetic method produces realistic estimates of the mean surface circulation, thereby realizing the long time dream of oceanographers to observe the ocean circulation from space. The new oceanographic estimates are not as accurate, but the new TS mean contributes to improvements in the performance of ocean models, a necessary step in understanding and predicting the oceans.

Coastal tide gauges can provide an accurate estimate of the alongshore tilt of the coastal MDT and this has been used to evaluate the above estimates. Temporal variability of the tilt along the coast of the South Atlantic Bight is used, with statistical methods and an ocean circulation model, to identify the processes contributing to the tilt. A new opportunity to use tide gauges as part of an observing system for the ocean circulation is discussed.

LIST OF ABBREVIATIONS AND SYMBOLS USED

Abbreviation	Description
AC	Azores Current
ArcGP08	Arctic Gravity Project 2008
AVISO	Archiving, Validation and Interpretation of Satellite Oceanographic Data
CC	Canaries Current
CGG2010	Canadian Gravimetric Geoid Model 2010
CHAMP	Challenging Minisatellite Payload
CH96	*Cooper & Haines* [1996]
CORE	Common Ocean-Ice Reference Experiments
EGC	East Greenland Current
EGCC	East Greenland Coastal Current
EGM96	Earth Gravity Model 1996
Glorys2v1	Global Ocean Reanalysis 2 Version 1
GOCE	Gravity Field and Steady-State Ocean Circulation Explorer
GPS	Global Positioning System
GRACE	Gravity Recovery and Climate Experiment
GS	Gulf Stream
GSLSE	Gulf Stream Landward Surface Edge
GSS	Gulf Stream Separation
IC	Irminger Current
IS	Irminger Sea
LC	Labrador Current
LIM	Louvain-la-Neuve Sea Ice Model
LoC	Loop Current
MAB	Mid-Atlantic Bight
MDT	Mean Dynamic Topography
MSS	Mean Sea Surface
NAC	North Atlantic Current

Abbreviation	Description
NCAR	National Center for Atmospheric Research
NCEP	National Centers for Environmental Prediction
NEC	North Equatorial Current
NEMO	Nucleus for European Modelling of the Ocean
NRCan	Natural Resources Canada
OI	Optimal Interpolation
OPA	Ocean Parallelise
PCG08I	Preliminary Canadian Gravity Model 2008 Version I
RMS	Root Mean Square
SAB	South Atlantic Bight
SGB	Southern Grand Banks
TS	Temperature and Salinity
WGC	West Greenland Current
WOA	World Ocean Atlas
WOCE	World Ocean Circulation Experiment
WOD	World Ocean Database

Symbol	Description	Units
f	Coriolis Parameter	radians s^{-1}
$\mathcal{F}$	Combined Frictional Terms	
g	Gravitational Acceleration	9.8 ms^{-2}
G	Gravitational Constant	6.673 x 10^{11} $m^3kg^{-1}s^{-2}$
h	Steric Height	m
M	Mass of Earth	kg
N	Geoid Height	m
p	Pressure	Pa
r	Correlation Coefficient	
u	Meridional Velocity	ms^{-1}
v	Zonal Velocity	ms^{-1}
v_s	Specifc Volume	m^3kg^{-1}

Symbol	Description	Units
V	Gravitational Potential	J kg^{-1}
W	Geopotential	J kg^{-1}
Z	Geopotential Height Anomaly	m
η	Sea Surface Height	m
η_a	Altimeter Sea Surface Height Anomaly	m
$\Delta\eta$	Alongshore Gradient of Sea Level	m $100km^{-1}$
γ	De-eddying Adjustment Factor	
Φ	Geopotential Anomaly	J kg^{-1}
ρ	Density	kg m^{-3}
ρ_0	Equilibrium Density	kg m^{-3}
σ	Standard Deviation	
δ	Specific Volume Anomaly	m^3kg^{-1}
ζ	Relative Vorticity	s^{-1}

ACKNOWLEDGEMENTS

I would like to thank Keith Thompson, my supervisor, for all of his help and encouragement during the past five years. I would also like to thank the members of my supervisory committee, Youyu Lu, Jianliang Huang and Markus Kienast, for their helpful comments and contributions.

A special thank you to Philip Woodworth, my external examiner, for making the trip from the UK for my defence. His comments and suggestions have helped to improve the work presented in this thesis.

Many other people have helped me along the way. Thank you to fellow graduate students, to the staff and Faculty of the Department of Oceanography and especially to my wife, Catherine.

Finally, this work would not have been possible without the data provided freely by a number of organizations including the Geodetic Survey Division of Natural Resources Canada, Aviso, the CLS Space Oceanography Division, the International Argo Project, the NOAA Earth Systems Research Laboratory, myOcean and the Global Drifter Program.

CHAPTER 1

INTRODUCTION

Mapping the mean circulation of the world's oceans is one of the fundamental challenges of physical oceanography. An understanding of the mean circulation is required, for example, to study transports of heat, salt, ice and pollutants, and the mean circulation can be used to assess the accuracy of ocean models. The mean surface circulation forms an important part of the three dimensional ocean circulation, and the circulation at depth can be mapped by combining the mean surface circulation with an estimate of the hydrographic structure.

The North Atlantic has probably been studied and instrumented more intensively than any other ocean basin, yet some aspects of the mean circulation are still poorly defined. Some regions are difficult to observe in winter because of ice, and the ocean's interior has been measured less than the surface ocean and coastal seas. The sparse in situ measurements only provide a snapshot of the circulation and unresolved temporal and spatial variability may be aliased or otherwise misrepresented in the mean.

New observation platforms are providing measurements with better, and more uniform, temporal and spatial resolution. For example, satellite altimeters and satellite gravity missions are improving our understanding of the height of the ocean surface and of the geoid. Drifting profilers of the Argo network are producing unprecedented numbers of temperature and salinity measurements in the ocean's interior.

In this thesis these new measurements will be used to produce estimates of the mean dynamic topography (MDT) of the North Atlantic. Separate estimates will be produced based on the new oceanographic data and the new geodetic observations, both relating to

the relatively short period from 2000 to 2007 corresponding to the first 8 years of the Argo programme. Defining the mean for a short period such as this reduces the misrepresentation of low frequency variability. The new MDTs will then be used to estimate the geostrophic component of the mean surface circulation, and these new estimates will be compared with each other and with other estimates of the mean circulation. Ocean models and dynamical principles will be used to examine some of the physical processes involved.

These results will be used to gain an improved knowledge and understanding of the mean surface circulation. This will assist with future studies, for example providing an improved representation of the mean state that can be used to validate ocean circulation models.

1.1 The Mean Surface Circulation of the North Atlantic

For this thesis the North Atlantic is defined as the region north of a latitude of 20°N, including the Labrador and Irminger seas around Greenland, but not including the Norwegian and Greenland seas to the north and east of Iceland.

The dominant feature of the North Atlantic surface circulation is the Gulf Stream (Figure 1.1). This current system originates in the Gulf of Mexico as the Loop Current, fed by waters from the Caribbean Sea via the Yucatan Strait (e.g. *Auer* [1987]). The current passes through the Straits of Florida, often referred to as the Florida Current at this point, and then follows the continental slope of the east coast of the United States northwards. The current is fast, exceeding 1 ms^{-1} in places, and the water is relatively warm and saline. The mean transport is approximately 32 Sv (1 Sv equals 10^6 m^3s^{-1}) near Miami (*Meinen et al.* [2010]), increasing to 85 Sv further north near Cape Hatteras. The path of the Gulf Stream along this coastline is constrained by topography, but near Cape Hatteras the current moves offshore into deeper waters and the path becomes more variable with meanders and eddies.

Beyond the tail of the Grand Banks the Gulf Stream becomes known as the North Atlantic Current. Part of the flow separates to form the Azores Current, which flows eastward and feeds recirculations to the south and west, such as the Canaries Current and

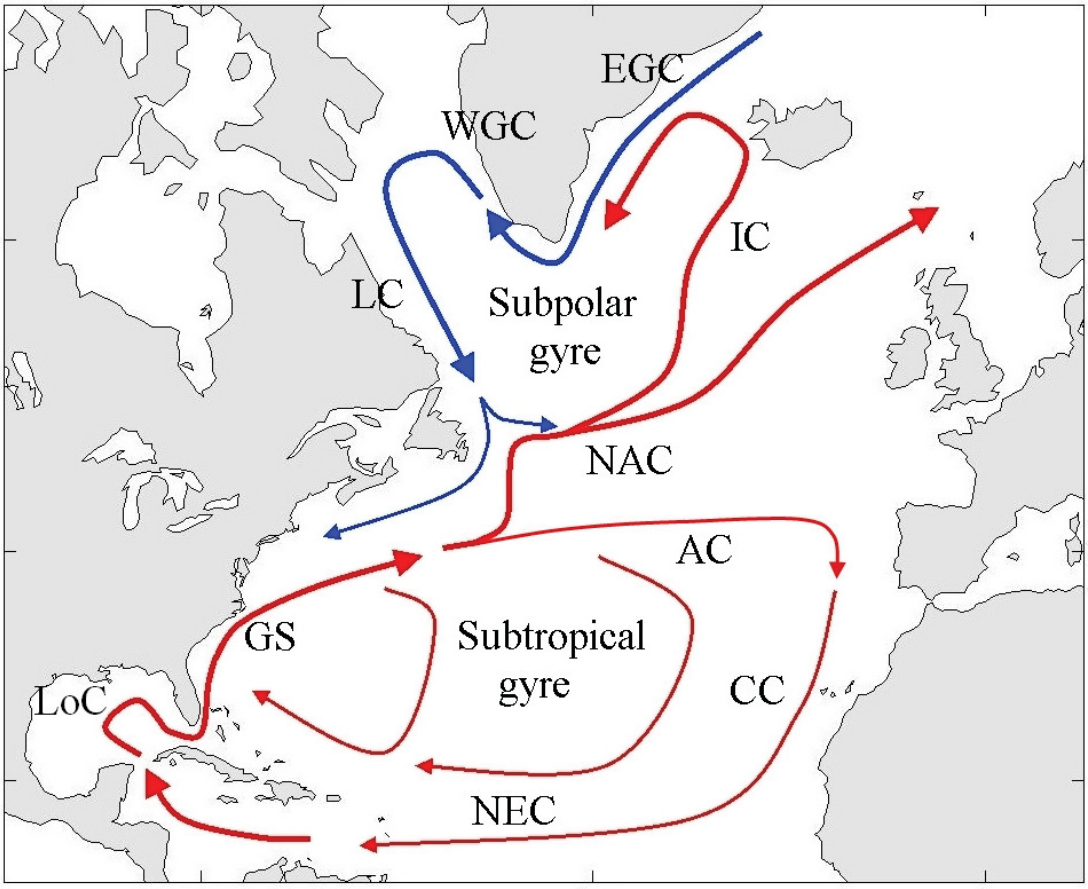

Figure 1.1: Schematic of the surface circulation of the North Atlantic. The relatively warm currents are shown in red, the cold currents in blue. The currents that are labelled are the Gulf Stream (GS), the Loop Current (LoC), the North Atlantic Current (NAC), the Azores Current (AC), the Canaries Current (CC), the North Equatorial Current (NEC), the Irminger Current (IC), the East Greenland Current (EGC), the West Greenland Current (WGC) and the Labrador Current (LC).

the North Equatorial Current. These waters rejoin the Gulf Stream, either north of the Florida Straits or via the Caribbean Sea, completing the circulation that is the subtropical gyre (e.g. *Reid* [1994]). The remainder of the North Atlantic Current continues north-eastwards, either toward the Norwegian Sea or into the subpolar gyre circulation. This circulation comprises the Irminger Current toward Iceland, with return flow equatorward via the East and West Greenland and Labrador currents (e.g. *Heywood et al.* [1994]). Current speeds in this circulation tend to be 0.5 ms^{-1} or less with transport in the Labrador Current for example of approximately 11 Sv (*Lazier and Wright* [1993]).

This description of the surface circulation, describing the system as largely closed, is a simplification. There are significant exchanges with other ocean basins, and a loss of water to the deep ocean through convection in the Labrador and Greenland seas.

More detailed descriptions of the Gulf Stream and the subpolar gyre are given in later chapters.

1.2 Mapping the Mean Circulation

Aspects of the surface circulation of the North Atlantic, such as the fast-moving Gulf Stream, were described as early as the 16th Century (*Stommel* [1972]). By the middle of the 20th Century the surface circulation had been mapped from hydrographic and velocity measurements (for example, *Sverdrup et al.* [1942]), with a description of the mean currents that is broadly similar to the modern picture. Subsequent hydrographic surveys have improved the resolution of hydrographic data and the associated circulation estimates. For example, the $\frac{1}{4}^{\circ}$ temperature and salinity (TS) climatologies of Levitus (*Boyer et al.* [2005]), constructed using a database of hundreds of thousands of TS profiles collected over more than a century, is used to calculate the mean dynamic height and the mean circulation. Other observational studies have mapped the circulation using surface drifters (e.g. *Fratantoni* [2001], *Reverdin et al.* [2003]) and using a variety of satellite remote sensing techniques (for example, using geodetic data (e.g. *Jayne* [2006]), using satellite altimeter and scatterometer data (e.g. *Sudre and Morrow* [2008]), and combining geodetic data with surface drifter data, (e.g. *Maximenko et al.* [2009])).

Each of the methods used to map the mean circulation has limitations. In situ measurements, such as hydrographic profiles, tend to have poor resolution and inhomogeneous coverage in time and space (e.g. *Bingham and Haines* [2006]). Drifters have increased spatial resolution but inhomogeneous sampling will remain. There may be temporal and spatial bias to drifter measurements, for example caused by sporadic release of drifters and restrictions to movement by sea ice, and corrections are needed to account for the effect of wind on the drifter. Satellite remote sensing methods greatly increase the spatial and temporal resolution of surface measurements but the resolution may still be insufficient to resolve smaller circulation features, and satellite instruments are unable to measure the ocean's interior.

The mean circulation defined by any of these methods is the sample mean, and it will depend on the observation period and the resolution of the observations. The ocean is a non-stationary system. *Wunsch* [1981] showed that sea level records, for example, are dominated by low frequency variability with periods ranging from the mesoscale to decadal and longer (Figure 1.2). *Levitus et al.* [2005] and others have demonstrated a secular increase in ocean temperature, probably associated with atmospheric warming. The sample mean of such a non-stationary system will depend on the time period of the observations, varying from one period to another. There is also high frequency variability in the ocean. Variability at higher frequencies and shorter lengthscales than the observation resolution may be aliased as lower frequency or longer lengthscale variability. This error can be reduced by increasing the temporal and spatial resolution of observations, but there is a limit to the increase possible with each technology.

1.3 The Mean Dynamic Topography of the Ocean

The mean dynamic topography was used to produce some of the earliest maps of the surface circulation. For example *Sverdrup et al.* [1942] included maps of the surface circulation for the North Atlantic, produced from dynamic height relative to a deep level where the current was assumed to be zero. The dynamic heights were calculated from hydrographic data, attributing the method to Georg Wüst's work in the Florida Current

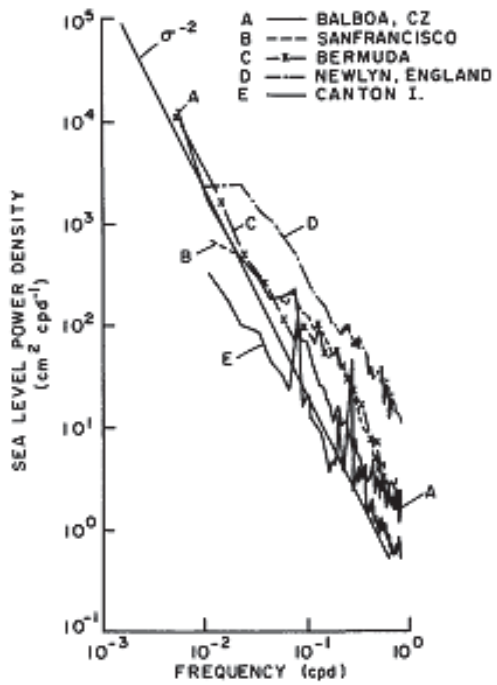

Figure 1.2: Spectra from a few representative sea level records (from *Wunsch* [1981], figure 11.5A)

published in 1924. Whilst measurements of current speed in the open ocean were sparse, mostly based on ship drift data, TS profiles were more readily available. Direct current measurements are now more common but spatial and temporal resolution remains relatively poor and the MDT remains a useful tool for estimating the circulation.

In simple terms the MDT is the difference between the actual mean sea surface and sea level if the ocean is at rest. This difference is associated with the currents, the gradients of the MDT being proportional to the mean surface geostrophic circulation. The MDT can be estimated geodetically or inferred from oceanographic data, and this is described in more detail below.

1.3.1 The Geodetic Method

The geoid can be considered as the level of equal gravitational potential which best approximates global sea level at rest. (This is discussed in more detail in Chapter 2 and Appendix A.) Although the geoid cannot be measured directly, it can be estimated using

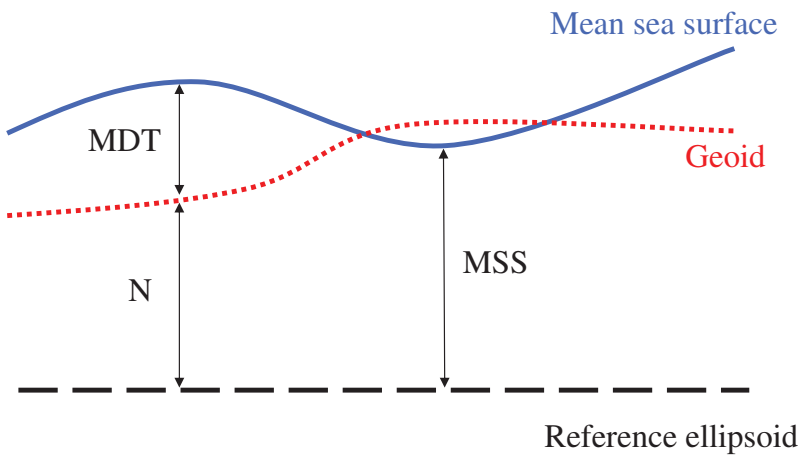

Figure 1.3: An illustration of the relationship between the geoid height (N), the mean sea surface height (MSS), the reference ellipsoid and the mean dynamic topography(MDT).

gravity and/or satellite altimeter measurements. Since the geoid approximates sea level at rest, MDT is given by

$$MDT = MSS - N \tag{1.1}$$

where N is the geoid height, and MSS is the mean sea surface height that can be measured by satellite altimeters. Each of these surfaces is defined relative to a reference ellipsoid, an idealized representation of the Earth's shape. The relationship between these surfaces is illustrated in Figure 1.3.

Spatial variations of the geoid are $\mathcal{O}$(100 m) with respect to the reference ellipsoid. The mean sea surface varies by a similar amount, with most of this variability attributable to the geoid. The residual MDT is 2 orders of magnitude smaller, $\mathcal{O}$(1 m), so both the MSS and the geoid must be measured with errors less than 1% or the errors will be larger than the MDT signal (*Bingham et al.* [2008]).

Satellite altimeter missions have been measuring sea surface height since the 1980's. A continuous record exists since 1992 incorporating measurements from a series of satellite missions including TOPEX/POSEIDON, ERS-1, ERS-2, Envisat, Jason-1 and Jason-2. Accuracy of these measurements is, for example, around 5 cm for the TOPEX/POSEIDON instrument (*Fu et al.* [1994]), which is sufficiently accurate to be useful for calculating a meaningful MDT.

Prior to the launch of dedicated low-orbit gravity mission satellites, geoid models were not sufficiently accurate to allow a useful MDT to be calculated for half-wavelengths below about 1000 km (*Johannessen et al.* [2003]), except for a few areas where the density of terrestrial gravity measurements was high. The GRACE satellite gravity mission was launched in 2002, followed in 2009 by the GOCE mission. These missions were designed to map the gravity field in unprecedented detail, with a target geoid accuracy of 1-2 cm at 100 km lengthscales for the GOCE mission (e.g., *Rummel et al.* [2011]). This has opened the door to using the direct geodetic method to produce an accurate MDT and estimate of the circulation. Such MDTs can be compared with oceanographic data to identify any areas of concern in the geoid model.

A limitation of the geodetic method is that the altimeter derived mean sea surface has higher errors in areas within 50 km or so of the coastline because of land contamination in the signal and the inaccuracy of geophysical corrections (*Bouffard et al.* [2008]). This limits the usability of the geodetically-determined MDT in this important coastal region, and restricts our ability to assess the accuracy of the geoid model.

1.3.2 The Oceanographic Method

The simplest method to calculate the MDT from oceanographic measurements is to calculate dynamic height relative to a given pressure level using TS profile measurements. *Gill* [1982] defines dynamic height as the geopotential anomaly (Φ) between two pressure surfaces

$$-\Phi = \int_0^p \delta \, dp \tag{1.2}$$

where δ is the specific volume anomaly. This is calculated as

$$\delta = v_s(S, T.p) - v_s(35, 0, p) \tag{1.3}$$

where v_s is the specific volume ($v_s = \rho^{-1}$), and the second term uses a salinity of 35 and a temperature of 0°C. The units of Φ are $\mathrm{m^2 s^{-2}}$, but it is usually converted to a geopotential height anomaly, Z, with units of m, using

$$Z = g^{-1} \int_0^p \delta \, dp \tag{1.4}$$

Geopotential or dynamic height tends to be used interchangeably with steric height, h, given by (e.g. *Talley et al.* [2011])

$$h = \int_0^z \delta\rho_0 \, dz \tag{1.5}$$

where ρ_0 is a reference density. Equation (1.5) is similar to (1.2) but the integration is between two depths rather than two pressure surfaces. The units of steric height are m, and the value of steric height is essentially the same as dynamic height using these definitions.

The reference level, p (or z), is usually chosen to be sufficiently deep that it may be assumed that the currents at that level are negligible. Then the surface geostrophic currents are proportional to the gradients of geopotential anomaly

$$u_g = -\frac{1}{f}\frac{\partial\Phi}{\partial x} \qquad v_g = \frac{1}{f}\frac{\partial\Phi}{\partial y} \tag{1.6}$$

or, similarly, to the gradients of steric height.

Whilst this method has been widely used, the assumption of a deep level of no motion is not necessarily correct, and the method cannot be used in waters shallower than the deep reference level p.

A more sophisticated approach, and one which is explored in this thesis, is to derive mean dynamic height by incorporating the mean TS fields into an ocean model. This does not require the assumption of a level of no motion, and allows the estimates to be extended into shallower water. The simplest method is to prescribe the model density field from observations, an approach described as the diagnostic method (e.g. *Holland and Hirschman* [1972]). *Sarmiento and Bryan* [1982] noted that the results from the diagnostic method are very sensitive to slight errors in the observed density field, and they developed a refinement of the method, the robust diagnostic approach, whereby the model density field is nudged toward the observations. *Thompson et al.* [2006] further developed this idea with an approach which they called spectral nudging. The model is nudged toward climatological TS values in the climatologically-important frequency bands, but allowed to evolve prognostically in other frequency bands. This reduces the bias and drift to which models are prone because of, for example, inadequate resolution and poor boundary

conditions. The spectral nudging has the advantage of not suppressing eddy activity, hence allowing nonlinear dynamics to contribute to the mean state. In this thesis an ocean model that incorporates spectral nudging is used to produce estimates of the MDT based on TS climatologies.

Both the dynamic height method and the ocean model method require an estimate of the mean TS fields from the observations i.e. a climatology. As previously noted, the ocean is a non-stationary system and the sample mean will vary with the observation period. Existing TS climatologies, such as the global $\frac{1}{4}^{\circ}$ World Ocean Atlas 2001 climatology (*Boyer et al.* [2005]), are based on observations collected over many decades, and low frequency variability may be incorrectly represented in such a climatology. Such errors will be propagated through the MDT and mean circulation produced using the climatology. An estimate of the mean that relates to a shorter, specific time period will reduce the misrepresentation of low frequency variability in the MDT, but oceanographic observations have, until recently, been too sparse to produce such an estimate.

1.4 New Data and Techniques

New observation platforms have been deployed in the past decade which provide oceanographic measurements at a higher spatial and temporal resolution than previously, and geodetic measurements at a higher accuracy than previously. The potential benefits are two-fold. Firstly both geodetic and oceanographic estimates of the MDT and the circulation should be more accurate than earlier estimates. Secondly the estimates can be related to a specific decadal period, thereby reducing the misrepresentation of low frequency variability associated with estimates that relate to longer time periods.

Geodetic data: Gravity measurements from the GRACE and GOCE satellite missions have been used to produce geoid models with much lower errors than previous models. The errors are of similar magnitude to the sea surface height errors of satellite altimeters, and it is now feasible to directly estimate the MDT and the mean circulation using the geodetic method. This is a benefit to the geodetic community as well as oceanographers since the geoid models can be evaluated by comparing the MDTs with oceanographic

estimates. Once a geoid model is validated it is feasible to use it with time-varying altimeter measurements to track the time-dependent surface circulation.

Oceanographic data: A range of new ocean observation technologies have been deployed in recent years, including floats, profilers, gliders and "bioprobes" (marine animals with sensors attached). Of particular interest for defining the mean state of the ocean is the Argo network of autonomous profiling floats which measure TS profiles to a maximum depth of 2000 m (*Roemmich et al.* [2000]). The first floats were deployed in 2000 with full deployment of a network of 3000 floats by 2007. The network now measures approximately 100,000 TS profiles each year . Whilst this number is small compared to the total of approximately 7 million records in the World Ocean Database 2005 (WOD05, *Boyer et al.* [2006]), the Argo sampling is more spatially homogeneous and the measurements extend to greater depths than many of the WOD05 records. This new dataset, less than 12 years of data in total, provides an ideal opportunity to develop a TS climatology relating to a much shorter period than conventional climatologies. This new climatology can then be used to estimate the MDT and the mean circulation specific to the Argo observation period. An added benefit is that it is possible to quantify any increase in the heat content of the ocean between previous TS climatologies and a new Argo-period one. One problem with this approach is that all measured TS profiles may have been perturbed by mesoscale activity such as eddies. This source of error is reduced by temporal averaging in climatologies derived from many decades of observations. A climatology based on fewer observations over a shorter time period will likely include larger errors, so a new approach is required to correct the observations for this mesoscale variability.

It has been noted earlier that geodetically-determined MDTs are unreliable in the coastal zone because of errors in the altimeter sea surface height measurements. This limits our ability to examine the mean circulation in nearshore regions, and to validate the geoid models. However alternative sea surface height data are available from coastal tide gauges and, combined with the ocean models that are used to estimate the oceanographic MDT, there is an opportunity to map and understand the mean circulation in the economically-important coastal zone.

1.5 Objectives and Outline of Thesis

The overall objective of this thesis is to use newly available oceanographic and geodetic data to improve the mapping of, and our understanding of, the mean surface circulation of the North Atlantic. To achieve this overall objective, this study has been designed to:

1. Improve estimates of the mean state of the temperature salinity (TS) structure of the North Atlantic over the Argo period.

2. Improve oceanographic and geodetic estimates of the MDT and the mean circulation for the Argo period.

3. Evaluate and understand the new estimates of the mean circulation.

4. Validate the new geoid model using oceanographic data.

5. Quantify and understand the coastal expression of MDT, and explore the use of coastal tide gauge measurements for ocean circulation monitoring.

The structure of the thesis is as follows. The method for constructing a geodetic MDT is described in Chapter 2. In Chapter 3 a new method is described for correcting Argo profiles for eddy variability, and the adjusted Argo data are used to construct a new TS climatology. This new climatology is used with the oceanographic MDT method described in Chapter 4, using both the dynamic height and ocean model approaches. The new geodetic and oceanographic estimates of the mean circulation of the subpolar gyre are mapped and discussed in Chapter 5. A similar analysis is undertaken for the subtropical gyre and Gulf Stream region in Chapter 6. In Chapter 7 the coastal expression of MDT is examined using tide gauge measurements close to the Gulf Stream in the South Atlantic Bight, and an ocean model is used to investigate the processes contributing to the observed signal. A summary of the main conclusions of this study is presented in Chapter 8.

CHAPTER 2

A GEODETIC MEAN DYNAMIC TOPOGRAPHY

The geodetic approach outlined in Chapter 1 is the most direct method for estimating the mean dynamic topography. The MDT is defined as the difference between the mean sea surface and the geoid height (Equation 1.1) but, since the MDT is two orders of magnitude smaller than both of these fields, this requires that the geoid model and the mean sea surface are both accurate to within a few centimetres. Until recently large-scale geoid models could not be defined to this level of accuracy, but the launch of a series of satellite gravity missions has changed this. In this chapter new geoid models from Natural Resources Canada, which incorporate both terrestrial and satellite gravity data, are used to produce estimates of the MDT for the North Atlantic and the associated estimates of the mean surface geostrophic circulation.

2.1 The Geoid

The first of the fields required to calculate the MDT geodetically is the geoid, which is a level of equal gravity potential. Such a level is "horizontal" in the sense that, at any point, local gravity is directed perpendicular to it. There are infinite equipotential levels, and the geoid is one that approximates mean sea level over the oceans (*Li and Götze* [2001]). Gravity can be expressed as

$$\vec{g} = \nabla W \tag{2.1}$$

where W is the potential of gravity (*Heiskanen and Moritz* [1967]), and the geoid is a surface of constant W (W_0). The gravity potential can be decomposed as

$$W = V + \Phi \tag{2.2}$$

where V is the gravitational potential due to the Earth's mass, and Φ is the centrifugal potential. The centrifugal potential varies only with latitude and radial distance from the centre of the Earth, whereas the gravitational potential varies spatially (because of density differences) as well as with radial distance.

2.1.1 Determining the Geoid

The gravity potential and hence the geoid is derived from measurements of gravity. The first global models were derived during the 1940's and 1950's from sparse terrestrial measurements of $\vec{g}$ using gravimeters (*Amalvict and Boavida* [1993]). Gradually the density of terrestrial measurements increased, with the development of ship- and air plane-mounted gravimeters. However the global coverage of measurements was inhomogeneous.

Terrestrial measurements were supplemented from the 1970's onwards with satellite tracking data. Satellite orbits are perturbed by variations in Earth's gravity, so orbit tracking provides information on the gravity field, particularly at long wavelengths ($>$500 km). For example, the EGM1996 geoid model (*Lemoine et al.* [1998]) incorporates measurements from satellite laser ranging of satellites such as LAGEOS, LAGEOS-2, Starlette and Stella.

In 2000 a dedicated low-orbit satellite gravity mission was launched (CHAMP) followed by two further missions (GRACE and GOCE). These are described further in section 2.1.3.

In this study the geoid is used with a mean sea surface to estimate the MDT. A number of issues must be considered when defining a geoid model to ensure that it is comparable with the mean sea surface field.

2.1.1.1 The Permanent Tides

The Earth is subject to gravitational forces from the Sun and the Moon, and measurements of gravity will be influenced by these additional forces. Although these forces vary on Earth with time, resulting in the Earth and Ocean tides, the time average is not zero. These permanent tides can be accounted for in three different ways - the mean tide system, the zero tide system and the tide-free system.

The mean tide system includes the additional gravitational potential in the gravity field and the geoid. This includes both the direct effect of the external bodies and the indirect effects caused by the permanent deformation of the Earth (*Petit and Luzum* [2010]). This reflects the physical reality. The tide free system totally removes the tidal potential of external bodies, with both direct and indirect effects removed. The zero tide system removes only the direct effect of the external bodies i.e., the contribution from the deformation of the Earth is still present. A geoid defined in the tide free system will be approximately 15 cm lower at the equator and 25 cm higher at the poles compared to a geoid defined using the mean tide system. The three tide systems are readily convertible (e.g. *Ekman* [1989]).

2.1.1.2 The Reference Ellipsoid

The geoid is defined relative to a reference ellipsoid, an equipotential ellipsoid of revolution which serves as an approximation of the geoid (*Li and Götze* [2001]). A number of different ellipsoids are in use for different geoid and satellite datasets, defined by the length of the semi-major axis, the geocentric gravitational constant, the dynamic form factor (related to the polar flattening of the ellipsoid) and the angular velocity of Earth.

2.1.1.3 Spherical Harmonics

The Earth's gravitational field is usually described in terms of spherical harmonics, analogous to a Fourier representation of a field on a plane. In spherical coordinates (r being the distance from the centre of the Earth, ϕ the latitude and λ the longitude) the spherical harmonic representation of the gravitational potential V for example is

$$V(r,\phi,\lambda) = \frac{GM}{r}\sum_{l=0}^{\infty}\left(\frac{R}{r}\right)^{l+1}\sum_{m=0}^{l}K_{l,m}Y_{l,m}(\phi,\lambda) \tag{2.3}$$

where G is the gravitational constant, M is the mass of the Earth, R is a scale factor, $Y_{l,m}$ are the real and complex spherical harmonics of degree l and order m, and $K_{l,m}$ are the complex numerical coefficients (*Hughes and Bingham* [2008], *Heiskanen and Moritz* [1967]).

For the purposes of this thesis the most important consequence of the use of spherical harmonics is for the interpretation of the resolution of a geoid model. For a given degree, l, the length scale or half wavelength D associated with spherical harmonics at that degree is given, in km, by

$$D = 20,000/l \tag{2.4}$$

A gravity or geoid model will be defined to a given degree and order, usually dependent on the resolution of the data used to construct the model. This half wavelength D provides a useful indication of the length scale of features that are resolved by the geoid model.

2.1.1.4 Errors

The geoid model contains errors of commission and errors of omission. The former are the errors associated with the measurement and processing methods i.e., the errors in the part of the geoid model that is resolved. An estimate of these errors may be provided with the geoid model. Errors of omission are errors in the part of the geoid model that is not resolved, such as features that are too small to be resolved by the maximum degree of the model.

2.1.2 Geoid Models from the Pre-Gravity Satellite Mission Era

The first global geoid models were produced using sparse terrestrial gravity measurements. For example the first global model computed using spherical harmonics was produced in 1952 to degree 8 (*Amalvict and Boavida* [1993]), a half wavelength of 2500 km. This may have contained errors of tens of metres because of the sparse data contributing to the analysis.

During the 1970's and 1980's there was an increase in the density of terrestrial gravity measurements, including surveys using ship-mounted and aircraft-mounted gravimeters. The new technique of measuring the gravity field by tracking perturbations in satellite

orbits was also introduced (*Rummel et al.* [2002]). For example the LAGEOS and Starlette satellites have been tracked using laser ranging. Both of these developments resulted in an increase in the resolution and accuracy of global geoid models. Satellite tracking data provides useful information up to degree 40 (i.e., half wavelengths greater than 500 km), whilst the terrestrial data provides the short wavelength information. *Rapp and Wang* [1993] analyzed several geoid models defined to degree 50 or better and found that differences were of the order of 30 cm over the oceans but more in some areas.

The next major development was to incorporate satellite altimeter measurements of the ocean surface, corrected for the mean dynamic topography. For example the EGM96 gravity model was produced using terrestrial gravity data, satellite tracking data and satellite altimeter measurements (*Lemoine et al.* [1998]). This model was defined to degree 360 (half wavelength 55 km) with typical geoid accuracy over the oceans in the range 5-15 cm up to degree 70 (a half wavelength of 285 km). An issue with this approach is that an estimate of the MDT must be subtracted from the altimeter measurements to derive an estimate of the geoid, but the MDT is not accurately known without an initial estimate of the geoid.

Whilst these techniques increased the accuracy of geoid models, the errors were still large compared to the MDT signal.

2.1.3 Satellite Gravity Missions

Only limited improvements to models such as EGM96 were possible using improved terrestrial gravity measurements, tracking data and altimeter measurements. The next major advance in geoid modelling was the development of remote measurement of the gravity field using dedicated low-orbit gravity mission satellites. Since 2000 three such missions have been put into orbit. All three differ from regular remote sensing missions in that the observation method is passive, with the entire satellite (or satellites) functioning as the sensor.

The first mission was the CHAMP probe, launched in 2000. Designed as a proof-of-concept mission, it was the forerunner of the GRACE mission. CHAMP was positioned at

the relatively low altitude of 450 km to maximize the gravitational effects on its orbit. The satellite incorporated GPS positioning to detect orbit perturbations more accurately than possible using ground-based tracking, giving an estimate of total accelerations (*Reigber et al.* [2002]). An on-board accelerometer detected non-gravitational accelerations, such as drag, which are separated from the total accelerations to resolve the gravity field. The probe continued in orbit until 2010.

The GRACE mission was launched in 2002 and, although its intended lifetime was 5 years, it is still operating. The mission comprises twin satellites, each somewhat similar to the CHAMP satellite. The satellites are in an identical near-polar orbit at an altitude of approximately 500 km, separated by about 220 km (*Tapley et al.* [2004]). As with the CHAMP mission, each satellite incorporates GPS positioning and an on-board accelerometer to detect non-gravitational accelerations. However the GRACE satellites incorporate an inter-satellite microwave ranging system which measures the distance between the two satellites at a precision better than 10 μm. This contributes small scale orbit perturbation information, leading to more detailed measurements than using GPS tracking alone. The objective of the mission was to map the global gravity field every 30 days to degree/order 100 (a half wavelength of 200 km) with an accuracy of 2 cm, thereby tracking the temporal variability of the gravity field.

The GOCE mission was launched in March 2009 and orbits at an altitude of approximately 250 km, even lower than the previous missions. Like CHAMP and GRACE, the satellite incorporates GPS orbit tracking to provide the long wavelength information. Additionally the probe includes an electric ion propulsion system which compensates for non-gravitational forces, and an on-board gravity gradiometer (e.g. *Rummel et al.* [2011]). The gradiometer comprises three pairs of accelerometers, each pair separated by approximately 0.5 m and arranged along mutually orthogonal axes. These accelerometers measure the gradient of gravity along each axis, allowing improved accuracy of the gravity field recovery for short wavelengths. The mission objective was to produce a geoid model to degree/order 200 (a half-wavelength of 100 km) with an accuracy of 1-2 cm.

The accuracy of each of the three missions, expressed as a cumulative geoid error, is compared in Figure 2.1. GRACE produces the highest accuracy (i.e., lowest cumulative

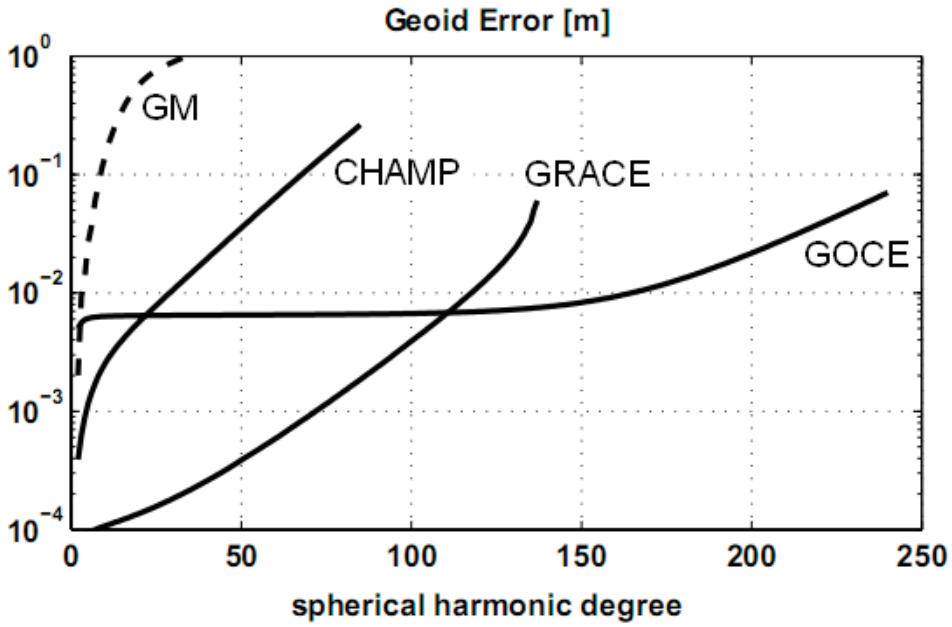

Figure 2.1: Comparison of the expected cumulative geoid error for idealized CHAMP, GRACE and GOCE satellite gravity missions (after *ESA* [1999]). The corresponding plot for a geoid derived from one of the best available satellite gravity models is also shown (dashed line, GM).

geoid error) at the long and medium length scales, improving accuracy by as much as 3 orders of magnitude, whilst GOCE contributes an improvement in accuracy at the shorter length scales.

2.1.4 Geoid Models from the Gravity Mission Era

An initial model produced using just 3 months of data from the first satellite gravity mission, CHAMP, yielded a geoid model with an accuracy of approximately 10 cm at degree/order 30 (the EIGEN-1S model, *Reigber et al.* [2002]). This solution was based solely on the CHAMP data, with no information from terrestrial gravity measurements or other sources. A later model incorporating 30 months of CHAMP data increased this level of accuracy to degree/order 55 (the EIGEN-3p model, *Reigber et al.* [2004]). The model is complete to degree/order 120 (a half wavelength of 167 km), but accuracy decreases with increasing degree/order.

The next mission, GRACE, was designed to study temporal variations of the gravity field but also yields data that can be used to construct a mean field. A number of geoid models

have been produced using the GRACE data. An early example, the EIGEN-GRACE02S model (*Reigber et al.* [2005]), is based on 110 days of GRACE data. The model is complete to degree/order 150 and geoid accuracy of 1 cm extends to degree/order 75 (a half wavelength of 267 km), a significant improvement over the best CHAMP and pre-CHAMP models. This accuracy improved with longer observation periods. For example the GGM02S model (*Tapley et al.* [2005]), complete to degree/order 160, increased the 1 cm accuracy to degree/order 95 (a half wavelength of 210 km). A number of models have been produced to higher degree/order by combining terrestrial gravity data with a GRACE solution. For example the EGM2008 model (*Pavlis et al.* [2012]) is complete to degree/order 2160.

The most-recent gravity mission, GOCE, is designed to yield a more-accurate mean solution at higher degree/order than the previous missions. *Pail et al.* [2011] described 3 solutions using 71 days of GOCE data, either independently or combined with GRACE and terrestrial measurements. They found a geoid accuracy of about 10 cm at degree/order 200 (a half wavelength of 100 km), and estimated that this will improve to 2-3 cm with the full mission dataset.

2.1.5 New North American Geoid Models

Thompson et al. [2009] used a North American regional geoid model to estimate the MDT of the North Atlantic. The geoid model was a combination of GRACE , altimeter and terrestrial data, with GRACE defining the geoid at long wavelengths and the terrestrial and altimeter data defining it at the shorter wavelengths. They compared the MDT and the associated surface geostrophic currents with oceanographic estimates and found generally good agreement. However they identified a number of spurious features in the geodetic MDT, such as high wavenumber variability south of Iceland.

In this study two improved North American geoid models produced by Natural Resources Canada will be used. The first (PCG08I) is similar to the one used by *Thompson et al.* [2009] but incorporates additional terrestrial gravity data and improved quality control. The second (CCG2010) additionally incorporates data from the GOCE mission.

2.1.5.1 The PCG08I Geoid Model

PCG08I (Preliminary Canadian Geoid Model 2008, version I) is one of a series of experimental geoid models developed at the Geodetic Survey Division of Natural Resources Canada (NRCan). This model covers all of North America (10-90°N, 170-10°W) but for regions away from Canadian territory and the neighbouring oceans NRCan relies on data provided by external international agencies such as the US National Geodetic Survey and the National Space Institute at the Technical University of Denmark.

The geoid model is produced using GRACE satellite gravity data, gravity derived from satellite altimetry and terrestrial gravity data. The GRACE data are introduced using the EGM2008 gravity model (*Pavlis et al.* [2012]), which is dominated by the GRACE contribution up to degree 90. Terrestrial gravity data include land observations from Canada and the United States, shipboard observations from the east coast of Canada, and airborne observations from around Greenland. These observations include data collected under the Arctic Gravity Project (ArcGP, http://earth-info.nga.mil/GandG/wgs84/agp/hist_agp.html). The realization of the marine gravity grid, and the computation of the geoid model from the gravity grid, is described in more detail in Appendix A. The geoid model is calculated on a grid with 1/30° spacing, and defined in the mean tide system.

The difference between the PCG08I geoid model and the one used by *Thompson et al.* [2009] exceeds 20 cm around the coast of Greenland (Figure 2.2), largely due to the use of newer ArcGP and altimeter-derived gravity grids. There are also large differences between the two geoids in the vicinity of the Gulf Stream, an area of oceanographic interest. The difference is only a few centimetres along the Canadian east coast, where basically the same terrestrial gravity dataset is used, representing an update from the new GRACE information in EGM2008.

The geoid errors for PCG08I range from a few centimetres to decimetres, but the total geoid error is mostly between 1 cm and 5 cm for the North Atlantic.

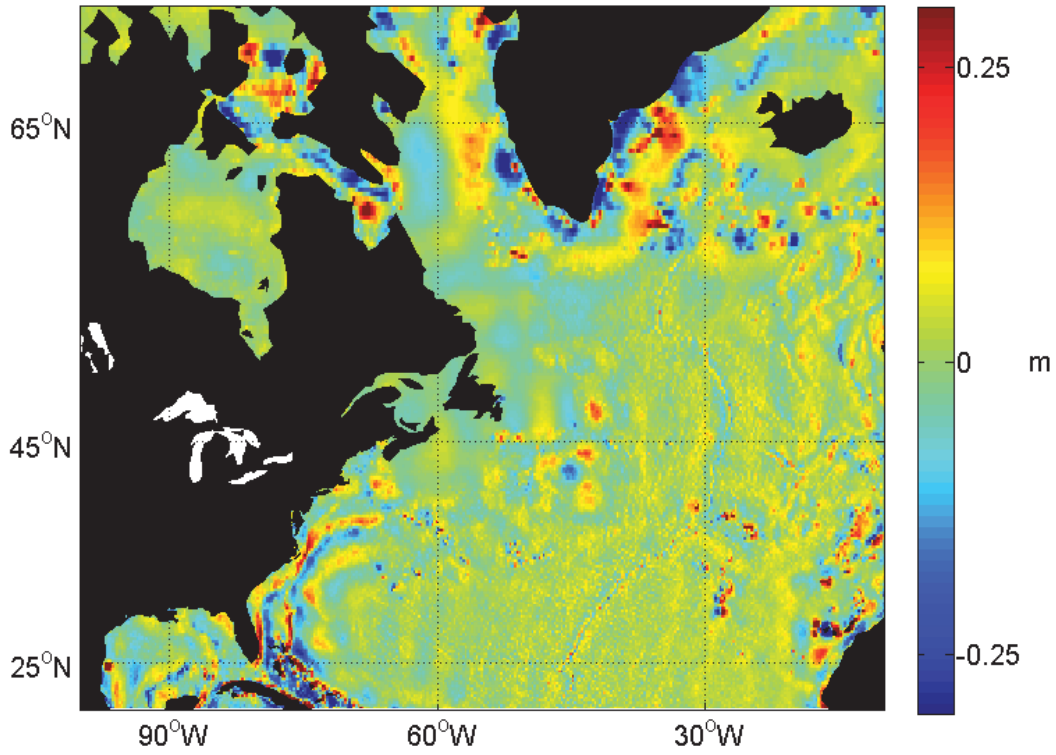

Figure 2.2: The height difference between the PCG08I geoid model, and the one used by *Thompson et al.* [2009].

2.1.5.2 The CGG2010 Geoid Model

CGG2010 (Canadian Gravimetric Geoid model 2010) is the latest public geoid model produced by NRCan. This model incorporates long wavelength components from a mean GRACE gravity model and the first cycle (2 months) of the GOCE mission, and short wavelength components incorporating the latest releases of marine and ArcGP gravity data.

The model is constructed in a similar manner to PCG08I, but the combined GRACE and GOCE satellite gravity model GOCO01S (*Pail et al.* [2010]) is incorporated into the solution. GOCO01S includes seven years of GRACE data and the first two months of GOCE gravity gradient measurements. The GRACE data is dominant up to degree 100 (a half wavelength of 200 km), and from degree 100 to 150 (a half wavelength of 130 km) the GOCE data contributes to the geoid. When GOCO01S is incorporated into the CGG2010 geoid the GOCE contribution is approximately limited to degree 120, a half wavelength of about 170 km. The GRACE and GOCE contribution is particularly useful for this study because it improves the accuracy of the resulting geoid model in regions further from Canada, where there are fewer terrestrial measurements to provide the high order detail. The differences from the PCG08I model (Figure 2.3) are mostly long wavelength corrections from the GRACE and GOCE data - unlike the differences shown in Figure 2.2, which are mostly short wavelength corrections from terrestrial gravity data.

2.2 The Mean Sea Surface

The second field required to calculate the MDT geodetically is the mean sea surface defined with respect to a reference ellipsoid. This is measured near-globally by satellite altimeters.

Satellite radar altimeters have been in orbit since the 1970's measuring the sea surface height relative to a reference ellipsoid (*Benveniste* [2011]). A continuous record exists since 1992 based on a number of missions including the TOPEX/Poseidon, ERS-1, ERS-2, Envisat, Jason-1 and Jason-2 satellites. The basic principle of satellite radar altimetry is that radar pulses are transmitted down from the satellite, and the distance between the satellite and the surface (the range) is measured by the time taken for the echo to be received back

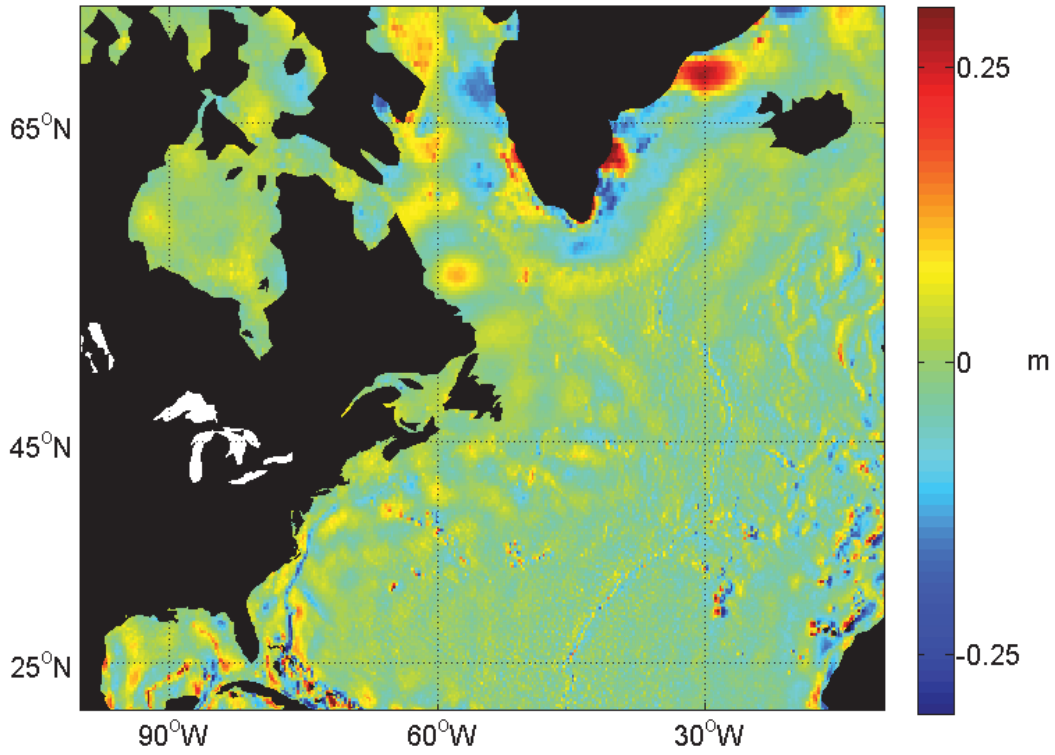

Figure 2.3: The height difference between the CGG2010 and the PCG08I geoid models.

at the instrument (e.g. *Wunsch and Stammer* [1998]). A number of corrections are required, which can broadly be classified as atmospheric refraction corrections, sea state bias corrections and external geophysical adjustments (e.g. *Chelton et al.* [2001]). Atmospheric refraction affects the travel time of the radar pulse and includes dry troposphere, wet troposphere and ionosphere refraction effects. Sea state bias relates to the bias of the altimeter range measurement toward the troughs of ocean waves. External geophysical adjustments include corrections for the effect of ocean tides and the inverse barometer effect. Typically satellite altimeters can measure sea surface height to an accuracy better than 5 cm (e.g. *Fu et al.* [1994]) but there are increased errors in coastal regions (50km or less from the coast) because of land contamination and problems with the atmospheric corrections, sea state bias corrections and geophysical adjustments (*Bouffard et al.* [2008]). The altimeter measures absolute height of the ocean relative to the reference ellipsoid, although values are more typically distributed as anomalies relative to a long term mean sea level.

The MSS_CNES_CLS10 mean sea surface product distributed by Aviso (Archiving, Validation and Interpretation of Satellite Oceanographic data, http://www.aviso.oceanobs.com/en/data/products/auxiliary-products/mss/index.html) is used for this study. This MSS combines 16 years of altimeter data referenced to the 1993-1999 period, and represents the geoid plus the MDT for this period. It is computed on a $\frac{1}{10}^{\circ}$ grid using altimeter data within a 200 km radius of each grid point. The resulting MSS, and an estimate of its error, are interpolated onto a nominal $\frac{1}{30}^{\circ}$ grid by Aviso. MSS values range from approximately -45 m to +70 m in the region of this study and the error estimate is typically less than 5 cm. Aviso relax the MSS toward an estimate of the geoid in the coastal zone (approximately 50 km from shore) because of the errors associated with satellite altimeter measurements near coastlines.

The altimeter measurements are adjusted from the original period (1993-1999) to the period 2000-2007 using

$$MSS_{00-07} = MSS_{93-99} + (\overline{\eta}_{00-07} - \overline{\eta}_{93-99}) \tag{2.5}$$

where $\overline{\eta}$ is the mean sea surface height anomaly from satellite altimeters for the period specified. This equation is similar to the MDT adjustment formula detailed, for example, by *Griesel et al.* [2012]. The reference period 2000-2007 is chosen because it corresponds with the reference period of the oceanographic estimate of MDT described in Chapter 4.

2.3 The Mean Dynamic Topography

The MDT is calculated by a subtraction of the new geoid model from the MSS_CNES_CLS10 mean sea surface adjusted to the 2000–2007 reference period. This subtraction can be undertaken in a pointwise manner, for gridded data, or spectrally, for data expressed in spherical harmonics (*Bingham et al.* [2008]). Here both the MSS and the geoid are expressed as gridded products and the pointwise method is used.

The MDT is mapped onto a $\frac{1}{4}^\circ$ grid by taking the mean of all values within $\pm\frac{1}{8}^\circ$ of each grid point. This resolution is chosen to correspond with the oceanographic estimate of MDT described in Chapter 4. The MSS is relaxed towards a geoid model in the coastal zone (50 km or approximately $\frac{1}{2}^\circ$ from shore, see above). For this study the MDT within approximately $\frac{1}{4}^\circ$ of the coastline is excluded, which is the region where the geoid model dominates. The resulting MDT is shown in Figure 2.4 for the PCG08I geoid model and in Figure 2.5 for the CGG2010 geoid model.

2.4 Evaluation of the New Geodetic Estimates

At the scales visible in Figures 2.4 and 2.5 there is little difference between the two estimates of MDT. The appearance of the topography is broadly as expected. The low of the cyclonic subpolar gyre is clearly visible to the south of Greenland, and the high associated with the warm waters of the subtropical gyre can be seen to the south of the domain. The path of the Gulf Stream can clearly be seen off the east coast of the United States, marked by the sharp boundary between red/orange colours and blue.

In order to undertake further evaluation of the MDTs it is useful to calculate the surface geostrophic speeds, which are proportional to the gradients of the MDT (see Equation 1.6). The gradients are calculated by differencing the MDT across $\pm\frac{1}{4}^\circ$ at each gridpoint. The

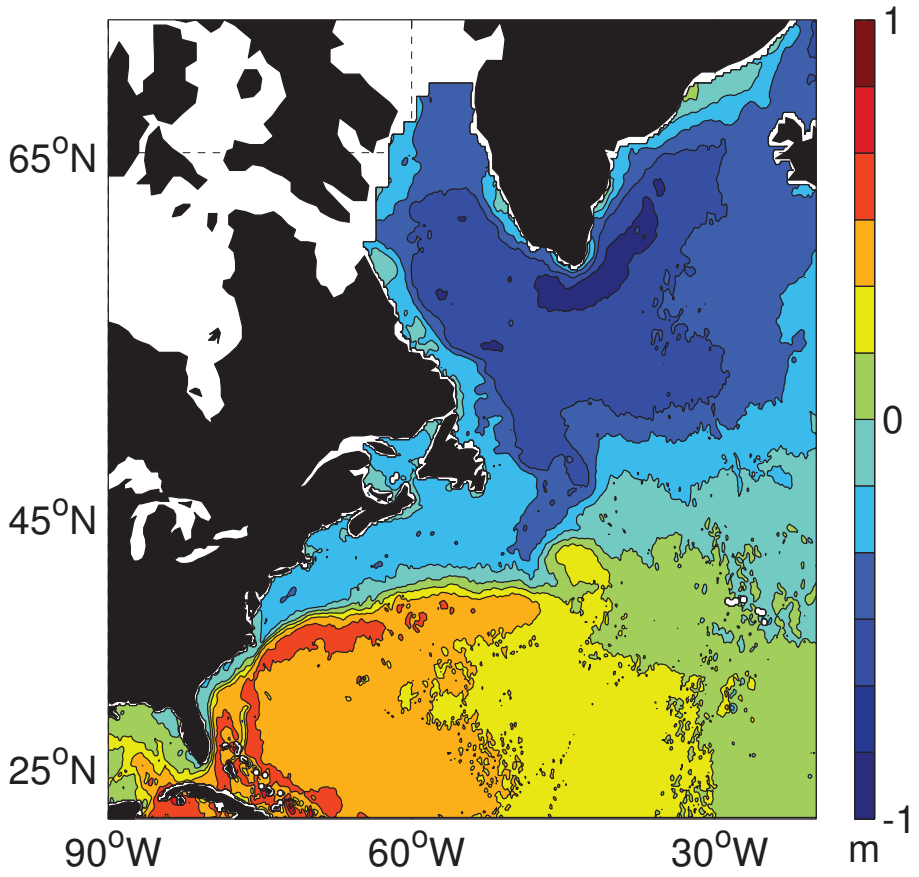

Figure 2.4: Mean dynamic topography, calculated as the difference between the MSS_CNES_CLS10 mean sea surface and the PCG08I geoid model.

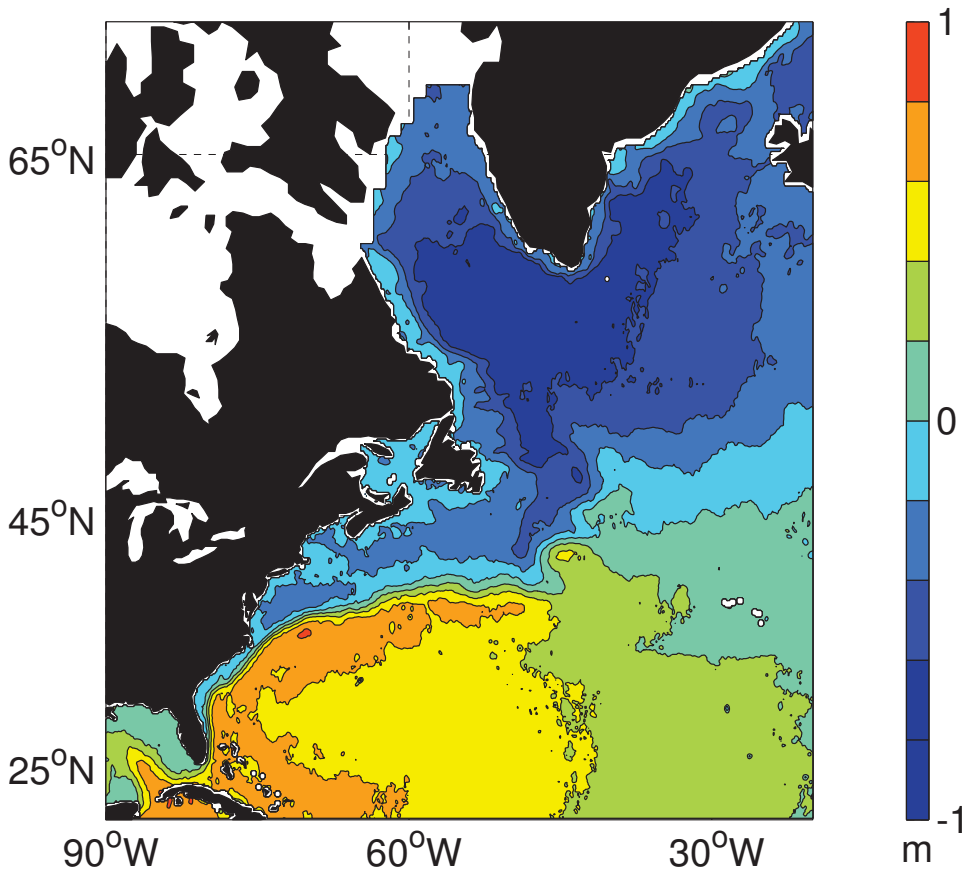

Figure 2.5: Mean dynamic topography, calculated as the difference between the MSS_CNES_CLS10 mean sea surface and the CGG2010 geoid model.

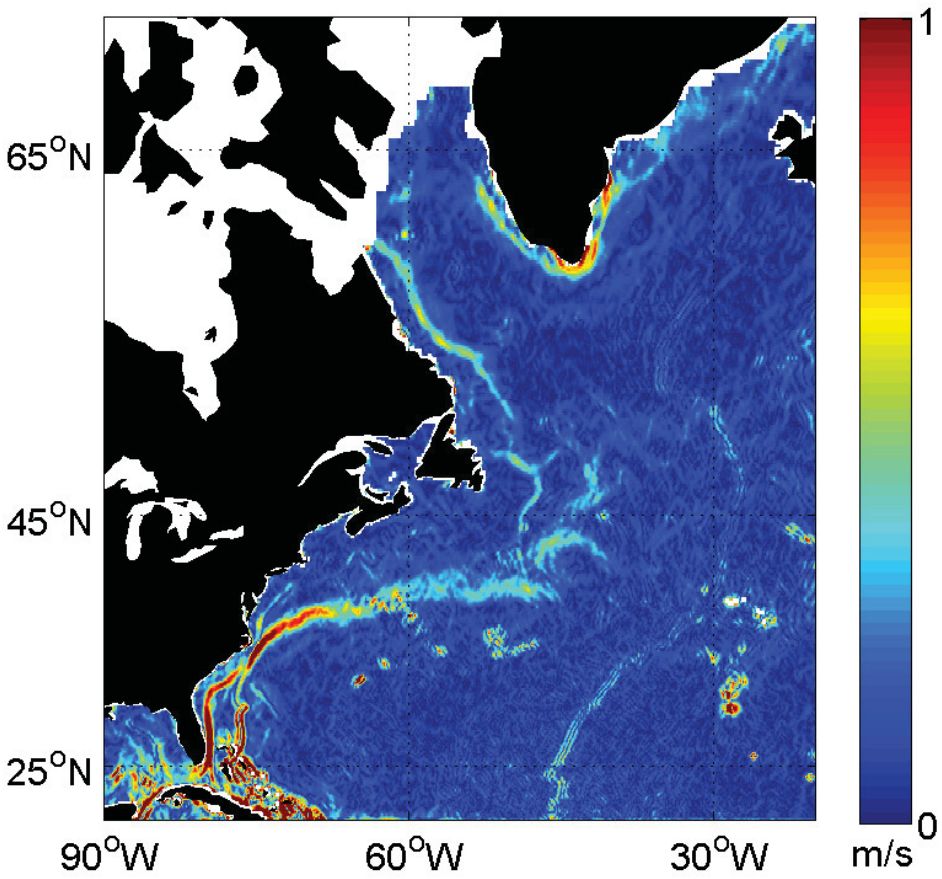

Figure 2.6: Total mean surface geostrophic current speed derived from the MDT shown in Figure 2.4, calculated using the PCG08I geoid model.

total geostrophic surface speeds are shown in Figure 2.6 for the PCG08I geoid, and in Figure 2.7 for the CGG2010 geoid.

The mean surface circulation is broadly similar in both plots, with the Gulf Stream system clearly visible, together with the shelfbreak currents around Greenland and along the coast of Labrador. The PCG08I estimate (Figure 2.6) includes spurious features around the Bahamas and in the open ocean south of the Gulf Stream. These spurious features are reduced in the CGG2010 estimate (Figure 2.7), and the Loop Current in the Gulf of Mexico is better defined.

These estimates of MDT and the mean surface geostrophic circulation will be examined more fully, and evaluated against oceanographic estimates, in later chapters of this thesis.

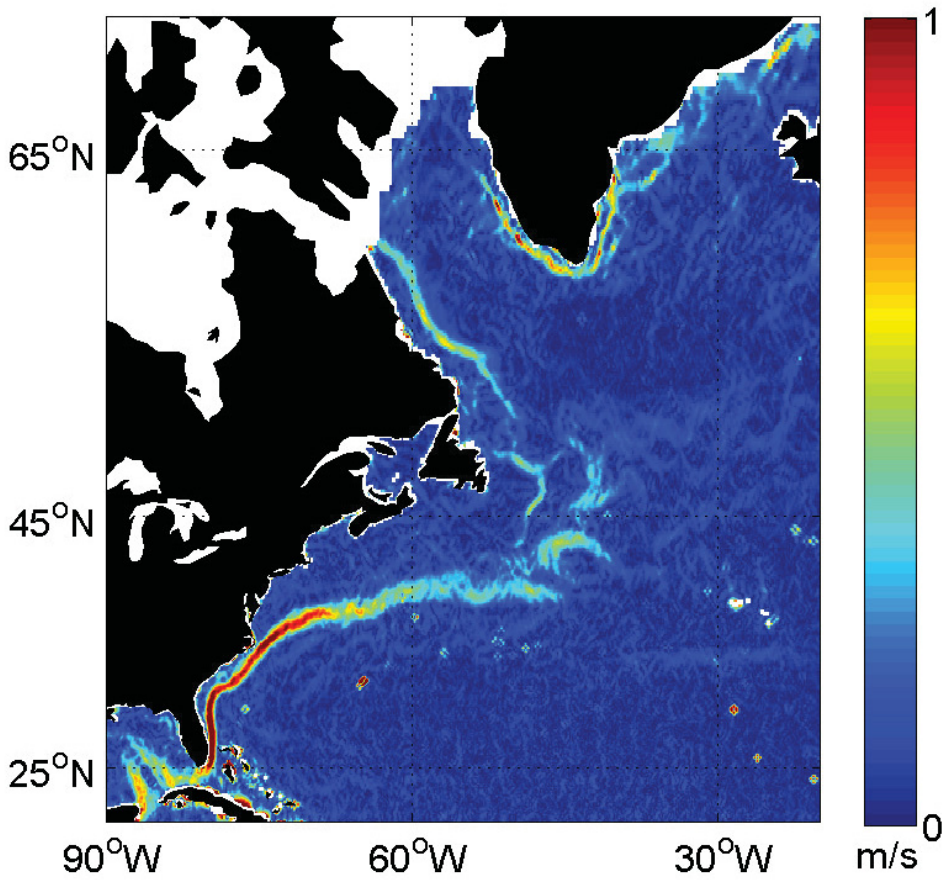

Figure 2.7: Total mean surface geostrophic current speed derived from the MDT shown in Figure 2.5, calculated using the CGG2010 geoid model.

CHAPTER 3

A NEW DECADAL TEMPERATURE-SALINITY CLIMATOLOGY

An oceanographic estimate of MDT can be constructed using a knowledge of the mean temperature and salinity (TS) structure of the ocean. This is typically provided in the form of a TS climatology. However existing TS climatologies are based on observations collected over many decades, and as such they may misrepresent the low-frequency (decadal and longer) variability that is dominant in the ocean (*Wunsch* [1981]). Whilst it is feasible to construct a climatology using shorter datasets, which would more accurately represent the mean state of the ocean for a given observational period, mesoscale (eddy) variability becomes more conspicuous and may be aliased into lower-frequency variability.

In this chapter a new method is described whereby eddy variability is removed from measured TS profiles using satellite altimeter data. The method is demonstrated using observations from the Argo network of drifting profilers, and a TS climatology is constructed which relates specifically to the period from 2000 to 2007.

3.1 Introduction

Temperature and salinity (TS) climatologies define the mean state of the ocean. TS climatologies are used, for example, to quality control ocean observations and to initialize and sometimes constrain ocean models. For this thesis TS climatologies are used to construct

oceanographic estimates of the MDT (see Chapter 4), which will then be compared with the geodetic estimates described in Chapter 2.

Vertical TS profiles have been measured for more than a century and, although non-uniform in their spatial and temporal coverage, they have been analyzed extensively to produce TS climatologies. This requires averaging and spatial smoothing of the sparse source data. Examples include the global $\frac{1}{4}^{\circ}$ World Ocean Atlas 2001 climatology (WOA01, *Boyer et al.* [2005]) and the North Atlantic climatology of Lozier (*Lozier et al.* [1995]). However major ocean features can vary on timescales of years to decades (and longer) so, when constructing an oceanographic MDT with the intention of estimating the mean ocean circulation, it is more appropriate to define the mean for shorter, specific periods. This has not been feasible in the past because of data sparseness.

The availability of TS data has increased significantly in recent years as a result of the Argo program. This network of drifting autonomous profilers presently measures 100,000 TS profiles each year compared with, for example, 20,000-30,000 profiles annually from all sources during the 1950s (*Boyer et al.* [2006]). The increase in observation density offers the possibility of defining a mean using observations from a time period of a decade or less. Problems with low frequency variability will be much less than in the multi-decadal dataset but aliasing of mesoscale variability remains an issue. This variability is reduced in conventional analyses by averaging but, for a shorter observation period and correspondingly smaller observation dataset, such averaging is less effective.

One way to deal with mesoscale variability is to average along potential density surfaces (*Lozier et al.* [1995]) and another is to assimilate data into an ocean model. Here a new technique for removing the mesoscale variability from TS profiles is described. This reduces the noise whilst retaining valuable information. The standard error of the sample mean is given by $\sigma/\sqrt{n}$, where σ is the population standard deviation of a random sample of n independent observations, and so reducing the standard deviation of the observations by half is equivalent to increasing the sample size by a factor of four.

The new scheme uses satellite altimeter measurements of sea surface height anomalies (η_a) to estimate isopycnal displacements and reduce the associated TS variability. It is

based on the assimilation technique developed by *Cooper and Haines* [1996], requires no prior knowledge of the TS fields and averaging is across depth surfaces, as for the widely-used WOA01 climatology. Isopycnal displacements which would produce a steric height anomaly equal to η_a are calculated. The TS profile is lifted or depressed by an equal amount in the opposite direction. The method assumes vertical advection is the dominant process influencing the water properties locally, although this is not the case near the surface or in shallow water. This restricts application of the technique to below the mixed layer of the deep ocean. The method also will not work where the barotropic effect is dominant (e.g. high latitude regions, including those where TS changes are density compensating) but these are areas where there is less variability and there are fewer problems with existing climatologies.

There are similarities between this new approach and the methods developed by *Guinehut et al.* [2004], *Ridgway and Dunn* [2010] and *Willis et al.* [2003]. These authors also used remote sensing data to reduce the error in observations of the subsurface temperature field, but they used linear regression techniques or empirical models whereas the scheme described here is based on dynamical balances.

3.2 Data

To illustrate the method the most eddy-rich region of the northwest Atlantic, 80°W-20°W 20°N-50°N, is considered (Figure 3.1).

3.2.1 Argo

The global Argo network comprises an array of approximately 3000 drifting profilers. The first floats were launched in 2000 with full deployment by 2007. Each float measures a vertical TS profile of the upper ocean, to a maximum depth of 2000 m, every ten days (*Roemmich et al.* [2000]). At the end of each ten day cycle the float comes to the surface and transmits data to regional Data Assembly Centres via the Global Telecommunications System. Two Global Data Assembly Centres maintain a data archive and distribute data to users in both near-real time and quality controlled delayed time modes.

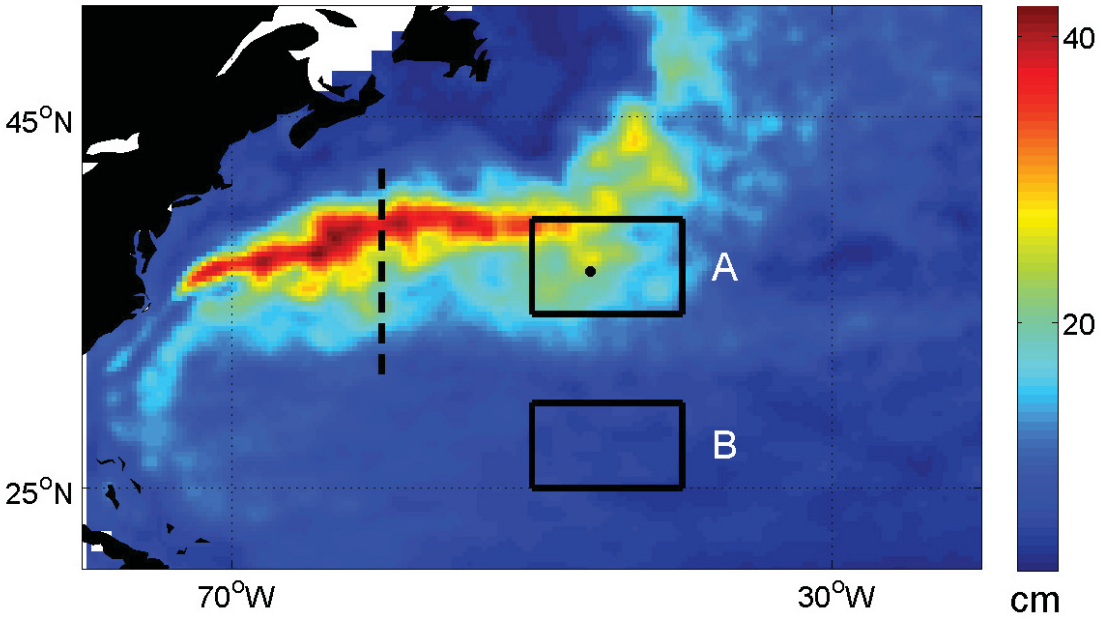

Figure 3.1: Standard deviation (cm) of sea surface height variability for the period 2000 to 2007 calculated using daily AVISO $\frac{1}{4}^{\circ}$ gridded altimeter sea surface height anomalies. The solid boxes show the subdomains used in Figure 3.3, the filled circle inside box A indicates the location of data plotted in Figure 3.2, and the dashed line identifies the section plotted in Figure 3.7.

For this study all quality controlled profiles from the northwest Atlantic between 1 January 2000 and 31 December 2007 are examined, a total of more than 31,000 profiles. Floats affected by a pressure offset error identified by the Argo project team (details available at http://www.argo.ucsd.edu/Acpres_bias.html) are excluded from the study. A total of nearly 10,000 profiles had complete temperature and salinity measurements between the surface and 1500 m, and a further 12,000 profiles had partial TS measurements. There were approximately 2,000 profiles measured during 2000 in the northwest Atlantic domain used for this study, increasing steadily to around 6,000 profiles during 2007. TS values are interpolated to standard depths corresponding with the WOA01 climatology depths.

3.2.2 Altimeter

A continuous record of sea surface height variability is available from October 1992 to date based on altimeter measurements made by the Topex/Poseidon, ERS-1/2, Envisat, Jason-1 and Jason-2 satellites. The "Reference Series Delayed-Time" daily maps of sea surface height anomaly are used. These are distributed by AVISO, with a grid spacing of $\frac{1}{4}^\circ$ (*Ducet et al.* [2000]). Instrument, atmospheric and geophysical corrections have been applied. This study focuses on the period 2000–2007, the period of the Argo data described above, and the mean for this period has been removed.

The standard deviation of η_a is largest along the path of the Gulf Stream (Figure 3.1). This is an indicator of eddy activity and corresponds closely with the pattern of eddy kinetic energy estimated from drifter tracks (*Fratantoni* [2001]). Maps of the variance of temperature and salinity measured by Argo floats (not shown) exhibit a similar pattern.

3.3 A Simple "De-eddying" Technique

Measurements below the mixed layer in mesoscale eddies show vertical isopycnal displacements of up to several hundred metres (e.g. *Richardson et al.* [1978]). The displacement is upwards (downwards) in cold-core (warm-core) eddies, producing horizontal temperature differences of up to 5°C relative to water outside the eddy. Repeat sampling at a given

depth and location will, in the presence of eddies, likely include TS measurements corresponding to water normally found higher and/or lower in the water column. Observations are consistent with this, showing local TS properties that are not identical but aligned with the local climatological TS relationship (Figure 3.2, left panel).

Isopycnal displacements are likely the cause of TS variability seen below the mixed layer (Figure 3.3, solid lines). Much higher variability can be seen below the mixed layer in domain A (a region of high η_a variability) than in domain B (low η_a variability). Other processes, such as heating and mixing, likely contribute to the near-surface variability. The isopycnal displacements produce changes in steric height and η_a is a reasonable approximation of steric height (calculated between 1500 m and 120 m to exclude the effect of other processes in the mixed layer) with a high correlation between the two (Figure 3.4, left panel, r=0.67 for the northwest Atlantic domain). Here η_a from the AVISO fields is used to estimate the isopycnal displacement and adjust the Argo profiles using a method based on the assimilation technique developed by *Cooper and Haines* [1996] (hereafter CH96).

CH96 developed a simple technique to assimilate surface pressure into an ocean model by vertically rearranging water parcels without modifying their TS properties. They assumed that the rearrangement is adiabatic and frictionless. They started with the hydrostatic connection between a surface pressure update (Δp_s, the difference between the observed value and the model a priori) and changes to the subsurface pressure field,

$$\Delta p(z) = \Delta p_s + g \int_z^0 \Delta\rho dz \tag{3.1}$$

where $\Delta\rho$ are updates to the subsurface density. They introduced a bottom constraint,

$$\Delta p(z = -H) = 0 \tag{3.2}$$

where H is the depth of the bottom of the water column. With this constraint, and rearranging,

$$\Delta p_s = g \int_{-H}^0 \Delta\rho dz \tag{3.3}$$

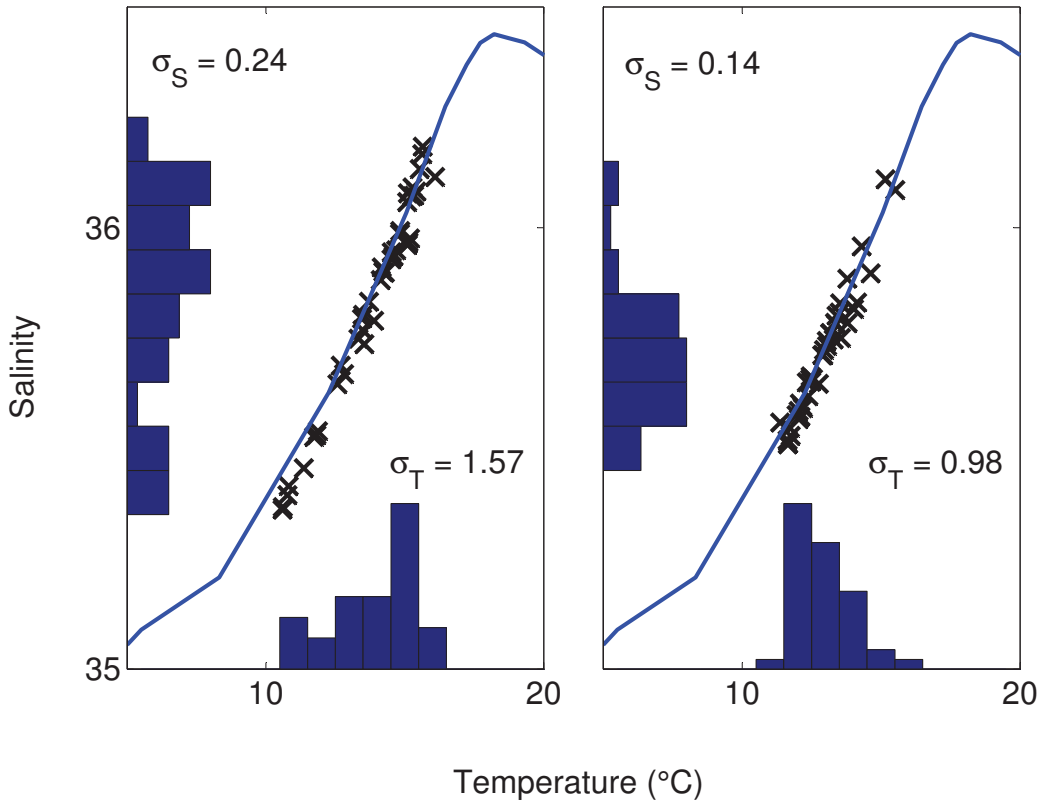

Figure 3.2: TS relation for observations, with and without de-eddying. Crosses show the TS relationship at a depth of 610 m for all Argo profiles recorded within 100 km of 37°N 46°W between 1 January 2000 and 31 December 2007 before (left) and after (right) the de-eddying adjustment. The line shows the annual mean climatological TS relation for all depths from the surface to 1500 m depth at this location from the WOA01 $\frac{1}{4}^\circ$ climatology. The distributions of temperature and salinity values are plotted as histograms against the x-axis and y-axis respectively along with the corresponding standard deviations (σ_T and σ_S).

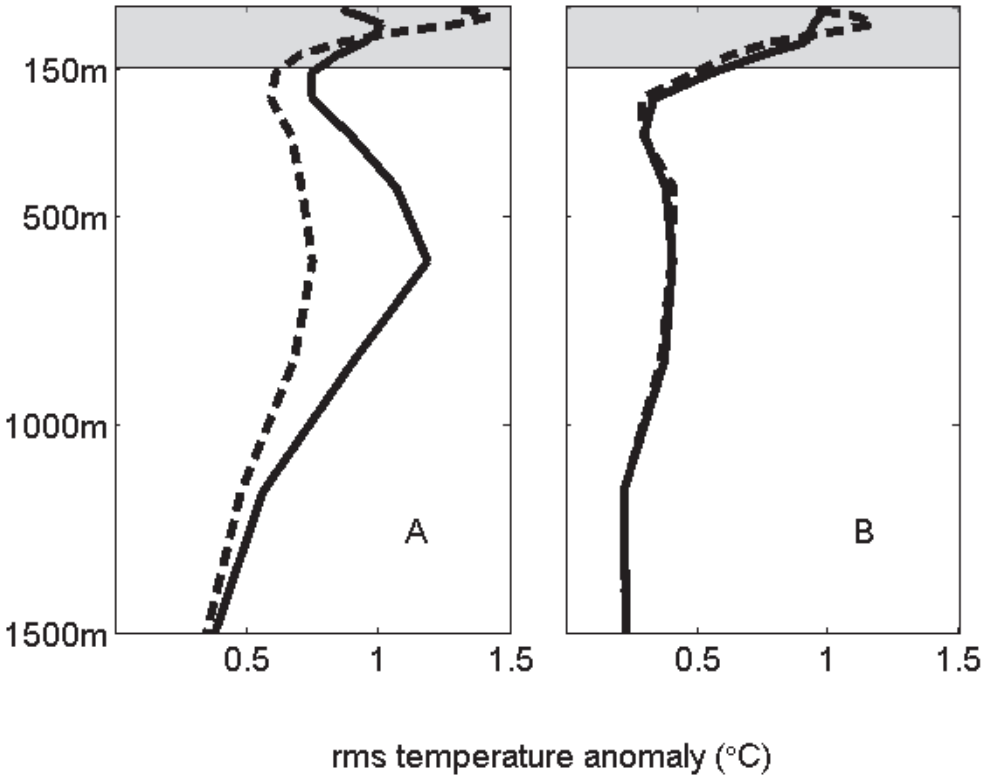

Figure 3.3: RMS temperature anomaly (°C) of Argo temperature relative to the WOA01 $\frac{1}{4}^{\circ}$ climatology (*Boyer et al.* [2005]), before (solid line) and after (dashed line) adjustment, plotted against depth for subdomains A (left) and B (right). These domains are shown on Figure 3.1. The shaded zone represents the surface mixed layer where processes other than vertical advection are believed to dominate.

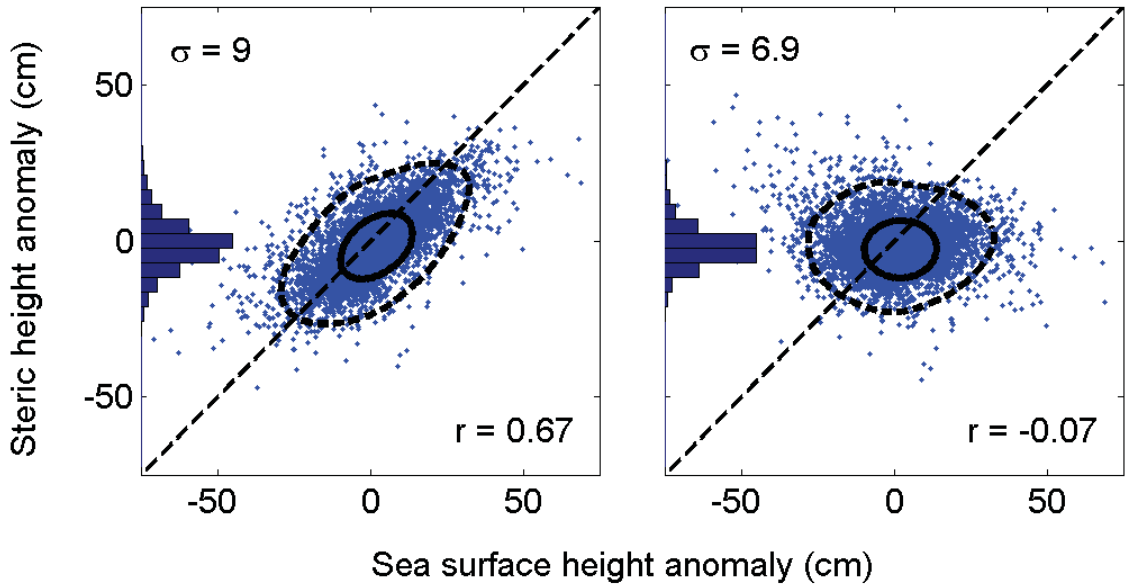

Figure 3.4: Steric height anomalies calculated between 1500 m and 120 m using Argo TS profiles, plotted against co-located altimeter sea surface height anomalies, from AVISO $\frac{1}{4}^{\circ}$ gridded fields, before (left) and after (right) the de-eddying adjustment is applied to the Argo profiles. The contours contain 50% (inner solid contour) and 95% (outer dashed contour) of the data points. The distributions of steric height values are plotted as histograms against the y-axes along with the corresponding standard deviations (σ). The correlation coefficient (r) is also shown.

which is a balance between the change in surface pressure and the change in weight of the water column. Assuming a vertical displacement of the water column that is constant with depth, and ignoring any changes due to horizontal advection, mixing and heat/salt inputs,

$$\Delta p_s = g[\rho(0) - \rho(-H)]\Delta h \tag{3.4}$$

where Δh is the vertical displacement.

Motivated by their technique, the vertical displacement (δh) is calculated as

$$\delta h = \gamma \frac{\rho_t}{\rho_t - \rho_b} \eta_a \tag{3.5}$$

where η_a is the altimeter sea level anomaly with the seasonal cycle removed and ρ_t and ρ_b are potential density at the top and bottom of the water column. This formula reduces to that used by CH96 when γ=1. The relationship between δh and η_a is illustrated in Figure 3.5. The water column is lifted by an amount δh, resulting in the loss of the top water parcel, with density $\rho 1$ and the addition of a new bottom water parcel, with density $\rho 4$. The change in steric height, η_a is given by the formula to the right, a rearrangement of (3.5) with γ=1. Assuming that the density of the bottom parcel is greater than the density of the top parcel (i.e. $\rho 4 > \rho 1$), the surface anomaly resulting from the upward displacement of the water column is negative.

For each measured Argo TS profile the displacement δh is calculated using (3.5) and the sea surface height anomaly η_a that is co-located in time and space. The Argo TS values at depth z are displaced to depth z+δh. Adjusted values at the standard WOA01 depths are then estimated using linear interpolation. There is some subjectivity in the choice of top and bottom levels for the calculation of the displacement, and for this study the water column between the surface and 1500 m is considered.

The adjustment factor γ is chosen to optimize the adjustment technique. The de-eddying adjustment is applied to all complete Argo TS profiles in the Gulf Stream domain using a range of values of γ. Steric height is calculated for each adjusted profile and the single value of γ that minimizes the monthly variance of steric height is chosen (Figure 3.6).

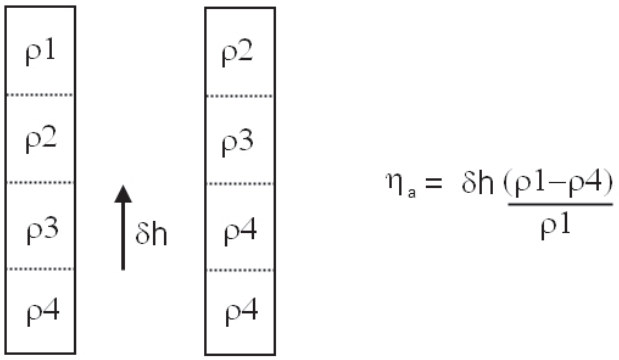

Figure 3.5: A highly idealized schematic illustrating the de-eddying technique. The boxes to the left represent a simplified water column with 4 density layers, $\rho 1$ to $\rho 4$. The thickness of each layer is δh. The boxes to the right represent the same water column after it is lifted by amount δh, equal to the thickness of one layer. The change in steric height, η_a is calculated as shown by the formula to the right, a rearrangement of (3.5). The reverse situation, associated with a downward displacement, would be represented by the loss of $\rho 4$ at depth and the gain of an additional layer of $\rho 1$ at the surface.

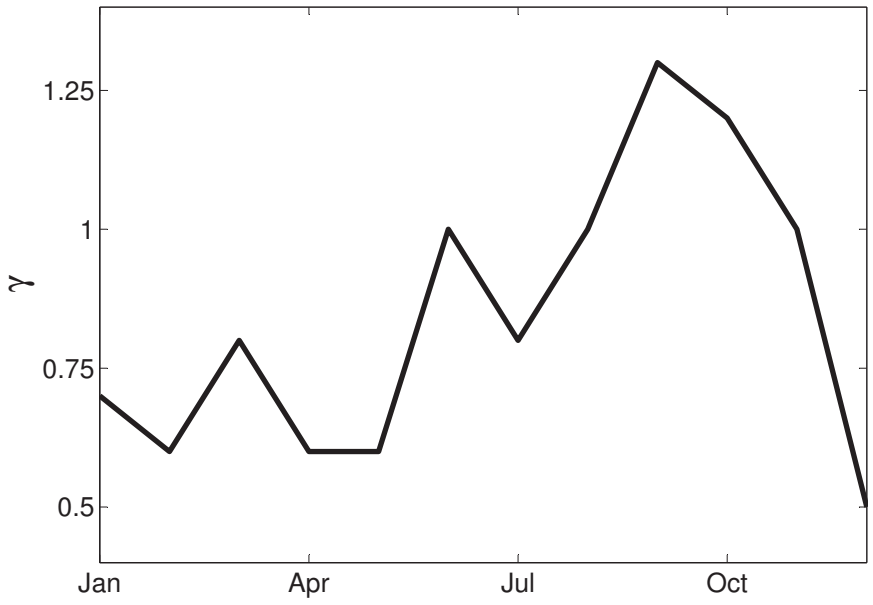

Figure 3.6: The monthly values of the adjustment factor, γ, chosen as the value which minimizes the variance of steric height when applied to Argo profiles across the Northwest Atlantic domain.

Here γ adjusts for the processes which are not represented in this simple correction, such as surface heating and changes below the 1500 m reference level.

With the optimized set of values of γ the adjustment is applied to the entire Argo dataset, including incomplete profiles. In order to allow the de-eddying of these incomplete profiles, ρ_t and ρ_b are calculated from the WOA01 $\frac{1}{4}^\circ$ monthly climatology (*Boyer et al.* [2005]) and the resulting displacement applied to the partial profiles. This does not seem to significantly alter the typical magnitudes of the adjustment compared to using the measured values of ρ_t and ρ_b.

3.4 Results from the Northwest Atlantic

Applying the de-eddying adjustment to the Argo profiles from the northwest Atlantic domain, values of γ between 0.5 (December) and 1.3 (September) are found to minimize the variance (Figure 3.6). Using these values the strong correlation (r=0.67) between steric height and the corresponding η_a is almost totally removed by applying the adjustment (r=-0.07 afterwards, Figure 3.4, right panel). Without the optimization the method seems to slightly over-correct the measurements (r=-0.27 with γ=1).

Subdomains A and B (Figure 3.1) are representative regions of high and low hydrographic and sea level variability. The RMS temperature anomaly relative to the WOA01 $\frac{1}{4}^\circ$ climatology is calculated for all profiles within each subdomain before and after the method is applied (Figure 3.3). The de-eddying technique has little effect on profiles in the region of low variability, as expected. In the high variability region the maximum effect is achieved at a depth of 600 m, with the RMS temperature anomaly reduced from near 1.2°C to 0.75°C. There is an increase in the RMS temperature anomaly in the surface mixed layer for both regions, almost certainly because processes other than vertical advection become important near the surface.

The scatter in the TS relation for profiles close to 37°N 46°W (the filled circle in Figure 3.1) illustrates the vertical displacements associated with eddies (Figure 3.2, left panel). This scatter is reduced when the method is applied (Figure 3.2, right panel), with the standard deviation of both temperature and salinity reduced by about 40%. This is a

region of high sea surface height variability where the technique is expected to have most effect.

To further illustrate the method the Argo profiles are used to create monthly climatological TS maps, both before and after the de-eddying adjustment is applied. The climatologies are constructed using optimal interpolation, with WOA01 (*Boyer et al.* [2005]) providing the background field. A description of the optimal interpolation technique is included in Appendix B. The resolution is $\frac{1}{4}^\circ$, and the vertical levels are the same as for WOA01.

As an example of the new climatology, Figure 3.7 shows the climatological temperature field for April along a meridional section at 60°W, for WOA01 (top panel) and for the Argo period climatologies, before (middle panel) and after (bottom panel) the adjustment is applied. Note that the method reduces an eddy-like feature around 34°N. The isotherms in the vicinity of the Gulf Stream (around 40°N) slope more steeply in the Argo climatologies than in WOA01.

To further illustrate the new climatology, Figure 3.8 shows the steric height (see Equation 1.5) calculated from the annual fields for WOA01 and the new climatology constructed using de-eddied Argo profiles, together with their differences. Steric height is useful for comparing climatologies because it integrates density differences through the depth of the water column. Whilst broadly similar, there are differences between the two climatologies, especially in the vicinity of the Gulf Stream. The gradient across the Gulf Stream is steeper for the new climatology and the height difference across the Gulf Stream is greater for the new climatology. This will be considered in more detail in Chapter 6.

3.5 Discussion

Existing TS climatologies are derived from observations collected over many decades and, as the dominant variability in the ocean is low frequency, this can lead to a misleading representation of the mean state of the ocean. For example low frequency shifts in the position of the Gulf Stream may result in a cross-current density gradient that is overly smoothed.

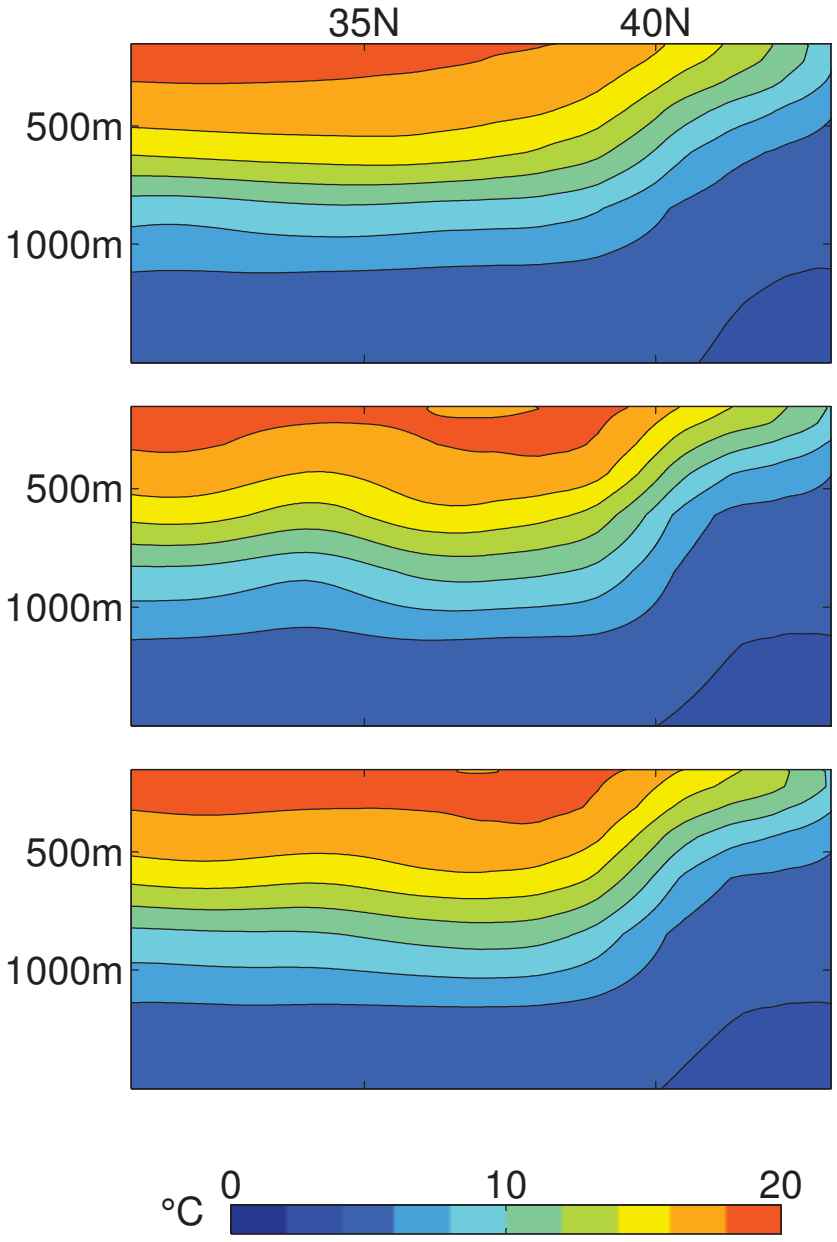

Figure 3.7: Temperature section across the Gulf Stream. Top panel: The climatological temperature field for April, from the WOA01 $\frac{1}{4}^{\circ}$ climatology, plotted from 150 m to 1500 m depth along a meridional section at 60°W from 31°N to 43°N (as shown on Figure 3.1). Middle and Bottom panels: The corresponding temperature fields derived from all Argo profiles recorded during April from 2000 to 2007 inclusive, before and after applying the de-eddying adjustment, with the same spatial smoothing applied to each.

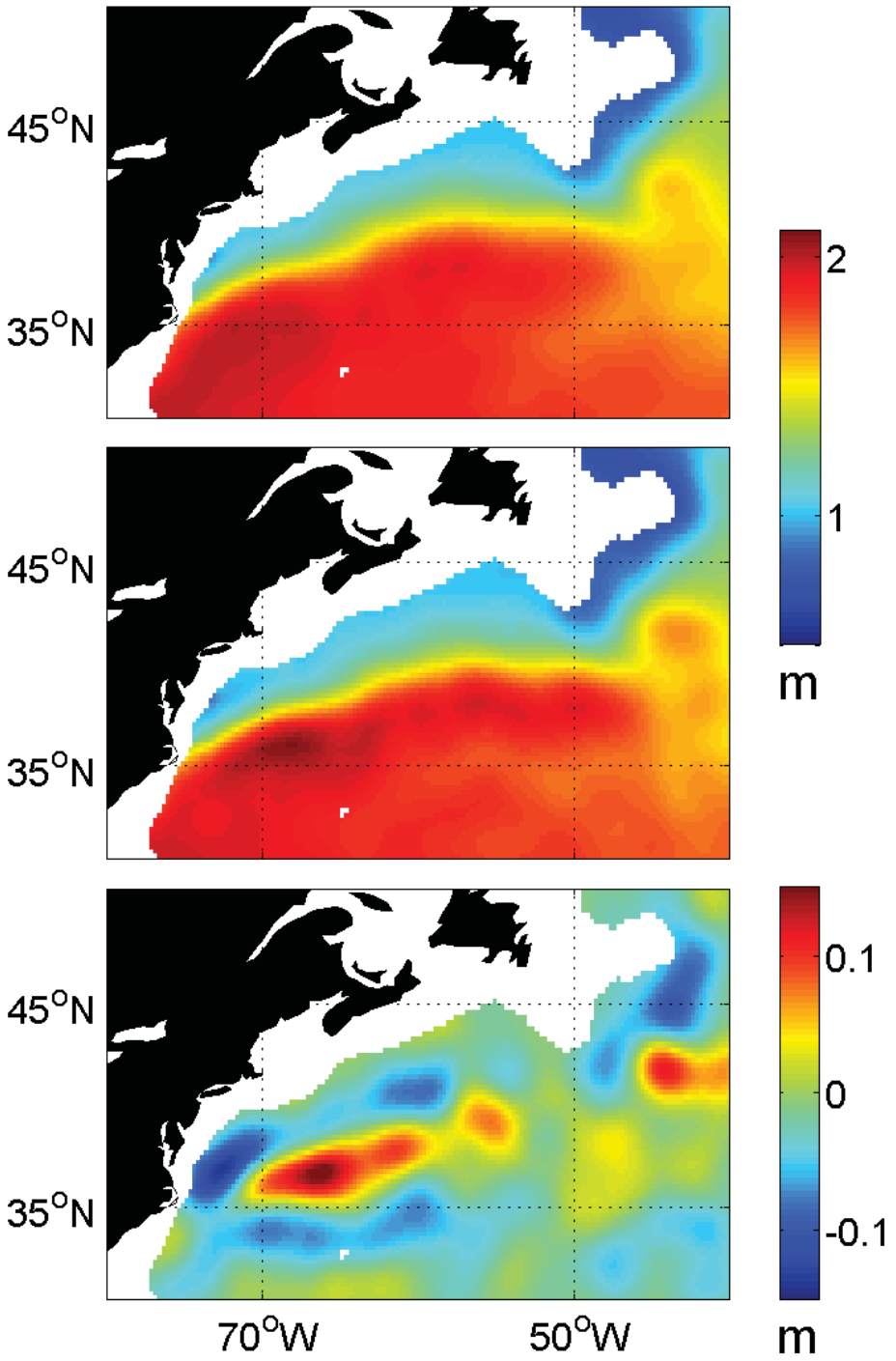

Figure 3.8: Steric heights from TS climatologies in the Gulf Stream region. Top panel: Steric height between 1500 m and the surface calculated from the WOA01 $\frac{1}{4}^{\circ}$ annual TS climatology. Middle panel: The corresponding steric height from a new annual climatology based on de-eddied Argo profiles from 2000 to 2007 inclusive. Bottom panel: The difference between the two steric height fields (Argo climatology minus WOA01).

In this chapter it is shown that it is possible to define a climatology using data collected over only 8 years using a simple technique, based on the idea of CH96, to reduce the mesoscale noise in the observations. Generally there is good agreement between the new climatology and WOA01, although there are interesting differences which will be investigated in later chapters.

The technique is simple, transparent and reproducible, requiring only η_a and the seasonally-varying γ. There are areas where it will not work well, for example the surface mixed layer. This is not surprising because the method assumes that vertical advection is the only process affecting local TS properties, which is clearly not the case near the surface. The value of the technique is in improving existing climatologies in dynamic regions such as the western boundary currents where low frequency and mesoscale variability make it difficult to define a meaningful climatology. This study uses TS profiles from the Argo network but other in situ observations recorded since the satellite altimeter record began in 1992 can be similarly adjusted (including other variables with a strong vertical gradient, e.g. nutrients).

In the following chapter this technique will be used to produce new oceanographic estimates of the MDT for the North Atlantic, which will then be compared with the new geodetic estimates described in Chapter 2.

CHAPTER 4

OCEANOGRAPHIC ESTIMATES OF MEAN DYNAMIC TOPOGRAPHY

Some of the earliest maps of the surface circulation of the North Atlantic were produced using oceanographic estimates of the MDT (e.g. *Sverdrup et al.* [1942]). These maps were produced using dynamic height calculated from sparse TS measurements. Over subsequent years the number of TS observations has increased and, because of the relative simplicity of the computations, dynamic or steric height has remained in widespread use for estimating the circulation. For example, *Reid* [1994] mapped the subsurface geostrophic circulation of the North Atlantic using dynamic height calculated from TS profiles.

Whilst the dynamic (or steric) height approach is simple, it requires an assumption that there is a deep level of no motion which can be used as the reference level from which to calculate the heights. An alternative approach is to incorporate TS observations into an ocean circulation model. This requires no assumption of a level of no motion, and the same circulation model can be used to diagnose ocean processes influencing MDT.

Both approaches require TS observations which, for the purposes of defining the MDT, can be provided in the form of a TS climatology. Traditional climatologies, such as WOA01, are based on measurements from many decades. These measurements are temporally and spatially inhomogeneous and as a result the climatology may misrepresent both low frequency and high frequency variability in the mean.

In the previous chapter the construction of a new climatology was described. This is based on only 8 years of data, with mesoscale variability removed using a new de-eddying technique. The combination of a short averaging period and the de-eddying simultaneously reduces the high and low frequency variability in the observations, and there is less misrepresentation of such variability in the climatology.

In this chapter oceanographic estimates of the MDT will be produced by applying both a steric height approach and an ocean model approach to TS climatologies. The WOA01 climatology and the new Argo-period climatology will be used and the resulting MDTs compared.

4.1 MDT from the Mean Density Field

In Chapter 1 the calculation of dynamic and steric height from TS measurements was described. Here this approach is used to estimate the MDT using the mean annual TS climatological values. Typically TS climatologies are defined on depth levels rather than pressure levels, so it is more appropriate to use the steric height calculation (1.5).

The annual $\frac{1}{4}^\circ$ TS climatologies of WOA01 (*Boyer et al.* [2005]) and the new Argo-period climatology described in the previous chapter are used. WOA01 is constructed from observations collected over many decades, whereas the Argo-period climatology uses data from the period 2000–2007 only. In both cases the annual climatologies are defined on a $\frac{1}{4}^\circ$ grid at 33 depth levels from 0 m to 5500 m. Both climatologies are produced as monthly fields, but here the mean annual values are used.

To produce a MDT across an ocean basin all points must be integrated over the same depth interval. The choice of the depth interval is a compromise. A deep reference level will limit the extent of MDT, since steric height is not calculated in areas shallower than the reference level. A shallow reference level will exclude part of the baroclinic signal and there will be horizontal pressure gradients at the reference level – contrary to the assumption of this being a level of no motion. Here steric height is calculated between 1500 m and the surface, corresponding with the interval used for the de-eddying technique described in Chapter 3.

4.2 Steric Height Results for the North Atlantic

The top panel of Figure 4.1 shows steric height calculated from the WOA01 annual TS climatology, and the middle panel shows steric height calculated using the Argo period climatology. In each case the height has been normalized by subtracting the mean steric height of all points within the plotted domain. This normalization is necessary to allow comparison with other MDT estimates.

Whilst the two plots appear similar, the differences (Figure 4.1, bottom panel) are between 10 cm and 20 cm around the Gulf Stream between Cape Hatteras and the Grand Banks. The differences around the Gulf Stream are illustrated by Figure 4.2 (top panel), which shows both estimates of the MDT along a meridional section at 70°W. The gradient across the Gulf Stream is noticeably steeper in the Argo climatology estimate, which will translate into a faster Gulf Stream when the mean surface geostrophic speed is calculated from the gradients of the MDT.

Also noticeable is an increase in steric height in the new climatology in the subpolar gyre. This is consistent with the findings of *Hakkinen and Rhines* [2004] and *Hakkinen and Rhines* [2009] that sea surface height increased in the subpolar gyre during the 1990's and 2000's, leading to a decline in the circulation of the subpolar gyre.

4.3 MDT Estimated Using an Ocean Model

The steric height approach is limited to deep waters, and relies on the assumption that there is a deep level with no horizontal pressure gradients. An alternative approach, which does not suffer from these limitations, is to run an ocean circulation model incorporating the TS climatology by way of a spectral nudging scheme.

Figure 4.1 *(following page)*: Steric height calculated from two climatologies. (Top panel) Steric height calculated between 1500 m and the surface using the WOA01 $\frac{1}{4}^\circ$ annual TS climatology. (Middle panel) The same but calculated with the new Argo-period climatology. (Bottom panel) The difference, shown as the Argo-period climatology height minus the WOA01 height. These figures are similar to Figure 3.8 but for a larger domain.

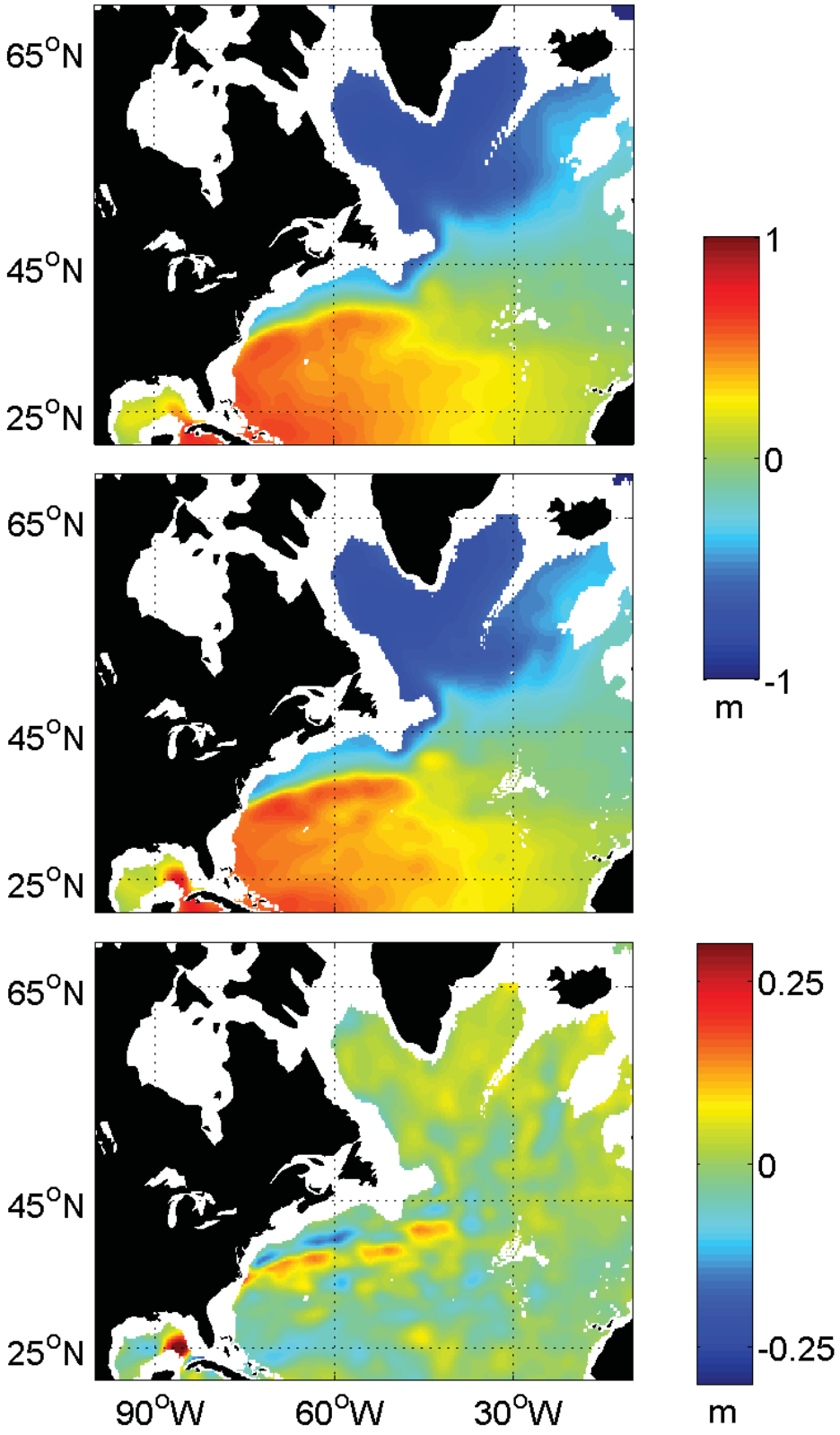
65°N
45°N
25°N
65°N
45°N
25°N
65°N
45°N
25°N
90°W
60°W
30°W
1
0
-1
m
0.25
0
-0.25
m

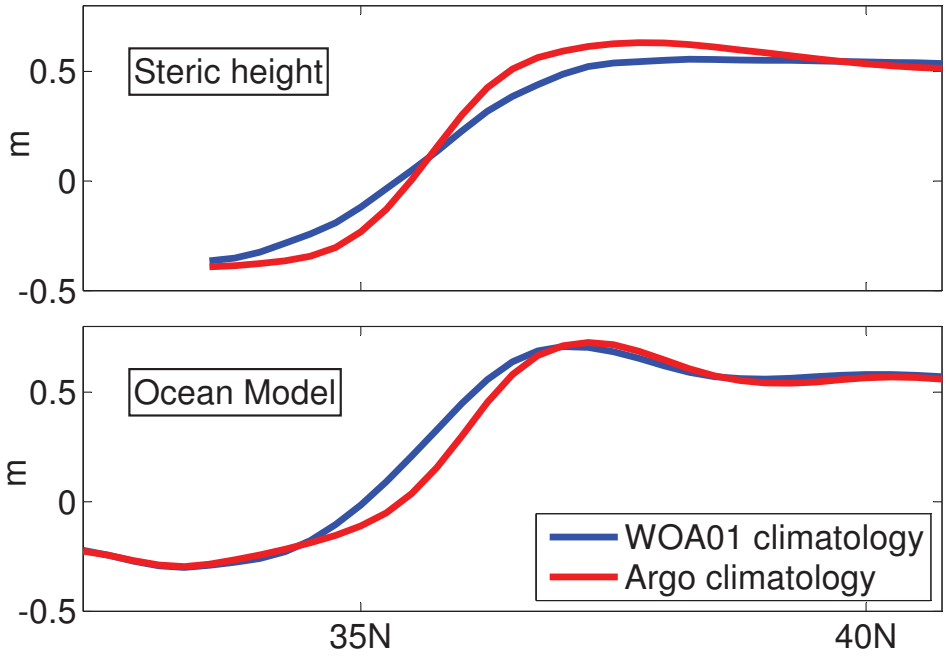

Figure 4.2: Comparison of MDT estimates along a section at 70°W. (Top panel) Mean dynamic topography along a meridional section across the Gulf Stream at 70°W, calculated using the steric height approach with the WOA01 TS climatology (blue line) and the new Argo period TS climatology (red line). (Bottom panel) The same plot calculated using the ocean model approach.

4.3.1 The Nemo Ocean Model

The ocean model is based on version 2.3 of NEMO (Nucleus for European Modelling of the Ocean). NEMO is a complete modelling framework, including modules for the dynamics of the ocean (OPA, *Madec et al.* [1998]) and the dynamics of sea-ice (LIM, *Fichefet and Maqueda* [1997]).

OPA is a three-dimensional numerical ocean circulation model. It is configured here to use z-level coordinates and the model permits partial cells, whereby the bottom level thickness can be adjusted, to accommodate the depth from an input bathymetry. The modelled equations include the horizontal momentum equations, the hydrostatic equation, the continuity equation, tracer equations for temperature and salinity, and the thermodynamic equation of state. Small scale physical processes such as horizontal and vertical mixing are parameterized.

The model grid is a North Atlantic subset (5-68°N, 100°W-34°E) of a global tri-polar grid with nominal $\frac{1}{4}^\circ$ resolution. Typical grid spacing is about 24 km in the subtropical gyre around 30°N, reducing to about 14 km in the subpolar gyre around 55°N. There are a maximum of 46 z-levels in the vertical, with level thickness increasing from approximately 6 m at the surface to 250 m at the bottom.

The model is forced by 10 m wind, air temperature and specific humidity, and surface radiation and precipitation. Values are from the Common Ocean-Ice Reference Experiments (CORE) normal-year data set (*Large and Yeager* [2009]), interpolated to the model time step and grid. Surface fluxes are calculated by the model using bulk formulae.

As this is a regional model, boundary conditions must be prescribed. Here ocean temperature, salinity and transport at the open boundaries are provided from a global $\frac{1}{4}^\circ$ NEMO model.

4.3.2 Spectral Nudging

The ocean model incorporates spectral nudging (*Thompson et al.* [2006]), which is designed to suppress model bias and drift. The model is nudged toward an observed TS climatology in selected wavenumber and frequency bands (in this case the frequencies of 0 and 1 cycles per year that are resolved by the TS climatology). Outside of these frequency bands the model is not nudged and it can evolve prognostically.

The effect of this scheme is that, at longer timescales, the model state is brought back toward the TS climatology. Hence the temporal mean will be largely based on the climatology, much like the robust diagnostic approach of *Sarmiento and Bryan* [1982]. However the model is allowed to evolve prognostically at shorter timescales so higher frequency features such as eddies are not suppressed. This allows nonlinear dynamics to contribute to the mean ocean state.

4.4 Ocean Model Results for the North Atlantic

The model is run, with spectral nudging, for the period from 1993 to 2000. At the end of this spin up period the model is in a statistical steady state. The model is then run for the period from 2001 to 2004 with spectral nudging to one of the two climatologies, either WOA01 or the new Argo-period climatology. The nudging is applied to the continental shelves as well as the deep ocean, although the new climatology defaults to the WOA01 values in shallow water where Argo does not operate. Instantaneous values of sea surface height are output for each gridpoint every 5 days, and the MDT is calculated as the time-mean sea surface height over the four year run.

Figure 4.3 shows the ocean model estimate of MDT using the WOA01 climatology (top panel) and using the new Argo-period climatology (middle panel). Both plots have been normalized by subtracting the mean of all gridpoints for which a value exists on the steric height plots (Figure 4.1).

The difference of the two estimates (Figure 4.3, bottom panel) shows an increase in height in the subpolar gyre, as for the steric height calculation of the MDT (Figure 4.1,

bottom panel). There are differences along the path of the Gulf Stream, from Cape Hatteras to beyond the Grand Banks, which require further investigation. These differences are smaller than when calculated using the steric height approach, which may be because there are compensating changes below the reference level (1500 m) which are not reflected in the steric height estimate. The section at 70°W (Figure 4.2, bottom panel) shows that the gradient across the Gulf Stream is steeper for the Argo period climatology MDT than it is for the WOA01 climatology, but the difference is not as great as when calculated using the steric height approach (top panel).

4.5 Comparison of the Two Approaches to Calculating MDT

Estimates of MDT based on both steric height calculations and using an ocean model have been presented. The estimates from the ocean model extend into shallow waters near the coast whereas the steric height estimates are restricted to waters deeper than the 1500 m reference level. Other differences are highlighted by plots of the differences between the two approaches for both the WOA01 climatology (Figure 4.4, top panel), and the new Argo-period climatology (Figure 4.4, bottom panel).

In both plots the dominant difference is along the path of the Gulf Stream, from Cape Hatteras eastwards. The model-derived MDT is some 20 cm higher along much of the current. This may be related to eddy activity, permitted in the spectrally-nudged model and perhaps contributing to the MDT through non-linear effects. Other differences include areas of lower model-derived MDT on the southern edge of the Gulf Stream and in the interior of the subpolar gyre. This may be caused by a baroclinic signal below 1500 m which is being missed by the steric height estimate. For example, *Meinen et al.* [2009] identified a Gulf Stream signal in hydrography below 1500 m, and *Yashayaev* [2007] observed temporal variability in the deep Labrador Sea associated with deep winter convection.

Figure 4.3 *(following page)*: MDT calculated using an ocean model and a climatology. (Top panel) MDT calculated as the four year mean sea surface height from an ocean model that is spectrally nudged toward the WOA01 $\frac{1}{4}^{\circ}$ annual TS climatology. (Middle panel) The same but calculated using the new Argo-period climatology. (Bottom panel) The difference, shown as the Argo-period climatology MDT minus the WOA01 MDT.

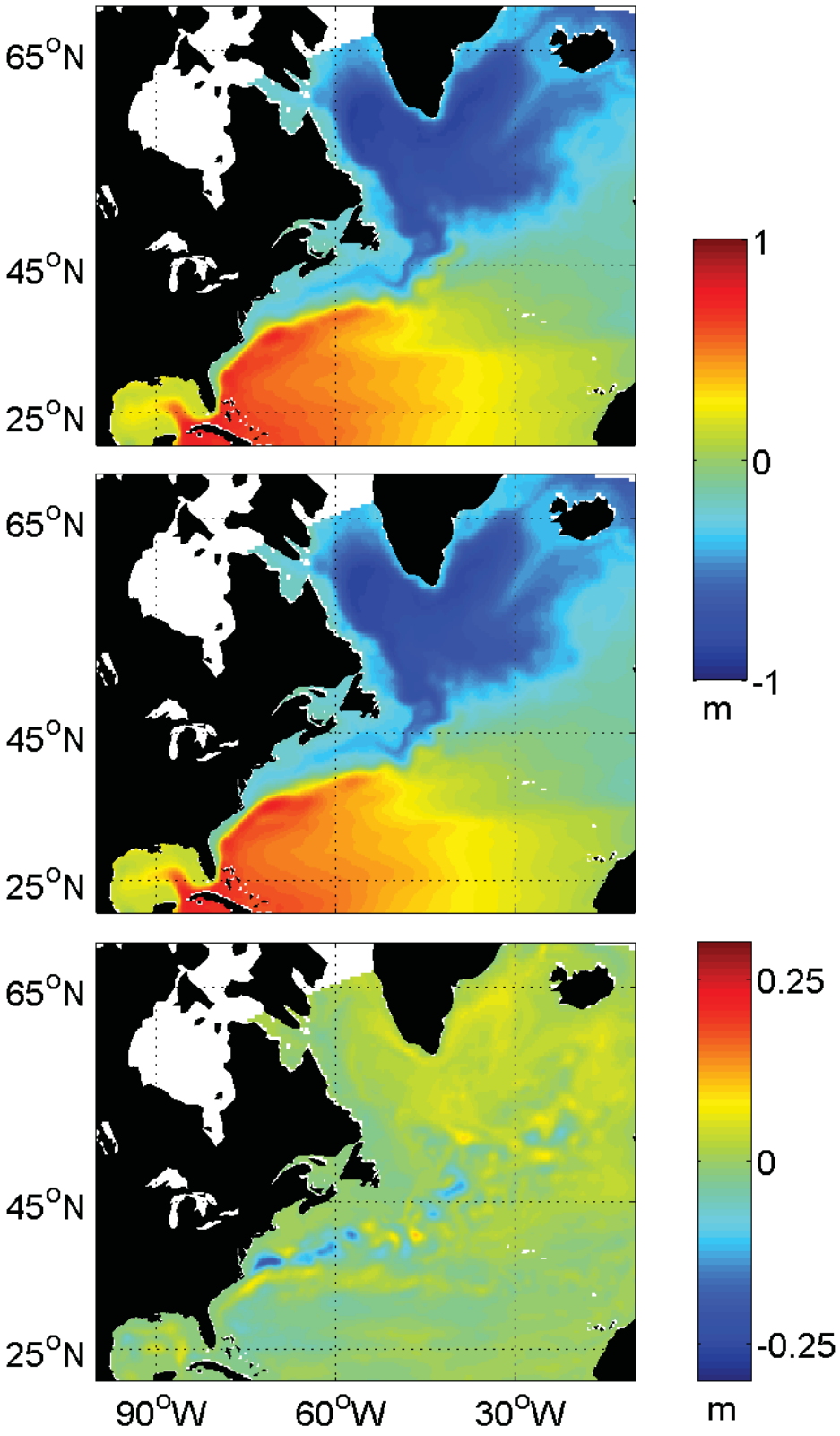
65°N
45°N
25°N
65°N
45°N
25°N
65°N
45°N
25°N
90°W
60°W
30°W
1
0
-1
m
0.25
0
-0.25
m

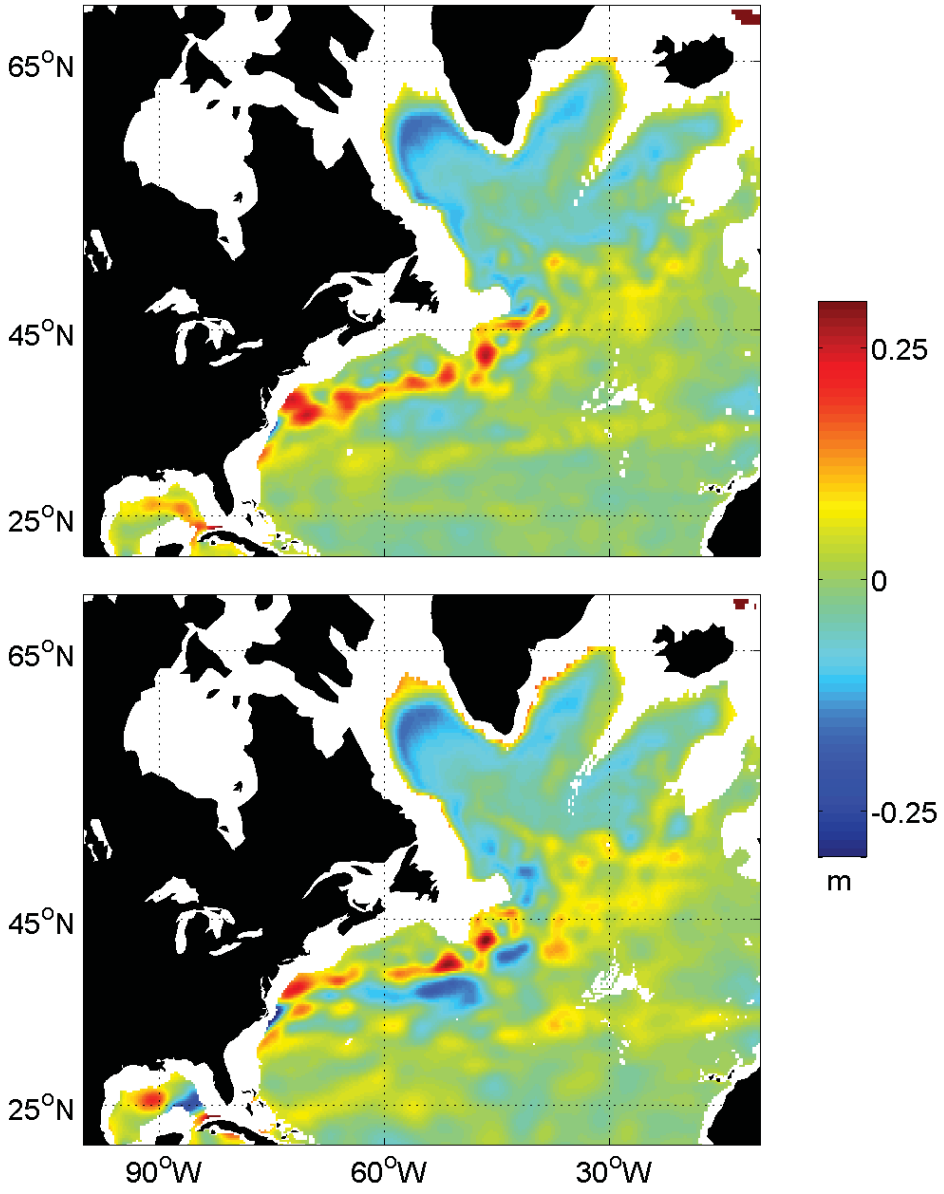

Figure 4.4: The differences between the oceanographic MDT estimation methods. (Top panel) The difference in MDT calculated using the WOA01 climatology, shown as the ocean model derived MDT minus the steric height MDT. (Bottom panel) The same, but calculated using the new Argo-period climatology.

4.6 Discussion

Estimates of the MDT produced using both the WOA01 climatology and the new Argo-period climatology have been presented, calculated using both the steric height and the ocean model approaches. Each of the estimates is broadly similar, but spatially coherent differences of 20 cm or more are noted in specific regions.

The Argo-period climatology produces a steeper gradient across the Gulf Stream between Cape Hatteras and the Grand Banks, which will produce a faster Gulf Stream when calculating the mean surface geostrophic circulation from the gradients of the MDT. Both calculation methods show higher MDT on the southern edge and lower on the northern edge compared to the WOA01 climatology. The Argo-period climatology also produces higher MDT in the interior of the subpolar gyre.

The ocean model method produces a more complete picture of MDT than the steric height approach, producing a MDT that extends into areas shallower than the steric height reference level. There are other differences between the two approaches, possibly related to deep ocean signals and eddy activity.

Whilst differences between the estimates are noted, it has not yet been considered whether one estimate is more realistic than another. The features of these MDTs will be examined in greater detail in subsequent chapters, validating the MDTs against the geodetic estimates from Chapter 2 and against other data. In Chapter 5 the focus will be the subpolar gyre region and in Chapter 6 it will be the Gulf Stream system and the subtropical gyre.

CHAPTER 5

THE NORTHWEST ATLANTIC SUBPOLAR GYRE

The dominant large-scale feature of the surface circulation of the northwest Atlantic is the subpolar gyre. This is a region where, because of remoteness and harsh conditions, in situ observations are especially sparse and hence new estimates of the mean circulation are especially useful.

Thompson et al. [2009] produced an estimate of the MDT and the mean circulation for this region using geodetic data. Their study produced good estimates in a number of areas, such as the Labrador Current, but they identified a number of spurious features in their estimate.

This chapter describes work undertaken to compare the new geodetic and oceanographic estimates of MDT and the mean surface circulation. The new estimates are compared with the earlier estimate by *Thompson et al.* [2009] and with other independent observations. Features in the mean surface circulation that have been poorly sampled using in situ measurements are identified, and the physical processes behind some of these features are examined.

5.1 The Subpolar Gyre

The northwest Atlantic subpolar gyre comprises a cyclonic circulation, with a warm, salty poleward flow (an extension of the Gulf Stream) and a return fresh, cold flow along the shelf at the western edge of the basin (e.g. *Lazier and Wright* [1993]; *Heywood et al.*

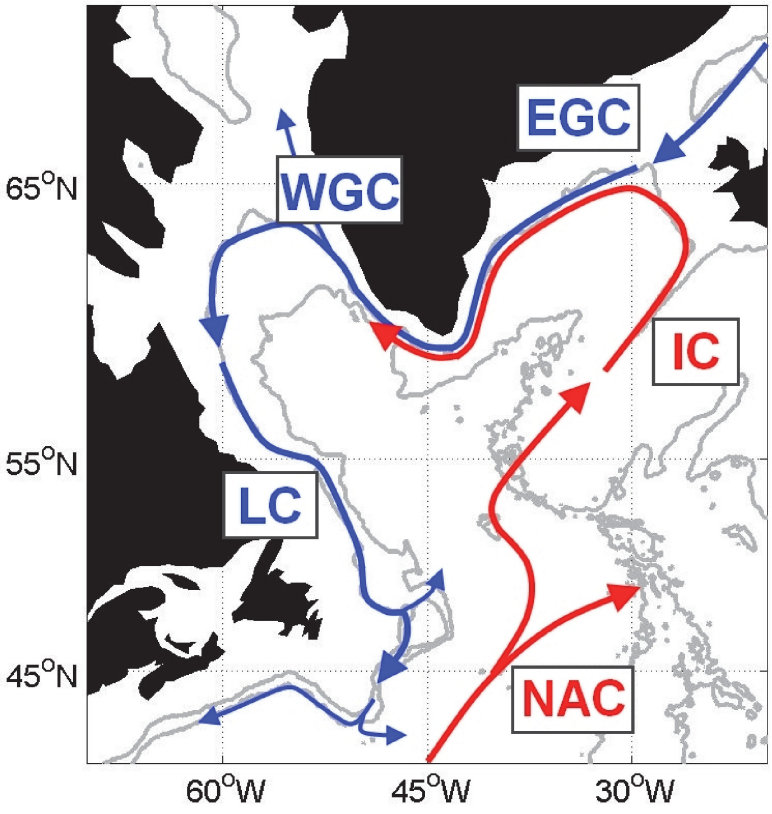

Figure 5.1: Schematic representation of the mean surface circulation of the northwest Atlantic subpolar gyre. The relatively warm currents are shown in red, the cold currents in blue. The labelled currents are the North Atlantic Current (NAC), the Irminger Current (IC), the East Greenland Current (EGC), the West Greenland Current (WGC) and the Labrador Current (LC). The grey lines are the 1000 m and 3000 m isobaths.

[1994]). The warm northward-flowing currents are the North Atlantic Current and the Irminger Current, and the colder return currents are the East Greenland Current, the West Greenland Current and the Labrador Current. A simplified representation of the circulation is shown in Figure 5.1.

The equatorward flowing currents of the subpolar gyre provide a pathway for the export of fresh water from high latitudes. Climate change may alter this fresh water flux, for example changing sea ice cover, river discharge, Greenland melting and the Arctic through flow (*Dickson et al.* [2007]). Modelling studies indicate that an increase in the freshwater flux can increase stratification of the interior of the subpolar gyre, including the Labrador Sea. This may reduce deep water formation and hence the strength of the meridional

overturning circulation (*Gerdes et al.* [2006]; *Stouffer et al.* [2006]; *Smith and Gregory* [2009]). *Smith and Gregory* [2009] showed that the effect is sensitive to the region of freshwater forcing and *Schmidt and Send* [2007] constructed freshwater budgets that showed the West Greenland Current is likely the dominant source of summer freshwater to the surface layer of the interior Labrador Sea. Monitoring the impact of climate change requires that we have an understanding of the circulation.

Although some southern parts of the gyre are well sampled, oceanographic observations in much of the gyre have been infrequent and biased toward the summer months because of geographic isolation and winter ice cover (*Bacon et al.* [2008]). Several sections are regularly sampled, for example the WOCE AR7W line between the coasts of Labrador and Greenland which is occupied annually by the Bedford Institute of Oceanography (*Yashayaev* [2007]). Float deployments have been used to map the circulation and water properties, for example the subsurface floats of the Labrador Sea Deep Convection Experiment (*Lavender et al.* [2000]). Other sampling is sporadic and sparse e.g. *Fratantoni and Pickart* [2007] noted only a handful of observations in the northern Labrador Sea between 1990 and 2001. Estimates of the mean circulation based on such sampling may be seasonally biased, and there may be significant aliasing of low frequency variability.

5.2 New Geodetic Estimates of the Mean Circulation

The production of new geodetic estimates of the MDT and the mean circulation is described in Chapter 2. The estimates are derived using a geoid model and an altimeter-derived mean sea surface height.

MDT estimates are produced using two new geoids from Natural Resources Canada – the PCG08I experimental geoid and the operational CCG2010 geoid. The PCG08I geoid is essentially an update of the geoid model used by *Thompson et al.* [2009], based on a combination of GRACE, altimeter and terrestrial gravity measurements, but with improved terrestrial measurements in some of the areas where *Thompson et al.* [2009] found spurious ocean circulation features. The CGG2010 geoid includes additional GRACE data and some GOCE data. (See Section 2.1.5 for a fuller description of both geoids.) In both cases

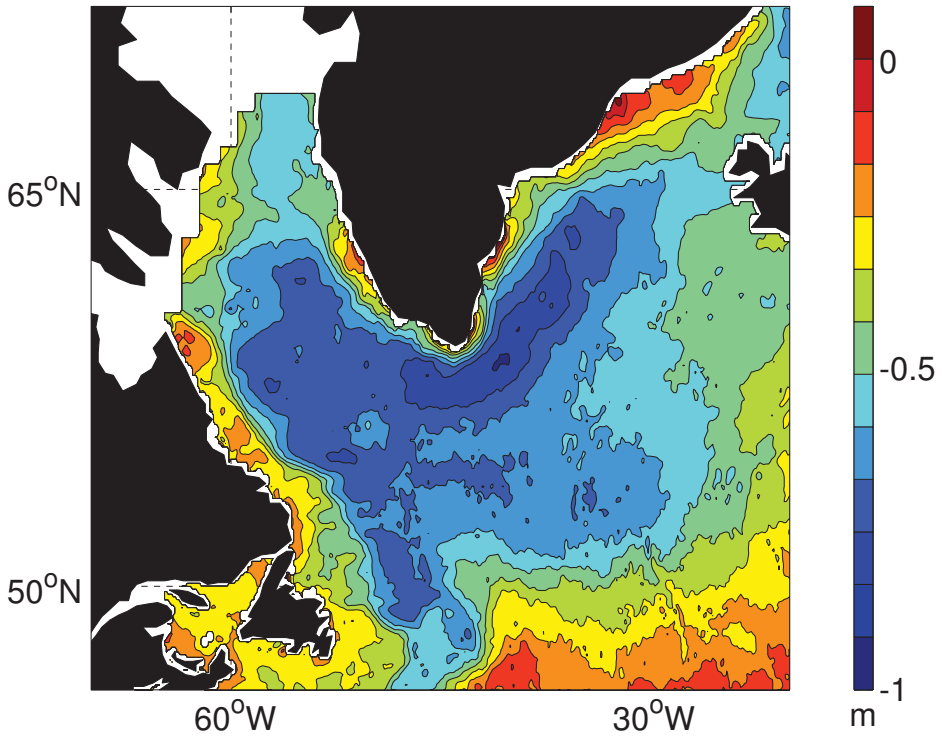

Figure 5.2: Mean dynamic topography of the northwest Atlantic subpolar gyre region derived from the PCG08I geoid (MDT_G). Areas within approximately $\frac{1}{4}^\circ$ of the coastline are excluded.

the altimeter-derived mean sea surface height is the MSS_CNES_CLS10 mean sea surface product distributed by Aviso, based on 16 years of altimeter measurements but adjusted to the 2000–2007 period to correspond with the reference period of the oceanographic estimate of MDT described in the next section.

In this chapter the focus is on the MDT produced using the PCG08I geoid. This provides a direct comparison with the *Thompson et al.* [2009] estimates, allowing an assessment of the improvement resulting from the improved terrestrial gravity data. The geoid and the mean sea surface are both defined in the mean tide system on a nominal $\frac{1}{30}^\circ$ grid. The MDT is calculated by pointwise subtraction of the geoid height from the mean sea surface height, with the MDT not calculated within approximately $\frac{1}{4}^\circ$ of the coastline and smoothed as described in Section 2.3. The MDT (MDT_G) is shown in Figure 5.2.

The subpolar gyre is a region where sea ice is present during part of the year, and in situ observations are heavily biased toward the summer months. The altimetric sea surface

height, which is used to construct MDT_G, is also seasonally biased but the areas affected by this are limited. This issue is discussed further in Appendix C.

The appearance of the ocean topography is broadly as expected. The low of the cyclonic subpolar gyre is clearly visible to the south of Greenland, and the high associated with subtropical waters south of the Gulf Stream is just visible at the southern edge of the domain. It is encouraging that the new MDT is smoother than the topography produced by *Thompson et al.* [2009] which contained a number of spurious features near Greenland.

The mean surface geostrophic speed is calculated from the gradients of MDT_G (Figure 5.3, bottom panel). This shows the shelf break current along the coasts of Greenland and Labrador with the Gulf Stream extension just visible around 45°W. The corresponding speed calculated from the gradients of the topography discussed in *Thompson et al.* [2009], MDT_{GO}, is shown in the top panel. A number of unexpected circulation features appear north of 55°N which do not appear in the speed plot derived from MDT_G.

5.3 New Oceanographic Estimate of the Mean Circulation

Oceanographic estimates of the MDT are described in Chapter 4. These are produced using both a steric height approach and an ocean model approach. The steric height approach is restricted to waters deeper than the reference level, chosen as 1500 m. This excludes the coastal shelves around Greenland and eastern Canada and a number of the currents that are shown in the geodetic estimate of the mean circulation (Figure 5.3, bottom panel). Only the ocean model estimate will be discussed for the remainder of this chapter, because it does not exclude these important coastal currents.

The ocean model approach uses an ocean circulation model that is spectrally nudged toward a TS climatology in the climatologically important frequencies but is allowed to evolve freely in other frequencies. Two oceanographic estimates are described in Chapter 4, one using the WOA01 climatology and the other using a new Argo-period climatology. The Argo-period climatology is based on data from the period 2000–2007 only, corresponding to the effective period of the mean sea surface height used to produce MDT_G. Accordingly

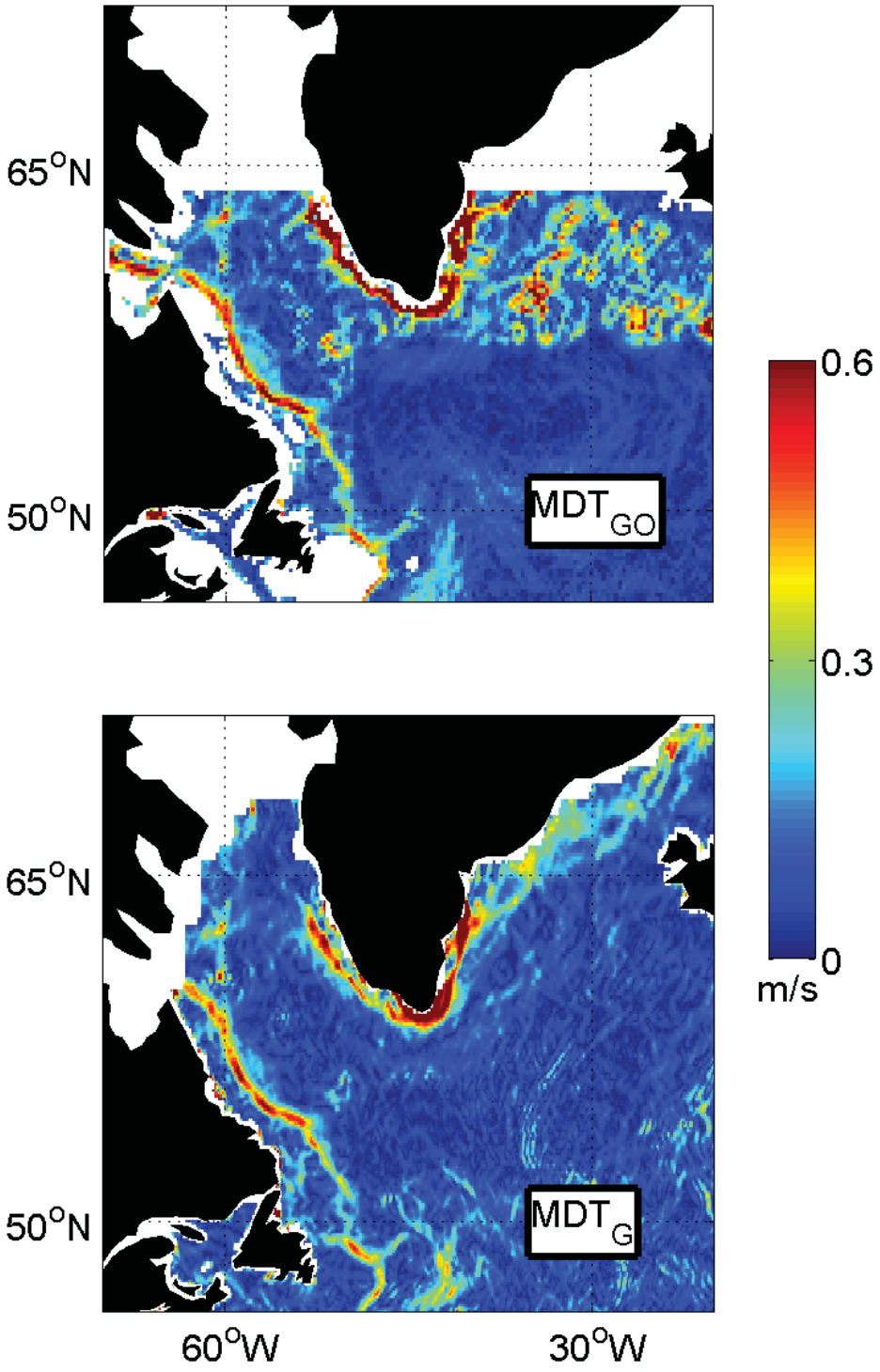

Figure 5.3: Total mean surface geostrophic current speed in the northwest Atlantic subpolar gyre region derived from the *Thompson et al.* [2009] geoid (MDT_{G0}, top panel) and from the PCG08I geoid (MDT_{G}, bottom panel). Areas within approximately $\frac{1}{4}^{\circ}$ of the coastline are excluded.

it is to be expected that the Argo-period climatology will be in better agreement with the geodetic estimate than WOA01, which is based on data collected over many decades.

As with other estimates of the MDT, these estimates may be biased toward summer values because of the presence of winter sea ice. The Argo profilers only operate in deep waters (>2000 m), which are less prone to sea ice. However the background used in constructing the climatology, which comes from WOA01, may have seasonal biases. This is discussed in Appendix C.

The oceanographic estimates of MDT are shown in Figure 5.4, with the top panel showing the estimate based on WOA01 (MDT_{WOA}), and the bottom panel showing the one based on the Argo-period climatology (MDT_{Argo}). Corresponding plots of the total mean geostrophic surface speed are shown in Figure 5.5. The speeds are calculated from the gradients of the MDT using the same method as for the geodetic estimates, described in Section 2.4

The two circulation estimates are very similar. The currents around Greenland are slightly better defined in the estimate based on the Argo-period climatology (MDT_{Argo}, Figure 5.5, bottom panel). This is also the estimate that corresponds with the effective period of the geodetic estimate, MDT_G, and so this estimate is used for the comparisons described in the later sections of this chapter.

5.4 Independent Oceanographic Observations

Although parts of the subpolar gyre are poorly sampled by in situ observations, a number of datasets exist which are useful for validating the geodetic and oceanographic estimates of the mean circulation described above.

5.4.1 Near-Surface Drifter Trajectories

The Global Drifter Program is an array of satellite-tracked surface drifting buoys designed to provide observations of mixed layer currents and sea surface temperature (*Lumpkin and Pazos* [2007]). The first large-scale deployments occurred in 1988, and the array achieved the target of 1250 drifters (an average 5° spacing) in 2005. The buoys are of various

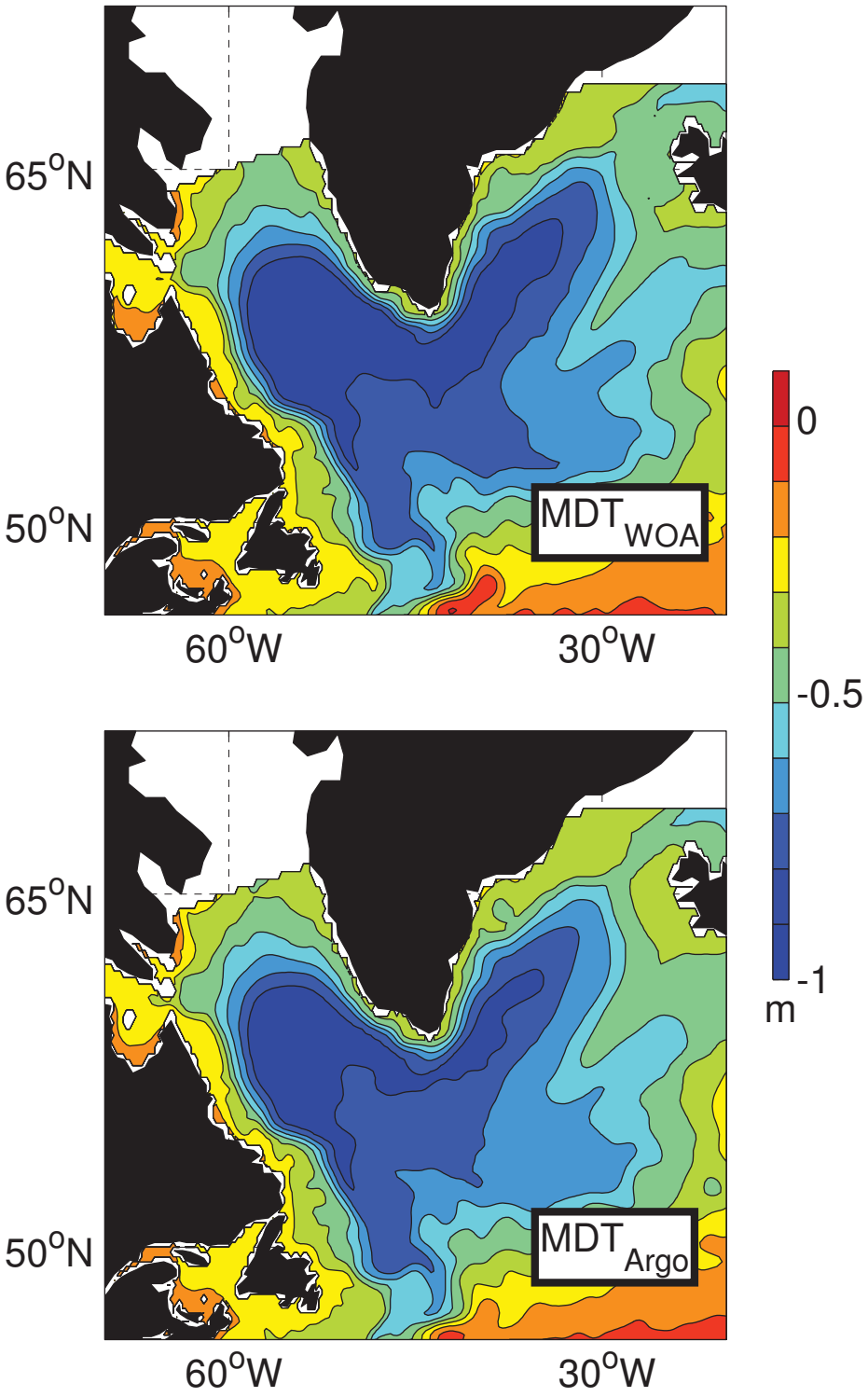

Figure 5.4: Mean dynamic topography of the northwest Atlantic subpolar gyre region derived using an ocean circulation model and the WOA01 TS climatology (MDT_{WOA}, top panel) and the new Argo-period TS climatology (MDT_{Argo}, bottom panel).

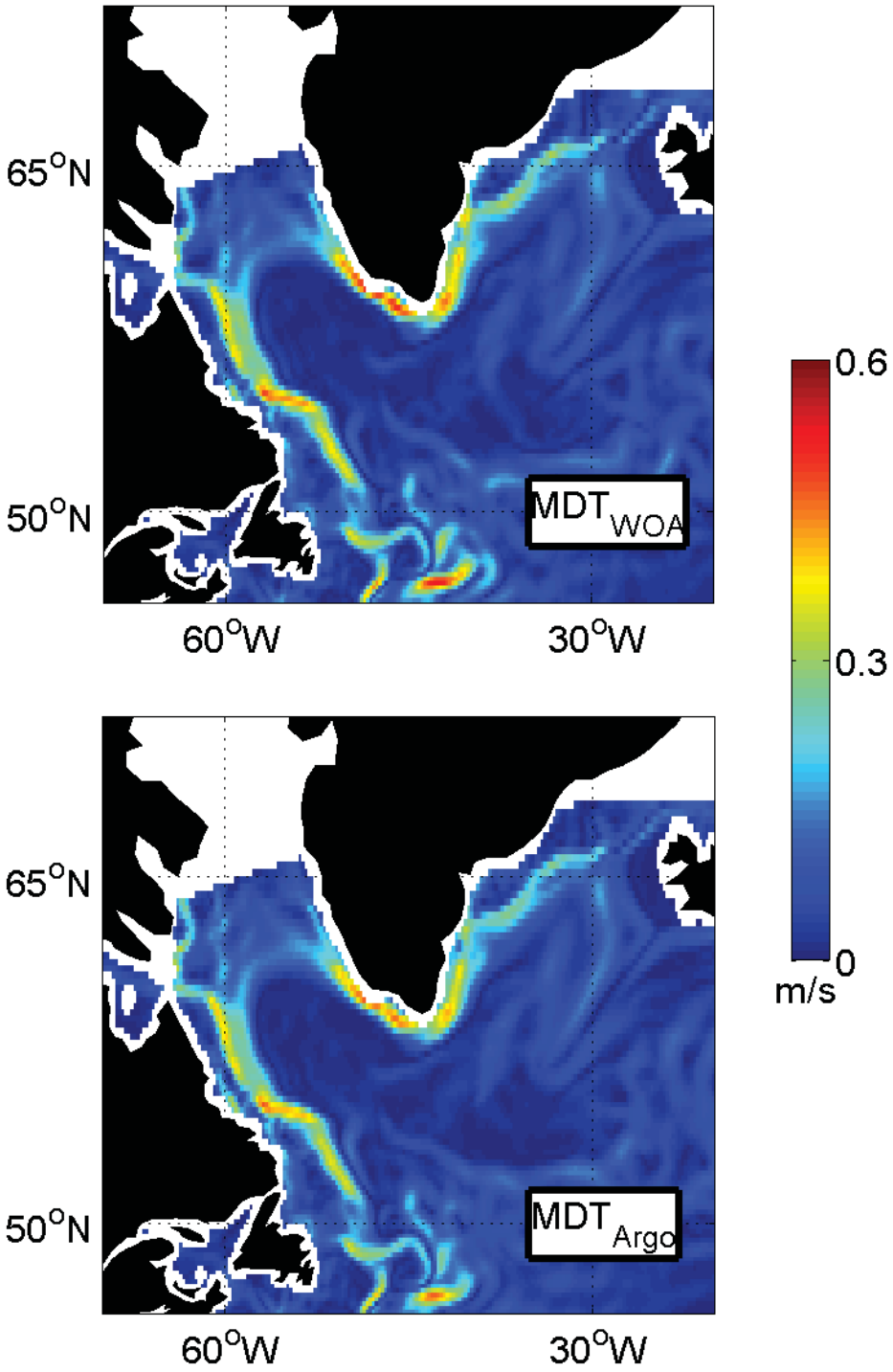

Figure 5.5: Total mean surface geostrophic current speed in the northwest Atlantic subpolar gyre region derived using an ocean circulation model and the WOA01 TS climatology (MDT_{WOA}, top panel) and the new Argo-period TS climatology (MDT_{Argo}, bottom panel).

designs but mostly comprise a surface float attached to a drogue at 15 m depth. Data are transmitted via the Argos satellite system, with the drifter position inferred from the Doppler shift of its transmission as the satellite passes over. The data are quality controlled by the Drifter Data Assembly Center and interpolated to a regular $\frac{1}{4}$ day interval.

For this study all drifter observations from 1991 to 2009 are analyzed. Drifters that have lost their drogue experience a greatly increased slip (lateral movements in a different direction to the current, caused by wind and wave effects) and these drifters are excluded from the analysis. The remaining observations are adjusted for Ekman drift using the technique of *Niiler and Paduan* [1995] and wind data from the NCEP/NCAR reanalysis project (*Kalnay et al.* [1996]). It should be noted that the adjustment technique of *Niiler and Paduan* [1995] was based on observations in the northeast Pacific Ocean and extrapolating this approach to the subpolar Atlantic may reduce the accuracy of the Ekman correction.

The adjusted velocities are binned and averaged on a $\frac{1}{4}^{\circ}$ grid by taking the mean of all drifters within $\pm\frac{1}{4}^{\circ}$ of each gridpoint. This averaging scheme is chosen so as to be comparable with the $\pm\frac{1}{4}^{\circ}$ differencing scheme used to calculate speeds from the oceanographic and geodetic MDTs. The total speed (Figure 5.6) is calculated from the mean velocity components.

Drifter observations from 2000 to 2007, corresponding to the Argo period, are analyzed using a similar technique. The standard error of the mean of the observations within individual bins is higher for this reduced dataset. Allowing for this increased uncertainty, the resulting circulation was broadly similar to the full dataset but with less complete coverage of critical regions. Accordingly the full dataset is used in the following discussions.

5.4.2 Regional Mooring and Ship-based Observations

There have been a number of recent regional studies which describe velocity observations made within the subpolar gyre. These include *Sutherland and Pickart* [2008] (the East Greenland Current and East Greenland Coastal Current), *Fratantoni and Pickart* [2007] (the West Greenland Current and Labrador Current), *Myers et al.* [2009] (the West Greenland Current) and *Bacon et al.* [2008] (the East and West Greenland Currents and the Labrador Current). Whilst observations from these studies are biased toward the summer months and mostly relate to short time periods, they are useful for validating drifter observations and they are discussed in the following sections.

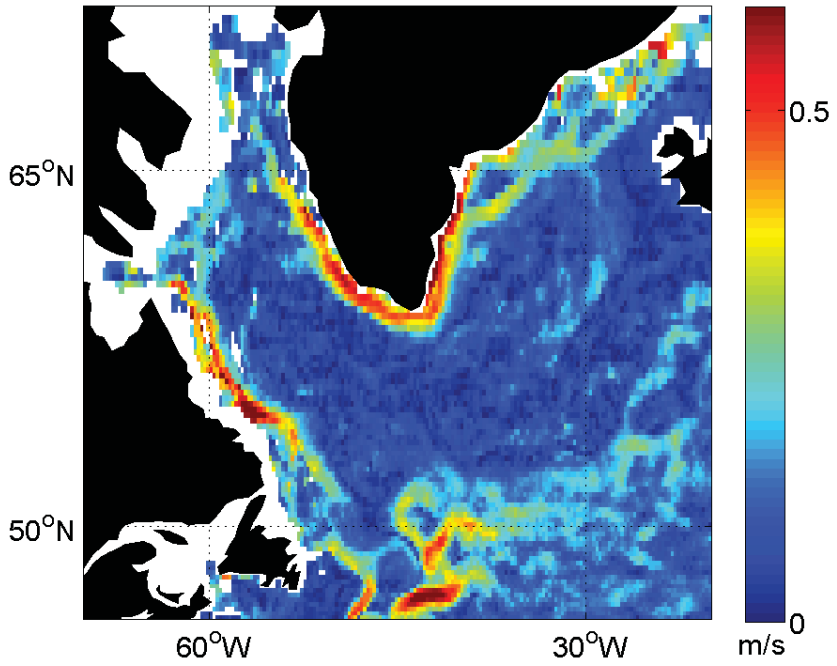

Figure 5.6: Total mean surface geostrophic current speed in the northwest Atlantic subpolar gyre region derived from drifter observations of the Global Drifter Program from 1991 to 2009. The observations are corrected for Ekman drift.

5.5 Evaluation of the New Geodetic Estimate

The mean surface circulation derived from MDT_G (Figure 5.3, bottom panel) shows relatively fast narrow currents along the coasts of Greenland and Labrador. The circulation from MDT_{Argo} (Figure 5.5, bottom panel) and from the surface drifters (Figure 5.6) show similar patterns. In each case the current around the south of Greenland is close to the coastline, reflecting the narrow shelf in this region. The path of the Labrador Current is similar in each and follows the shelf break. The current follows the edge of the Grand Banks off Newfoundland, with the North Atlantic Current entering the domain from the south at about 45°W. The current speeds are broadly similar for the MDT_G and drifter plots, but the MDT_{Argo} speed estimates appear to be a little lower in some areas.

In order to provide a more detailed and quantitative comparison a number of smaller regions are examined. These are identified in Figure 5.7.

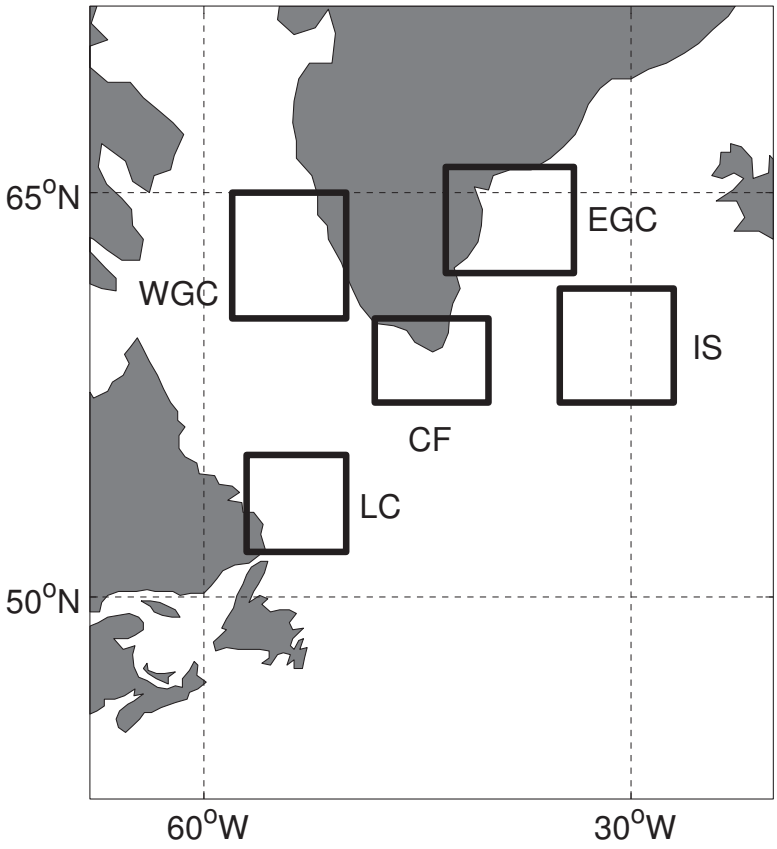

Figure 5.7: Location of the subregions examined in this section: East Greenland Current (EGC), Cape Farewell (CF), West Greenland Current (WGC), Labrador Current (LC) and Irminger Sea (IS).

5.5.1 The East Greenland Current

The East Greenland Current extends from the north-east of Greenland southwards along the coast to Cape Farewell (*Bacon et al.* [2008]) but this study will only consider the current south of Denmark Strait. The surface circulation is believed to comprise the main East Greenland Current (EGC) following the shelf break, with the Irminger Current (IC) alongside but further offshore, and a narrower current (the East Greenland Coastal Current, EGCC) on the shelf closer to shore (*Sutherland and Pickart* [2008]). The IC carries high-salinity Atlantic-origin waters, whereas the EGC and EGCC contain low-salinity Arctic-origin waters. *Sutherland and Pickart* [2008] examined six transects across the shelf occupied during the summer of 2004, together with other transects from 2002 and 2003. They identified the EGCC as a narrow (20-40 km wide) current on the shelf with speeds in the range 0.5-1 ms^{-1}. Their transects showed that the EGC follows the shelf edge with speeds in the range 0.1-0.5 ms^{-1}. They suggested that the EGCC is an inner branch of the EGC controlled by bathymetric steering whereas *Bacon et al.* [2008] proposed that it is a separate current formed mainly from sea ice melt.

Part of the East Greenland Current, labelled EGC on Figure 5.7, is considered in more detail in order to examine the strengths and weaknesses of MDT_G. Plots of current velocity vectors for each of the datasets are shown in Figure 5.8. The top right panel shows the mean surface currents estimated from drifters, and this is in broad agreement with recent descriptions of the current system (e.g. *Sutherland and Pickart* [2008]). Two currents can be identified, the EGC following the shelf edge (shown on this plot by the 700 m isobath), and the EGCC on the shelf much closer to shore. The two currents come together around 63°N where the shelf narrows, although other plots (not shown here) reveal that the currents separate again further to the south. The EGCC reaches speeds of about 0.5 ms^{-1}, and the EGC is somewhat slower and broader. The top left panel shows velocities derived from MDT_G and this shows a similar overall pattern. There is good agreement of current speed and position south of 63°N. To the north both currents are slower than the drifter estimates and the EGCC is located further from shore. This may point to a weakness in the offshore gravity data in this area. The third plot (middle left), derived from MDT_{Argo}, shows the position of the EGC, and part of the EGCC, in good agreement with the drifter estimates

although the speeds are generally slower. This is possibly due to the poor resolution of the climatology on the shelf, poor boundary conditions or inadequate atmospheric forcing. The cross-current section (bottom panel) illustrates the broad agreement between the three estimates for the position of the EGC and the differences for the EGCC noted above.

To provide a quantitative comparison statistics are provided for MDT_G, MDT_{GO} and MDT_{Argo} (Table 5.1). There is a reasonably high spatial correlation between MDT_{Argo} and MDT_G (r=0.82) but the standard deviation of the differences between the two fields is also fairly high (11.3 cm). MDT_G is a considerable improvement over the earlier geodetic estimate, MDT_{GO} described by *Thompson et al.* [2009]. The correlation between MDT_{GO} and MDT_{Argo} is 0.64, and the standard deviation of the differences is 15.9 cm, more than 30% higher than the corresponding figure for MDT_G.

Similar statistics of comparison are calculated for the alongshore component of the speeds derived from MDT_G and the drifter estimates (Table 5.2, see caption for details of the alongshore direction). As expected, the spatial correlation between the drifters and MDT_G is lower (r=0.67), and the standard deviation of the differences remains high (13.5 cms^{-1}). However MDT_G is again shown to be an improvement over MDT_{GO}. The correlation between MDT_{GO} and the drifters is 0.45 and the standard deviation of the differences is 16.9 cms^{-1}.

A small shift in the position of a current may result in poor statistics of comparison and, as noted previously, there is a difference in the position of the EGCC between MDT_G and the drifters on the shelf around 65°N. There are few direct observations of the EGCC in

---

Figure 5.8 *(following page)*: Estimates of the mean surface geostrophic flow for part of the East Greenland Current (62.5-65.75°N, 43-34°W, labelled EGC on Figure 5.7). Top left, middle left and top right: Velocity vectors derived from the spatial gradients of MDT_G and MDT_{Argo} and from surface drifter observations respectively. Vector size and colour are related to speed. The black line shows the position of the section plotted in the bottom panel and the grey line is the 700m isobath, representative of the shelf edge. Bottom: Mean surface current speed normal to the section plotted on the previous panels derived from the gradients of MDT_G (blue) and MDT_{Argo} (red) and from the surface drifters (black). The grey shaded area is the error for the drifter estimate, calculated as two times the standard error of the sample mean. The bathymetry and distance from shore are plotted beneath.

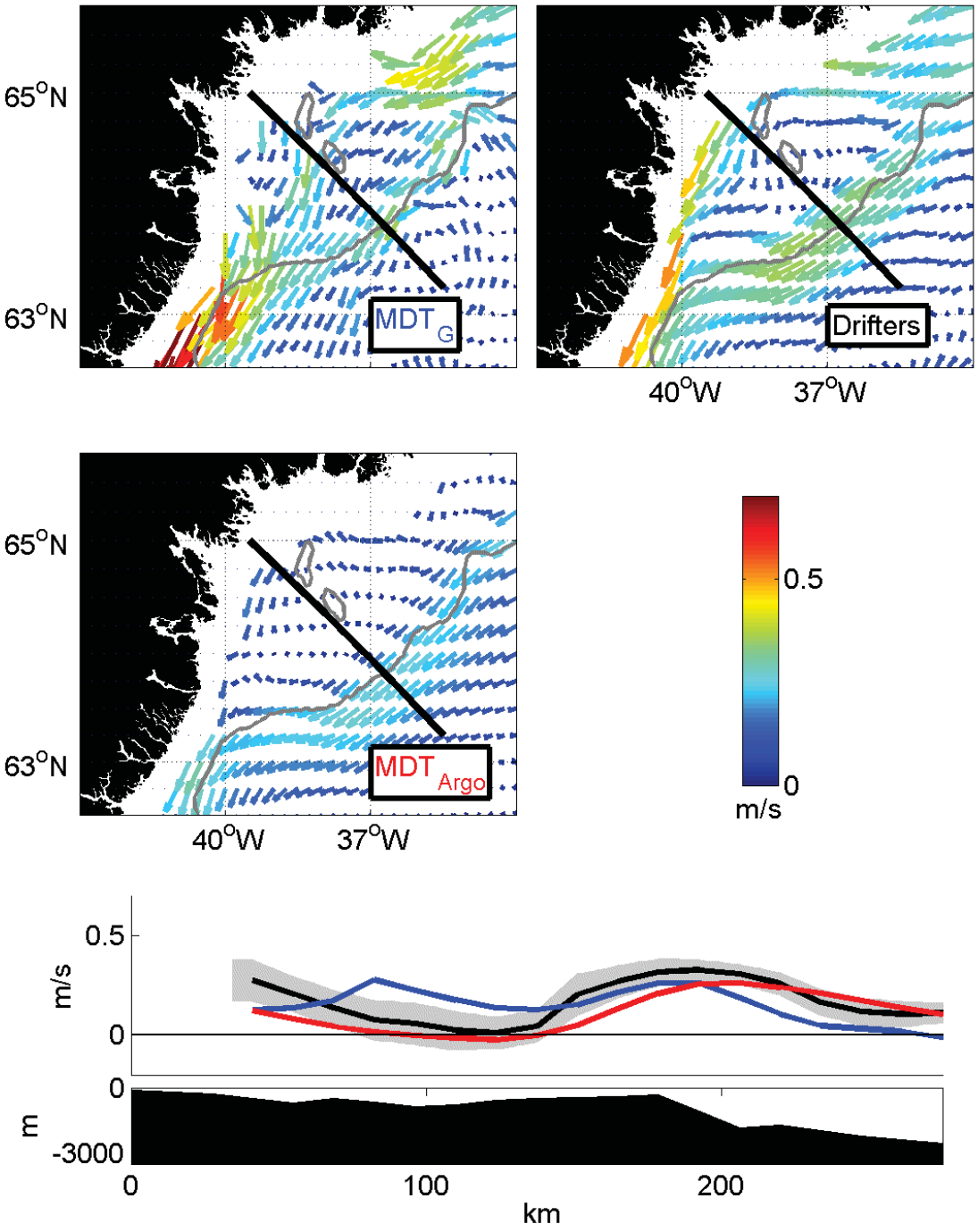
65°N
63°N
MDT G
Drifters
40°W
37°W
MDT Argo
0.5
0
m/s
m/s
0.5
0
m
0
-3000
0
100
200
km

Table 5.1: Comparisons of the sea surface topographies MDT_G and MDT_{GO} with MDT_{Argo} for each of the subdomains described in Section 5.5. The first five columns show the standard deviation (cm) of all gridpoints within each subdomain for MDT_{Argo}, MDT_G and MDT_{GO} and their differences. The final two columns are the correlation between MDT_{Argo} and MDT_G and between MDT_{Argo} and MDT_{GO}. The subdomains are shown in Figure 5.7.

	MDT_{Argo}	MDT_G	MDT_{GO}	MDT_{Argo} -MDT_G	MDT_{Argo} -MDT_{GO}	$r_{Argo,G}$	$r_{Argo,GO}$
EGC	15.9	19.6	20.6	11.3	15.9	0.82	0.64
CF	17.3	17.2	23.1	6.3	11.2	0.93	0.88
WGC	16.4	16.8	19.1	11.0	14.8	0.78	0.66
LC	20.9	20.6	22.2	4.9	5.3	0.97	0.97
IS	9.2	5.6	12.0	5.4	8.2	0.84	0.73

Table 5.2: Statistics of fit for the along-shore component of the speeds estimated from drifters and from MDT_G and MDT_{GO} for each of the subdomains described in Section 5.5. The first five columns show the mean and standard deviation (cms^{-1}) of alongshore speed at all gridpoints within each subdomain for drifters, MDT_G and MDT_{GO} and for their differences. Standard deviations are shown in parentheses. The final two columns are the correlations of alongshore speed between drifters and MDT_G and between drifters and MDT_{GO}. The subdomains are shown in Figure 5.7. Along-shore is defined as a bearing of 225° for EGC, 270° for CF, 330° for WGC and 150° for LC. For IS, which is open ocean, the statistics for zonal flow are shown.

	Drifters	MDT_G	MDT_{GO}	Drifters -MDT_G	Drifters -MDT_{GO}	$r_{D,G}$	$r_{D,GO}$
EGC	22.6 (17.4)	17.6 (18.2)	9.2 (18.6)	1.7 (13.5)	6.8 (16.9)	0.67	0.45
CF	14.7 (16.5)	10.9 (18.0)	4.8 (15.8)	2.6 (9.5)	3.5 (9.7)	0.85	0.79
WGC	14.5 (16.4)	11.0 (15.8)	6.4 (20.1)	3.2 (13.3)	4.4 (15.8)	0.67	0.64
LC	17.5 (15.0)	11.8 (14.6)	13.1 (12.4)	5.0 (10.3)	3.9 (10.0)	0.75	0.75
IS	5.5 (6.5)	3.1 (5.2)	3.4 (13.8)	2.4 (8.1)	2.1 (14.5)	0.05	0.12

this area and there are large uncertainties attached to the drifter estimates. *Sutherland and Pickart* [2008] included observations from summer 2004 close to 65°N (their Section 3) and they observed a jet between 25 and 30 km offshore. This is within the region close to shore where the geodetic technique is unable to accurately estimate MDT because of reduced accuracy of the satellite altimeter. On the other hand, their section does not extend out to the region where a jet is seen in the MDT_G data, 80-100 km offshore. It is possible that MDT_G is not observing the EGCC as defined by *Sutherland and Pickart* [2008], or that there is seasonality to the position of the current which they did not observe. This is an area for further study.

5.5.2 Cape Farewell

Holliday et al. [2007] described the circulation around Cape Farewell (the southernmost tip of Greenland) using data from a summer 2005 cruise. They found the EGC and EGCC merge again into a single current where the shelf widens directly to the south of Cape Farewell, in agreement with drifter observations described by *Cuny et al.* [2002]. The combined flow turns toward the northwest to form the West Greenland Current (WGC) with a partial subsurface retroflection feeding a recirculation in the Irminger Sea. *Clarke* [1984] deployed current meters in the Irminger Current south of Cape Farewell for 2 months during the winter of 1978 and found subsurface (100 m depth) currents flowing approximately westward with mean speeds of about 0.3 ms^{-1} near the shelf break and 0.15 ms^{-1} over the slope.

Figure 5.9 shows velocity plots for the Cape Farewell region. The drifter velocity estimate (top right panel) is in agreement with the description of *Holliday et al.* [2007]. The EGC and EGCC form a single current and follow the shelf break toward the northwest. The currents calculated from MDT_G (top left panel) follow a similar pattern although they are generally faster. The merged current has a mean speed of between 0.5 ms^{-1} and 0.7 ms^{-1}. This is in good agreement with the drifters described in *Cuny et al.* [2002], which ranged between 0.3 ms^{-1} and 0.9 ms^{-1} over the shelf, and a little faster than the subsurface measurements by *Clarke* [1984]. The currents derived from MDT_{Argo} (middle left panel) follow a similar pattern but speeds are lower, especially on the shelf. The

section plot (bottom panel) shows reasonable agreement south of Cape Farewell for all three estimates of the along-shelf current speed and position, although the measurements do not extend close enough to shore to capture the full current.

The statistics of comparison for MDT_G and MDT_{Argo} (Table 5.1) shows a high spatial correlation (r=0.93), and the standard deviation of the differences between the two fields (6.3 cm) is much lower than for the individual fields. Unlike the East Greenland Current region, MDT_G in this region is only a small improvement over the earlier geodetic estimate, MDT_{GO}. The correlation between MDT_{GO} and MDT_{Argo} is almost the same (r=0.88), but the standard deviation of the differences is somewhat higher (11.2 cm).

Similarly statistics of comparison of the alongshore velocity components from MDT_G and from the drifters (Table 5.2) show a high spatial correlation (r=0.85). There is only a small improvement in both correlation and standard deviation of the differences compared with MDT_{GO}.

5.5.3 The West Greenland Current

The West Greenland Current extends from Cape Farewell northwards along the west coast of Greenland. The current transports cold, fresh waters along the shelf and warmer, saltier waters (of Irminger Current origin) over the slope, with the strongest velocities over the shelf break (*Fratantoni and Pickart* [2007]). There are few direct measurements of the velocity of the current (*Myers et al.* [2009]) but drifter estimates include 0.7 ms^{-1} near Cape Farewell decreasing to 0.4 ms^{-1} near Fylla Bank (*Krauss* [1995]) and maxima of 0.95 ms^{-1} near Cape Farewell decreasing northwards to 0.7 ms^{-1}, and a mean velocity of 0.35 ms^{-1} (*Cuny et al.* [2002]). *Fratantoni and Pickart* [2007] estimated a mean summer velocity in excess of 0.3 ms^{-1} using TS observations and a thermal wind calculation. *Myers et al.* [2009] used an ocean model spectrally nudged to a TS climatology and estimated mean velocities decreasing from 0.3 ms^{-1} near Cape Farewell to 0.15 ms^{-1} off Fylla Bank. The current bifurcates with two branches turning to the west, approximately following the 1500 m and 3000 m isobaths, and the remnant West Greenland Current continuing northward toward Davis Strait (*Cuny et al.* [2002]).

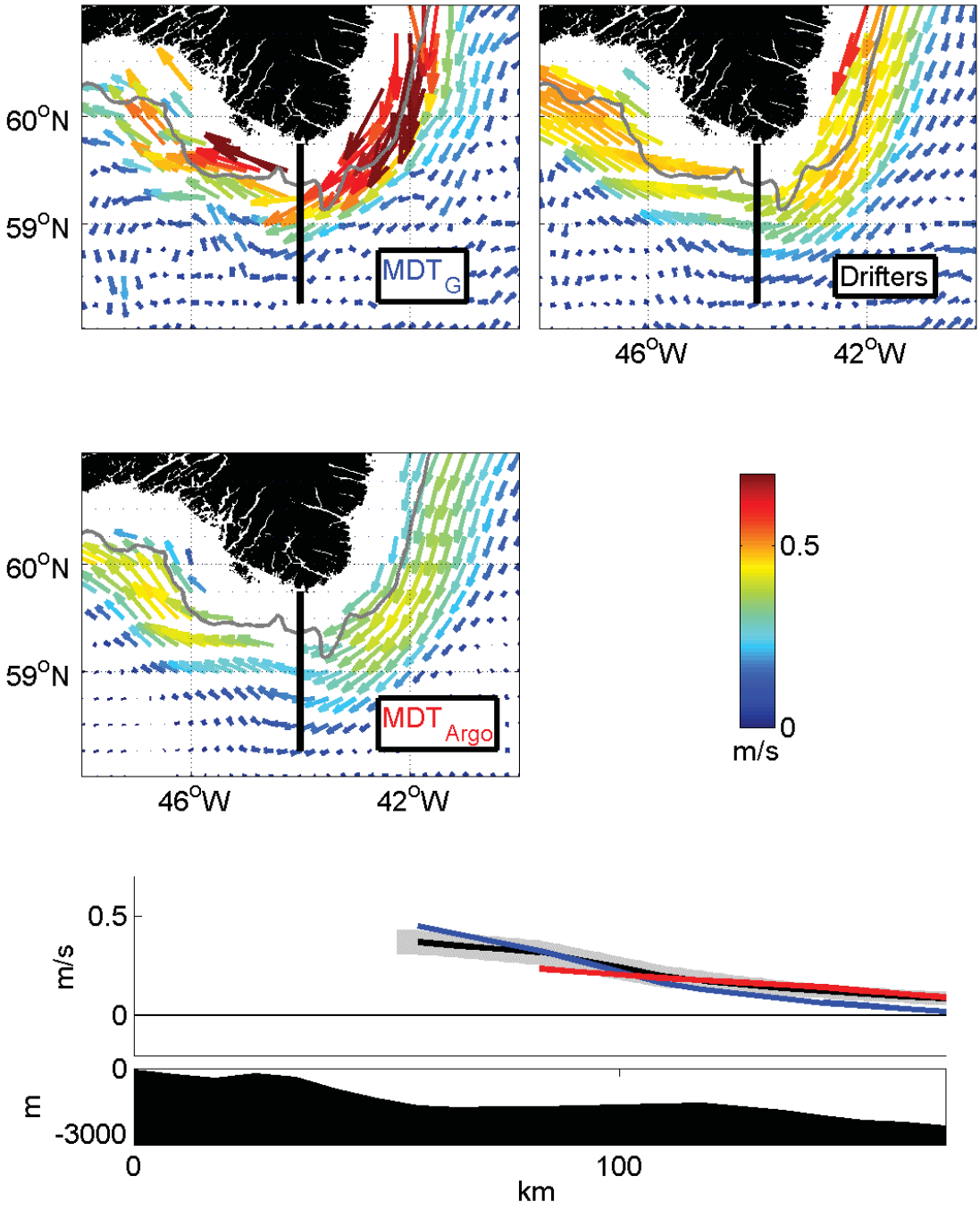

Figure 5.9: As for Figure 5.8 but for the Cape Farewell region (58-61°N, 48-40°W, labelled CF on Figure 5.7).

Figure 5.10 shows velocity plots for part of the West Greenland Current in the vicinity of Fylla Bank. The drifter velocity estimate (top right panel) shows a pattern similar to descriptions by, for example, *Cuny et al.* [2002] and *Fratantoni and Pickart* [2007]. The main West Greenland Current follows the shelf break, shown on these plots by the 700 m isobath, with mean speeds in the range 0.4-0.6 ms^{-1}. Bifurcation of the main jet can be identified, with branches of the current turning to the west approximately following the 3000 m and 1500 m isobaths but somewhat slower than the coastal current.

The velocity field derived from MDT_G (Figure 5.10, top left panel) shows a similar path and speed for the shelf break current, although north of 64°N the current is much slower than the drifter estimate. This may be related to the seasonality of the drifter observations since the drifter speed estimate is derived from just 13 floats, 10 of which passed through the region during the ice-free months of July to December. There is no sign of a bifurcation at the 3000 m isobath (near the southern edge of the domain) on the MDT_G plot but there is a weak branch of the current following the 1500 m isobath. The speeds derived from MDT_{Argo} are much weaker than the other estimates, although the main current still follows the shelf break. The flow almost disappears north of 64°N and flow on the shelf is very weak but the 1500 m bifurcation can be identified. The section (bottom panel) cuts across Fylla Bank, showing the main shelf break current and 1500 m isobath branch in the drifter speed estimates. There is good agreement with the speeds from MDT_G but the coastal current estimated from MDT_{Argo} is too weak.

With broad agreement on the position and strength of the WGC, the spatial correlation between MDT_G and MDT_{Argo} is quite high (Table 5.1, r=0.78). The standard deviation of the differences between the fields (11.0 cm) is much lower than the standard deviation of either MDT_G or MDT_{Argo}. These values are a significant improvement over the statistics comparing MDT_{GO} and MDT_{Argo} (r=0.66 and standard deviation of differences 14.8 cm).

The spatial correlation between MDT_G and the drifters is somewhat lower (Table 5.2, r=0.67) and the standard deviation of the differences remains high (13.3 cms^{-1}). This is, at least partly, due to the relative strength of the bifurcation flows and the WGC north of 64°N in the drifter estimate. (For example, the correlation is higher when the area north

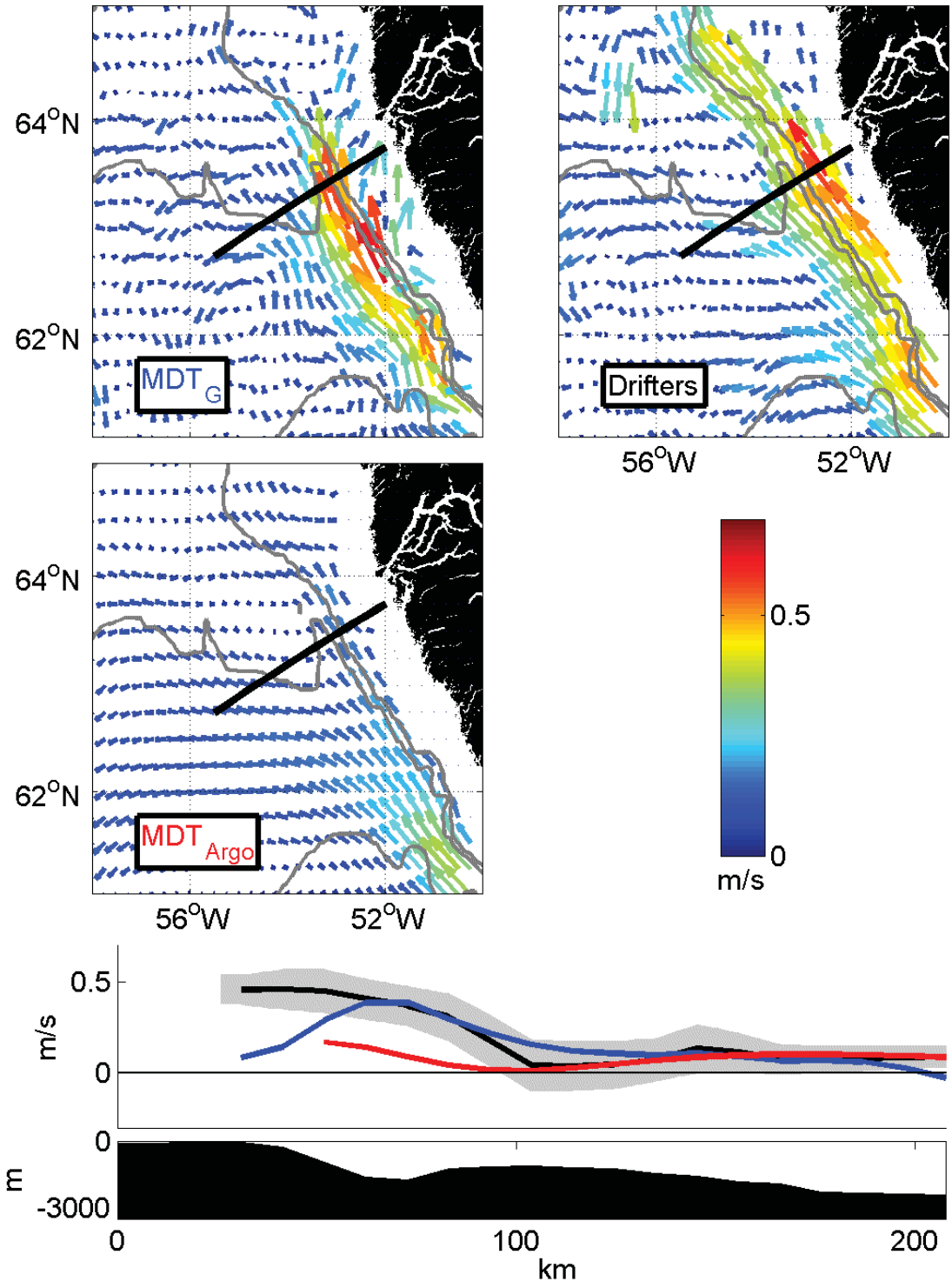

Figure 5.10: As for Figure 5.8 but for part of the West Greenland Current (61-65°N, 58-50°W, labelled WGC on Figure 5.7). The grey lines indicate the approximate position of the 700 m, 1500 m and 3000 m isobaths.

of 64°N is excluded). There are few observations in this region, but it is interesting that an analysis of surface drifters by *Cuny et al.* [2002] (their figure 4(b)) shows a surface circulation very similar to the MDT_G estimate. Their analysis indicates a rapid slowing of the WGC around 64°N and bifurcation speeds mostly 10 cms^{-1} or less. It is possible that the drifter analysis, based on a small number of observations, has overestimated the current speed in some areas, and that MDT_G is a better representation of the mean circulation.

5.5.4 The Labrador Current

Flow from the West Greenland Current turns to the south as it reaches the Labrador shelf, joining waters exiting Davis Strait and Hudson Strait to form the Labrador Current (*Loder et al.* [1998]). The current continues southward as far as the Grand Banks, bifurcating at the Tail of the Banks with part of the flow continuing southward and part joining the North Atlantic Current.

The Labrador Current has been the subject of more-intensive observation than the East and West Greenland Currents. For example *Lazier and Wright* [1993] described the structure and seasonality of the current around Hamilton Bank using data collected over 10 years from oceanographic sections and moorings. They described the main current located over the shelf break, with a maximum surface speed of 0.28 ms^{-1}, and a smaller inshore branch of the current, located over the shelf between Hamilton Bank and the coastline, peaking at 0.12 ms^{-1}. *Colbourne et al.* [1997] calculated a speed in excess of 0.3 ms^{-1} relative to flow at 500 m depth for the shelf break current near Hamilton Bank using TS data collected over more than 40 years, and a speed of less than 0.1 ms^{-1} for the inshore branch. *Lazier and Wright* [1993] observed seasonality to the current velocity, with a maximum in October and a minimum around March and April.

Figure 5.11 shows velocity plots for the region around Hamilton Bank. The plot derived from MDT_G (top left panel) shows the main shelf break current with mean speeds in the range 0.3-0.6 ms^{-1} and branches flowing onto the shelf either side of Hamilton Bank with speeds of 0.1-0.3 ms^{-1}. The structure of the currents and the speeds is in good agreement with the drifter estimates (top right panel) although the drifter speeds are a little higher where the current flows onto the shelf south of Hamilton Bank. However the drifter

estimates here on the shelf are based on relatively few observations (see Appendix C) and there are insufficient measurements to estimate velocities in the shallow water between the bank and the coast. The currents derived from MDT_{Argo} show a similar structure although speeds are generally lower along the shelf break. The cross-current section, which is just to the south of Hamilton Bank, shows good agreement between all three estimates for the position and speed of the main shelf break current but some differences on the shelf.

The spatial correlation between MDT_G and MDT_{Argo} is high (Table 5.1, r=0.97), and the standard deviation of the differences between the two estimates is low (4.9 cm). This correlation is identical to that between MDT_{GO} and MDT_{Argo}, which is to be expected since the geoid used by *Thompson et al.* [2009] incorporated much the same gravity data for this region as the new geoid. Similarly statistics comparing MDT_G and the drifters (Table 5.2) show that the spatial correlation is fairly high (r=0.75), again unchanged from the correlation for MDT_{GO}.

Bacon et al. [2008] suggested that the current on the shelf exists as a separate current system rather than a branch of the main Labrador Current, possibly originating with coastal meltwaters. However all of the estimates presented here show flow onto the shelf near 55°N and again near 54°N, indicating that the coastal current is at least partially formed from Labrador Current waters.

5.5.5 The Irminger Sea

For completeness, statistics of comparison are included for an area of open ocean within the Irminger Sea. This region was noted by *Thompson et al.* [2006] as one of the areas where their MDT contains spurious features because of poor gravity data.

The spatial correlation between MDT_G and MDT_{Argo} is high (Table 5.1, r=0.84), and an improvement over MDT_{GO} (r=0.73). The standard deviation of the differences is reduced from 8.2 cm for MDT_{GO} to 5.4 cm for MDT_G. The spatial correlation between MDT_G and drifters is near zero (Table 5.2, r= 0.05). This is a region of low current speeds but the drifter estimate has high variability and this may account for the low correlation. MDT_{GO} includes many erroneous circulation features which do not appear in MDT_G. The standard deviation of the zonal current estimates from MDT_G is 5.2 cms^{-1}, significantly less than the corresponding figure for MDT_{GO} (13.8 cms^{-1}).

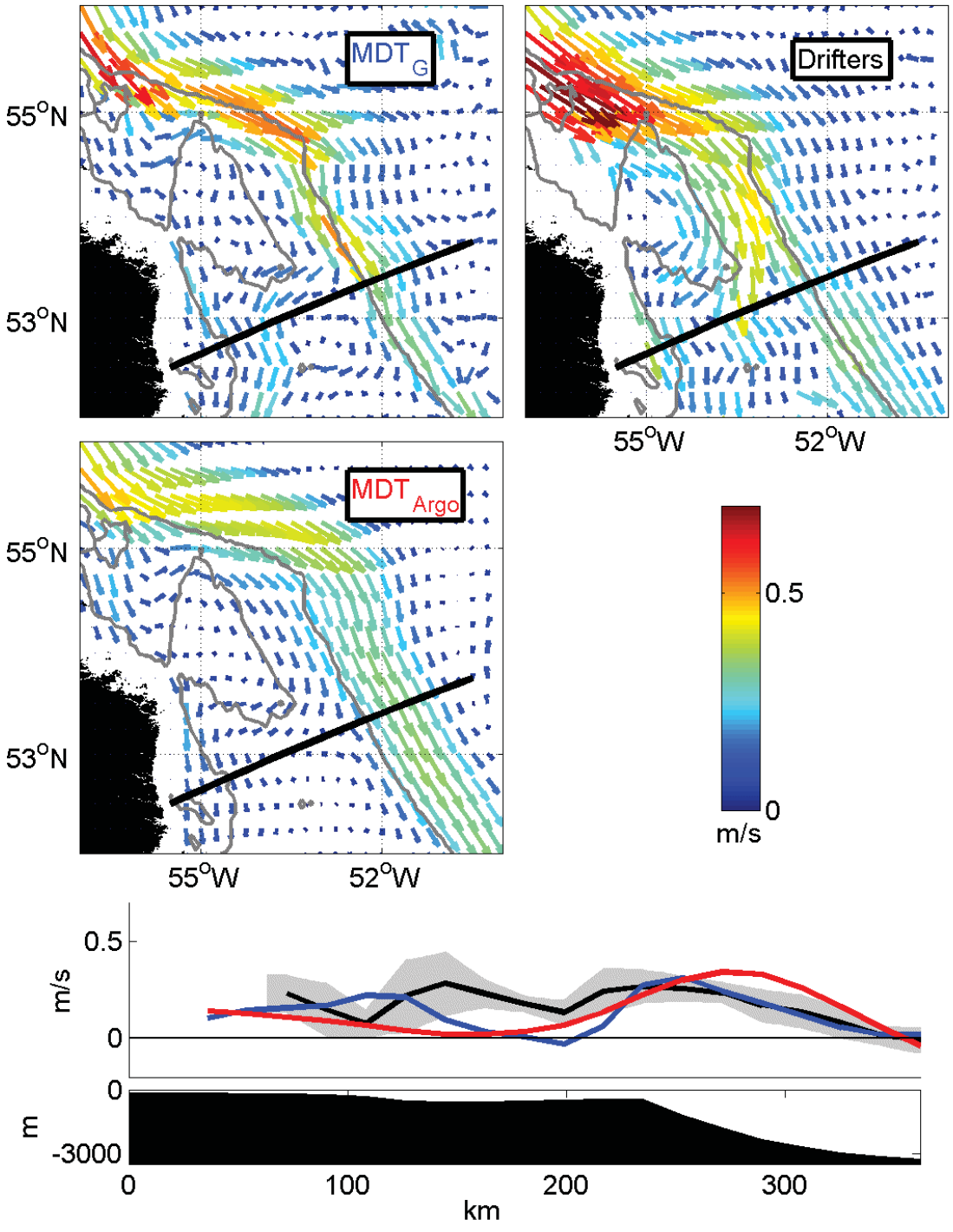

Figure 5.11: As for Figure 5.8 but for part of the Labrador Current (52-56°N 57-50°W, labelled LC on Figure 5.7). The grey lines are the 200m and 700m isobaths. Hamilton Bank is the shallow area centred near 54°N 55°W.

5.6 Discussion

In this chapter new geodetic and oceanographic estimates of the MDT and the mean circulation are described for the subpolar gyre region. These estimates are cross-validated, and compared with in situ and drifter observations.

The geodetic estimate is an extension of the work of *Thompson et al.* [2009], who used satellite and terrestrial gravity measurements to produce good estimates of the Gulf Stream and Labrador Current. However they found spurious circulation features around Greenland, caused for example by high wave number variability in the geoid south of Iceland, and the narrow coastal currents around Greenland were poorly resolved. The new geodetic estimate uses improved gravity data and improved quality control. A visual comparison of the velocity estimates from the new mean dynamic topography (MDT_G) and those obtained from surface drifters and oceanographic observations indicates good agreement. The main features of the subpolar gyre surface circulation are apparent, and the current speeds are generally consistent with other estimates. The MDT is much-improved around Greenland and the spurious circulation features apparent in the earlier work are no longer present. The resolution of the coastal currents is improved, including the narrow (20-40 km wide) East Greenland Coastal Current.

A quantitative comparison of the old (*Thompson et al.* [2009]) and new geodetic topographies shows minor improvements in the Labrador Current, as expected given the minor changes to the gravity data in this region. Much larger improvements are seen around Greenland, where the gravity data was revised more extensively. For example the correlation between MDT_G and drifters for alongshore currents in the East Greenland Current region shown in Figure 5.7 increases from 0.45 for the old topography to 0.67. In the West Greenland Current the standard deviation of the differences between the new geodetic estimates of alongshore velocity and the drifter estimate is reduced by more than 40% compared with the *Thompson et al.* [2009] estimate.

The oceanographic estimate is produced using an ocean model spectrally-nudged to a new Argo-period TS climatology. Comparison of velocities derived from the geodetic estimate (MDT_G) and from the ocean model (MDT_{Argo}) shows broad agreement in deeper

waters over the shelf slope. However there is frequently poor agreement in shallow water on the shelf, with MDT_G in closer agreement with drifter and other estimates. This may be because the climatology used to nudge the model incorporates Argo data but defaults to the WOA01 climatology in shallow water where Argo does not operate.

One of the attractions of using these techniques to study the circulation is the possibility of obtaining multi-year mean values across a large geographic area. The altimeter and drifter measurements used in this study are subject to a seasonal observation bias, which may lead to a bias in the mean circulation estimates. However the quantitative comparison of the topographies has been repeated using data restricted to the ice-free seasons and it does not seem to significantly alter the results for the scales and relatively short data record examined here. Further discussion of the seasonal bias in observations is included in Appendix C.

An interesting observation from these results is that both MDT_G and MDT_{Argo} show flow between the main Labrador Current and the coastal current. This indicates that the coastal current is, at least in part, formed as a branch of the main current rather than being of separate origin. A similar possibility arises with the East Greenland Current. There is some indication of flow between the main current and the coastal current in the estimate from MDT_G but it is a little less clear than for the Labrador Current. This may be the result of a weakness in the terrestrial gravity data or the nearshore altimeter data.

In conclusion the geodetic approach, using both GRACE and terrestrial gravity data, provides a realistic estimate of the mean dynamic topography, generally performing better than the oceanographic estimate. The resulting mean surface current speed estimates are comparable with in situ measurements and relatively small circulation features such as the East Greenland Coastal Current are resolved. The circulation close to shore may be improved by future improvements in the processing of altimeter data in the coastal zone.

CHAPTER 6

THE GULF STREAM AND THE SUBTROPICAL GYRE

The Gulf Stream is the dominant circulation feature of the subtropical gyre. It forms the boundary between the subtropical and the subpolar gyres, and is an important component of the meridional overturning circulation. It is one of the most intensively studied currents in the world's oceans. Its importance in the global and regional ocean circulation, together with its proximity to major oceanographic research centres, have motivated numerous observational and modelling studies.

Although the Gulf Stream system has been well described, modelling studies frequently fail to accurately reproduce the separation of the current from the North American coastline at Cape Hatteras (*Chassignet and Marshall* [2008]) and its subsequent path toward the Grand Banks. For example, a recent $\frac{1}{4}^{\circ}$ model study by *Tseng and Chien* [2011] showed unrealistic meanders downstream of Cape Hatteras. The spectral nudging technique was developed to achieve a realistic separation but this too can fail if the climatology to which the model is nudged has significant errors. *Thompson et al.* [2009] described results from a spectrally nudged ocean model and they speculated that unrealistic oscillations in the path of the Gulf Stream may have been caused by nudging toward a climatology that had aliased observed TS variability.

The construction of a new Argo-period TS climatology is described in Chapter 3. This is intended to more accurately represent the mean state of the ocean for the period 2000–2007

than a traditional multi-decadal climatology, and hence contribute to an improvement in the spectrally-nudged model representation of the Gulf Stream downstream of Cape Hatteras.

In this chapter the representation of the Gulf Stream in a new oceanographic estimate of the MDT is evaluated. This MDT is based on the new Argo-period climatology. The improvement attributable to the new climatology is quantified, and the new oceanographic estimate is compared with geodetic estimates and with independent observations. Although the Gulf Stream downstream of Cape Hatteras is the main focus of this study, the comparison will extend to other regions.

6.1 The Gulf Stream System

The Gulf Stream starts in the Caribbean Sea (*Talley et al.* [2011]). Water from the North Equatorial Current flows westward and northward as the Caribbean Current and then the Yucatan Current, passing into the Gulf of Mexico. Flow continues as the Loop Current in the Gulf of Mexico, and exits to the North Atlantic through the Straits of Florida as the Florida Current. This is commonly considered the start of the Gulf Stream.

The Florida Current is narrow and intense as it passes through the Straits of Florida. The flow is constrained by the channel, which is only about 80 km across near Miami. The fastest currents, measured at a mean of 180 cms^{-1} by *Leaman et al.* [1987], are less than 20 km from the Florida coastline. The mean transport is 32 Sv (*Meinen et al.* [2010], 1 Sv equals 10^6 $\mathrm{m}^3\mathrm{s}^{-1}$), and the seasonal and interannual variability has been studied using measurements of motion-induced voltage in a submarine telephone cable (e.g. *Baringer and Larsen* [2001]). North of the Straits of Florida the shelf widens. The current follows the shelf edge, moving it further offshore from the northern Florida and Georgia coastlines. Surface current speeds are up to 200 cms^{-1} (e.g. *Cadden et al.* [2009]) and the transport increases because of recirculations and inflow from the Sargasso Sea. At Cape Hatteras mean surface speeds are still in excess of 160 cms^{-1} and total transport has been estimated at 93.7 Sv (*Leaman et al.* [1989]).

Beyond Cape Hatteras the Gulf Stream separates from the coastline, moving eastwards over deeper waters. The departure point migrates on seasonal and interannual timescales

(e.g. *Frankignoul et al.* [2001]), though the excursions are relatively small (20-30km typically). The current is no longer constrained by bathymetry, and meanders and rings develop. Surface current speeds remain high, up to 200 cms^{-1} (*Johns et al.* [1995]), and the transport increases to reach around 150 Sv south of the Grand Banks. The increase in transport mainly results from an increased depth to the current, with the surface speed and width fairly constant. This increase is fed by recirculations to the north and south.

At the Grand Banks the flow breaks into a number of smaller currents. One branch turns to the north to become the North Atlantic Current, which feeds into the subpolar gyre. *Clarke et al.* [1980] measured surface current speeds of about 50 cms^{-1} in the North Atlantic Current around 42°N, compared with 90 cms^{-1} just before the current splits. Another branch of the Gulf Stream continues eastwards, subsequently splitting into two eastward-flowing currents, one at around 42°N and the other around 35°N (*Talley et al.* [2011]). The northern branch weakens as it passes to the north of the Azores whilst the southern branch, the Azores Current, passes to the south of the Azores and on toward the coasts of Portugal and Morocco.

Although the Gulf Stream system has been monitored extensively, measurements tend to be for relatively short periods. Long term monitoring has been undertaken in the Florida Straits, leading to good estimates of the mean for specific time periods, but elsewhere the mean may be less well defined.

6.2 Estimates of the Mean Circulation

In this chapter new estimates of the MDT and the mean surface circulation are compared and their realism is assessed. These new estimates are described in the following sections.

6.2.1 New Geodetic Estimates

Two new geodetic estimates of the MDT are described in Chapter 2. These are derived using a geoid model and an altimeter-derived mean sea surface height. The first uses the PCG08I geoid model from Natural Resources Canada and the MSS_CNES_CLS10 mean sea surface distributed by Aviso. The MDT is shown for the western subtropical gyre region in Figure 6.1 (top panel).

The second estimate uses the CGG2010 geoid model and the same MSS_CNES_CLS10 mean sea surface product. The geoid model is also produced by Natural Resources Canada, but it additionally incorporates data from the GOCE satellite gravity mission. The MDT is shown in Figure 6.1 (bottom panel).

At first glance the MDTs do not look significantly different, although there appears to be a little more high wavenumber variability in the PCG08I estimate. On closer inspection there are features in the PCG08I estimate that are absent in the CGG2010 estimate. For example there is a feature to the north of the Bahamas, near 75°W, that only appears in the PCG08I estimate. Similarly there are features in the open ocean around 30°N 30°W which only appear in the first estimate.

The differences in the two estimates is clearer when the mean surface geostrophic circulation is calculated from the gradients of the MDT (Figure 6.2). The features noted above are clearly visible in the PCG08I estimate (top panel) but not in the CGG2010 estimate. These features do not correspond with the general circulation described earlier, and are likely erroneous. Other erroneous features can be seen in the speed plots. For example there is an apparent current flowing in an approximately north-south direction at 40°W. Also the Gulf of Mexico Loop Current is poorly defined in the PCG08I estimate.

It appears that the CGG2010 estimate is a more realistic representation of the surface currents in this region. This is not surprising because PCG08I was constructed primarily to study territory around Canada. Terrestrial gravity data were not included for the southern North Atlantic, so high wavenumber features are poorly defined. CGG2010 incorporates a combined satellite gravity model from the latest GRACE model and the first release GOCE model, and this improves high wavenumber features homogeneously over the whole region.

The CGG2010 geodetic estimate is used for discussions in the remainder of this chapter because it represents the main currents of the subtropical gyre better than PCG08I and has fewer erroneous features.

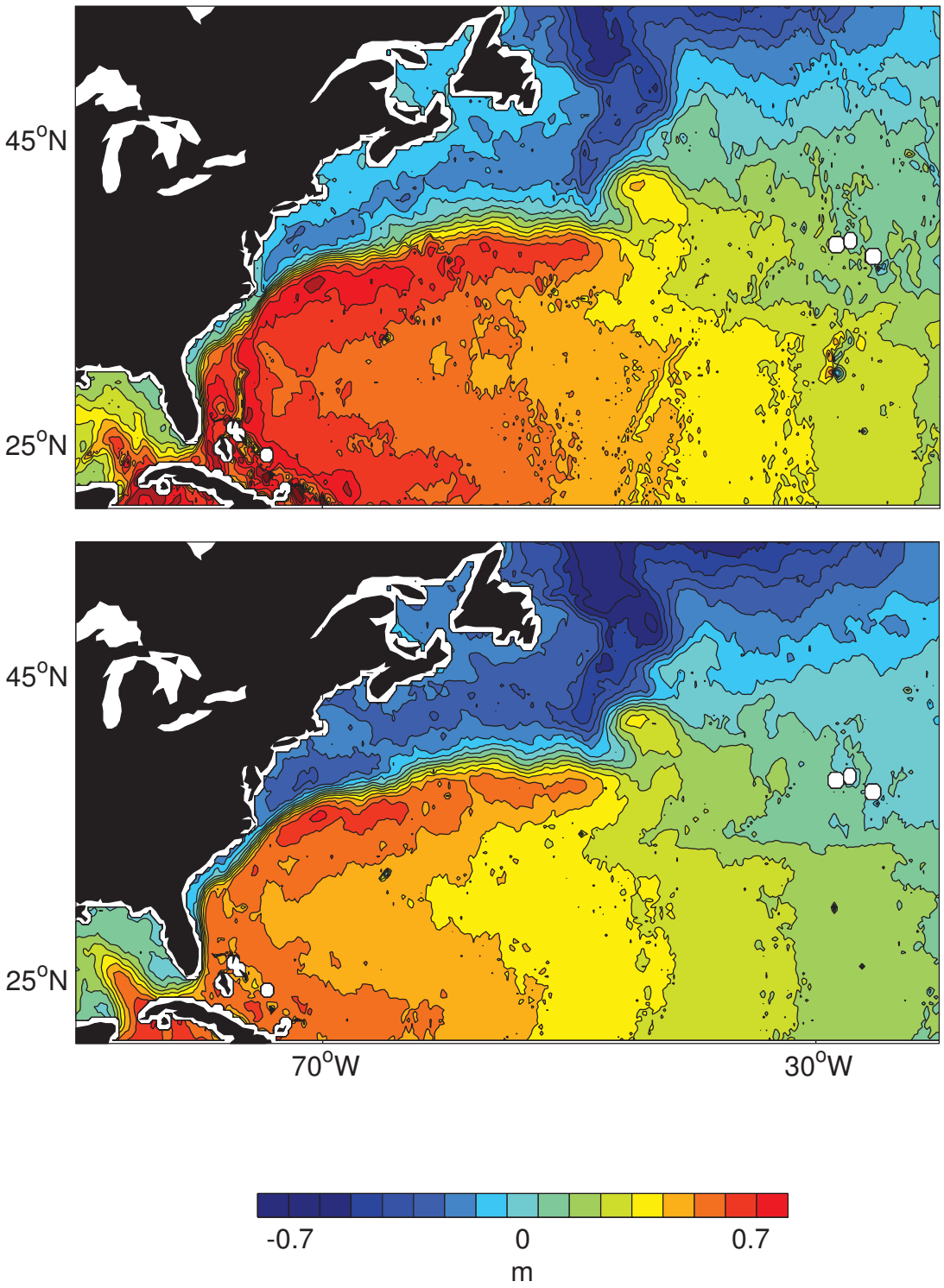

Figure 6.1: Mean dynamic topography of the western North Atlantic subtropical gyre region derived from the PCG08I geoid model (top panel) and the CGG2010 geoid model (bottom panel). Areas within approximately $\frac{1}{4}^{\circ}$ of the coastline are excluded because of potential errors in the altimeter mean sea surface (see Section 2.3).

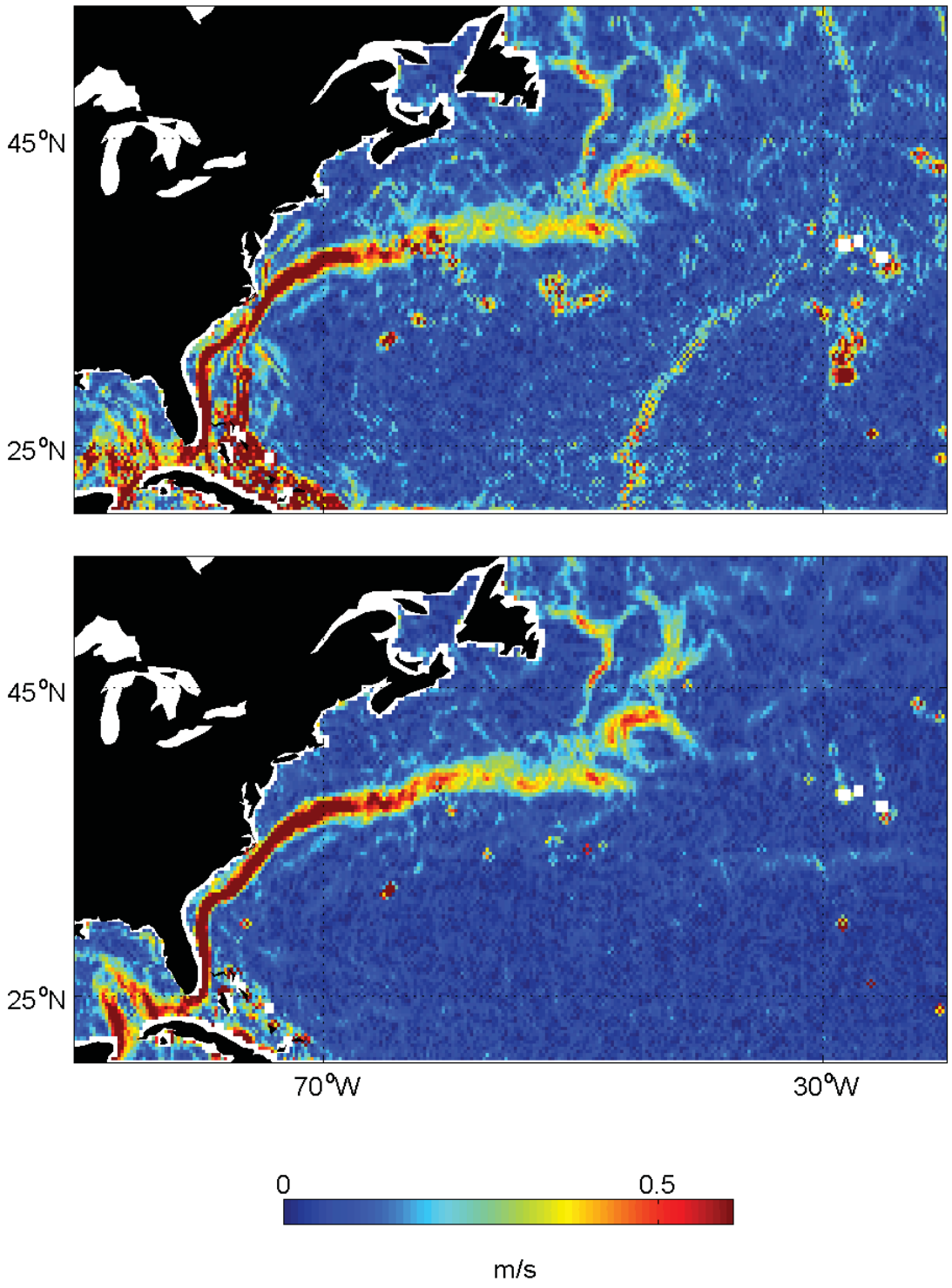

Figure 6.2: Total mean surface geostrophic current speed in the western North Atlantic subtropical gyre region derived from the PCG08I geoid model (top panel) and from the CGG2010 geoid model (bottom panel). Areas within approximately $\frac{1}{4}^{\circ}$ of the coastline are excluded.

6.2.2 New Oceanographic Estimates

New oceanographic estimates of the MDT and the mean surface circulation are described in Chapter 4. These are produced using both the steric height approach and the ocean model approach. The steric height approach excludes areas shallower than the reference level. A reference level of 1500 m was chosen in order to capture the main baroclinic signals, but this excludes large parts of the Florida Current and the Gulf Stream before it separates from the coastline of North America. Accordingly most of the discussions in this chapter refer to the oceanographic MDT estimates constructed using the ocean model approach.

The new oceanographic estimates are constructed using two TS climatologies. The first is the World Ocean Atlas $\frac{1}{4}^{\circ}$ climatology (WOA01, *Boyer et al.* [2005]). *Thompson et al.* [2009] speculated that erroneous meanders in the mean path of the Gulf Stream estimated using an ocean model spectrally nudged to a TS climatology may have been caused by the traditional multi-decadal climatology aliasing variability. The construction of a short-period climatology using Argo TS profiles is described in Chapter 3, and this was developed to reduce such aliasing. The second oceanographic estimate of MDT is constructed using this new Argo-period climatology.

The MDT estimates produced using the ocean model approach are shown in Figure 6.3, with the WOA01 climatology MDT in the top panel and the Argo-period climatology MDT in the bottom panel. The corresponding mean surface geostrophic speeds, estimated from the gradients of the MDT, are shown in Figure 6.4. At this scale the plots of MDT and geostrophic speed are broadly similar. There are slight differences in the path of the Gulf Stream as it breaks away from the coast of North America, and there are some differences in current speed. However estimates are broadly in line with the earlier description of the Gulf Stream system.

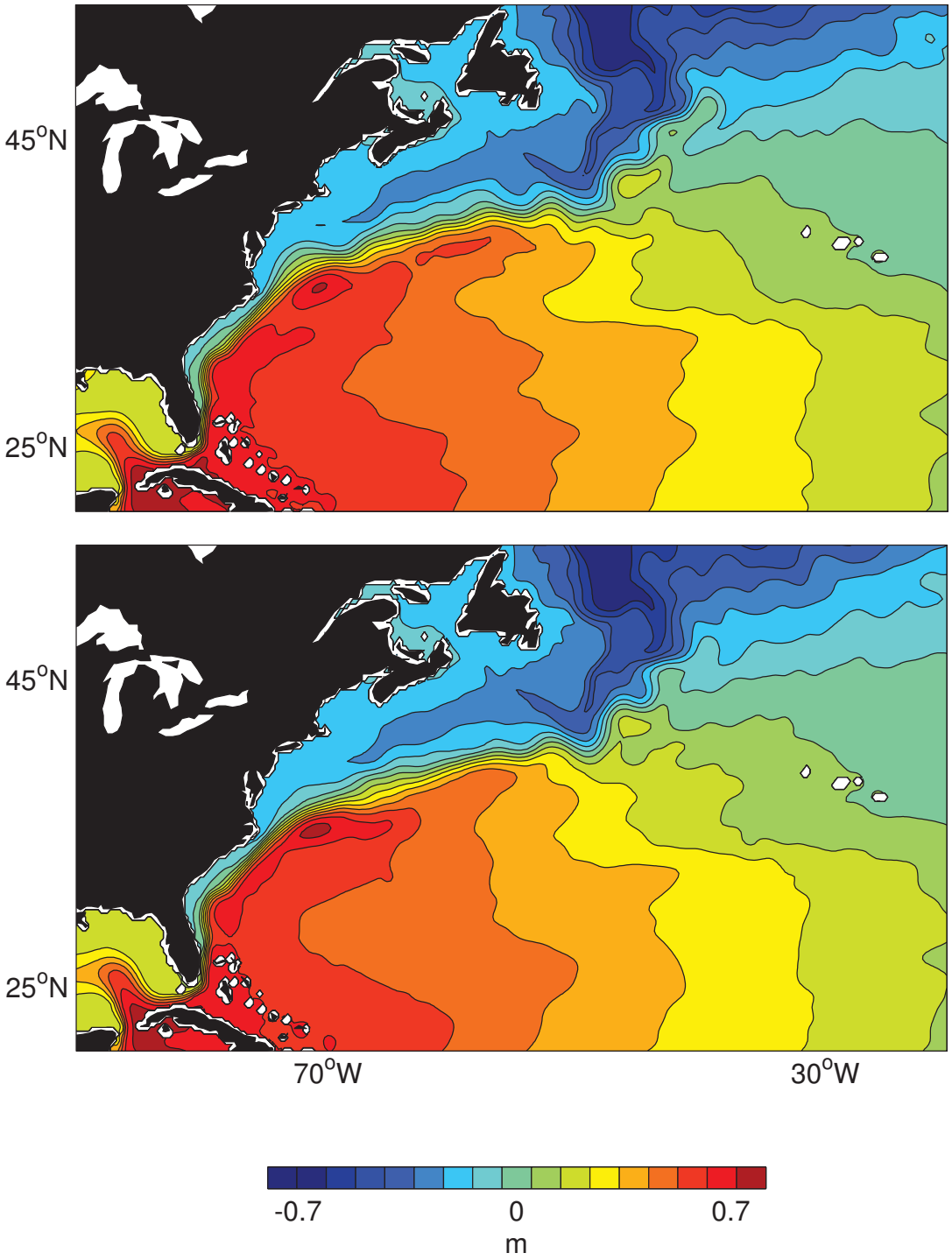

Figure 6.3: Mean dynamic topography of the western North Atlantic subtropical gyre region derived using an ocean circulation model and the WOA01 TS climatology (top panel) and the new Argo-period TS climatology (bottom panel).

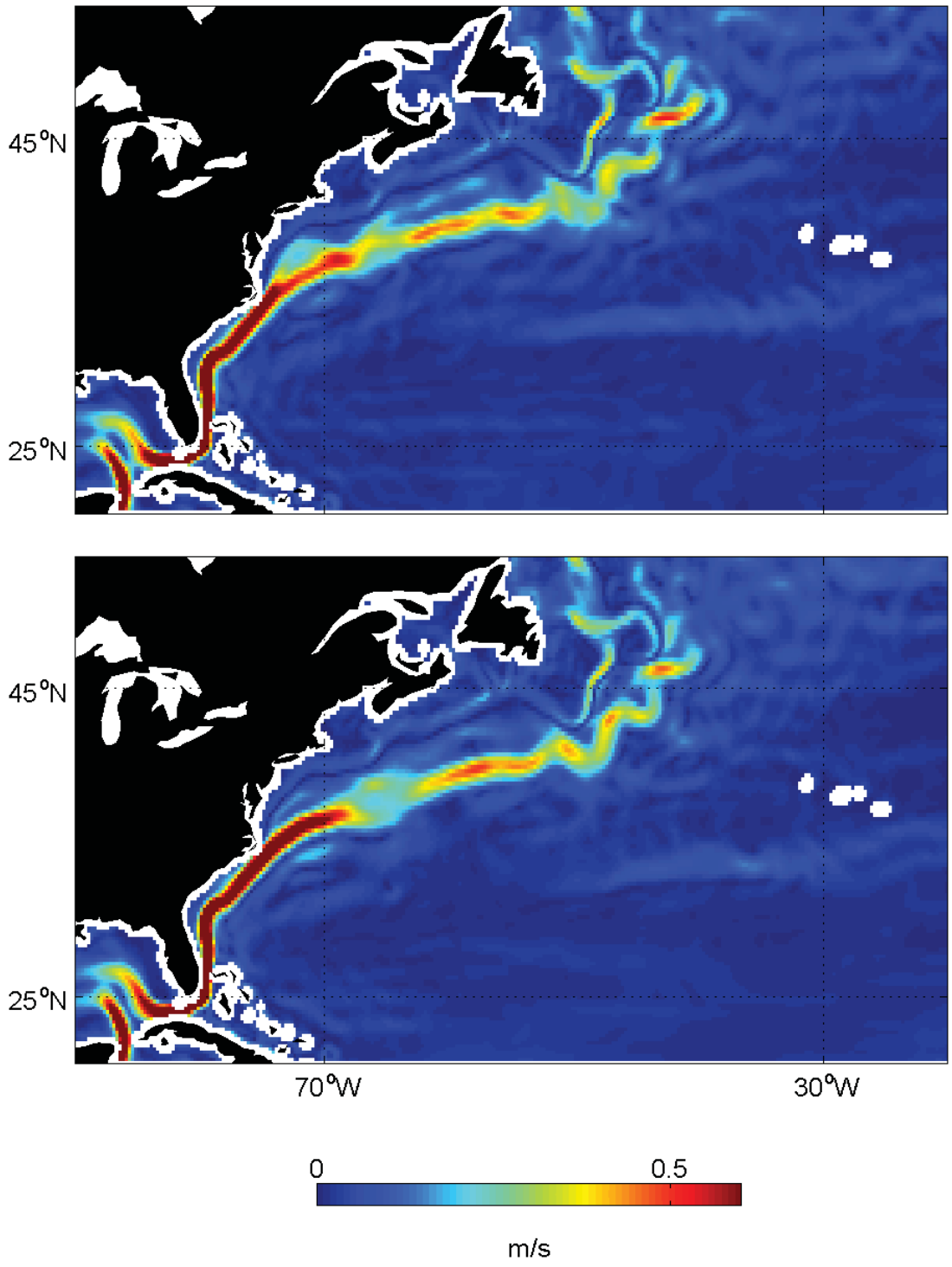

Figure 6.4: Total mean surface geostrophic current speed in the western North Atlantic subtropical gyre region derived using an ocean circulation model and the WOA01 TS climatology (top panel) and the new Argo-period TS climatology (bottom panel).

6.2.3 *Independent Observations*

This region has been extensively instrumented over many decades, and there are a large number of regional studies describing the surface circulation. Examples include studies by *Leaman et al.* [1989] in the Florida Current, by *Johns et al.* [1995] in the Gulf Stream downstream of Cape Hatteras, and by *Clarke et al.* [1980] in the Grand Banks region. Specific studies, selected as the most comprehensive for the regions of interest, will be referenced in later sections.

In addition surface drifter data are available from the Global Drifter Program (*Lumpkin and Pazos* [2007]), as discussed in Chapter 5. Figure 6.5 shows the mean surface speed from drifters from 2000 to 2007, corresponding to the time period of the oceanographic and geodetic estimates, and processed in the same manner as is described in Section 5.4.1.

6.3 Comparison and Evaluation of the Circulation Estimates

At the basin scale, the estimates from geodetic data (Figure 6.2), from oceanographic TS data (Figure 6.4) and from surface drifters (Figure 6.5) are all similar. The Gulf Stream system is clearly visible in all of the plots, from its origins in the Loop Current to the bifurcation at the beginning of the North Atlantic Current. The Florida Current passes very close to the coastline as it flows through the Straits of Florida and, since the geodetic estimate is masked within $\frac{1}{4}^\circ$ of the coastline, part of the current is missed by this estimate. This will be discussed further in the next chapter.

A pointwise comparison of the speeds from the CGG2010 geodetic estimate (MDT_G), the Argo-period climatology oceanographic estimate (MDT_{Argo}) and the drifters (Figure 6.6) illustrates two points. Firstly the histograms show that MDT_{Argo} includes more low values ($<$0.1 ms^{-1}) than the other estimates. This indicates that the MDT_{Argo} speed estimates are generally lower than the other estimates. Secondly the top two scatter plots show that there are a number of high values from MDT_G where the corresponding values from MDT_{Argo} and the drifters are close to zero. These "mismatches" are associated with a small number of erroneous mid-ocean features in MDT_G south of the Gulf Stream (see Figure 6.2).

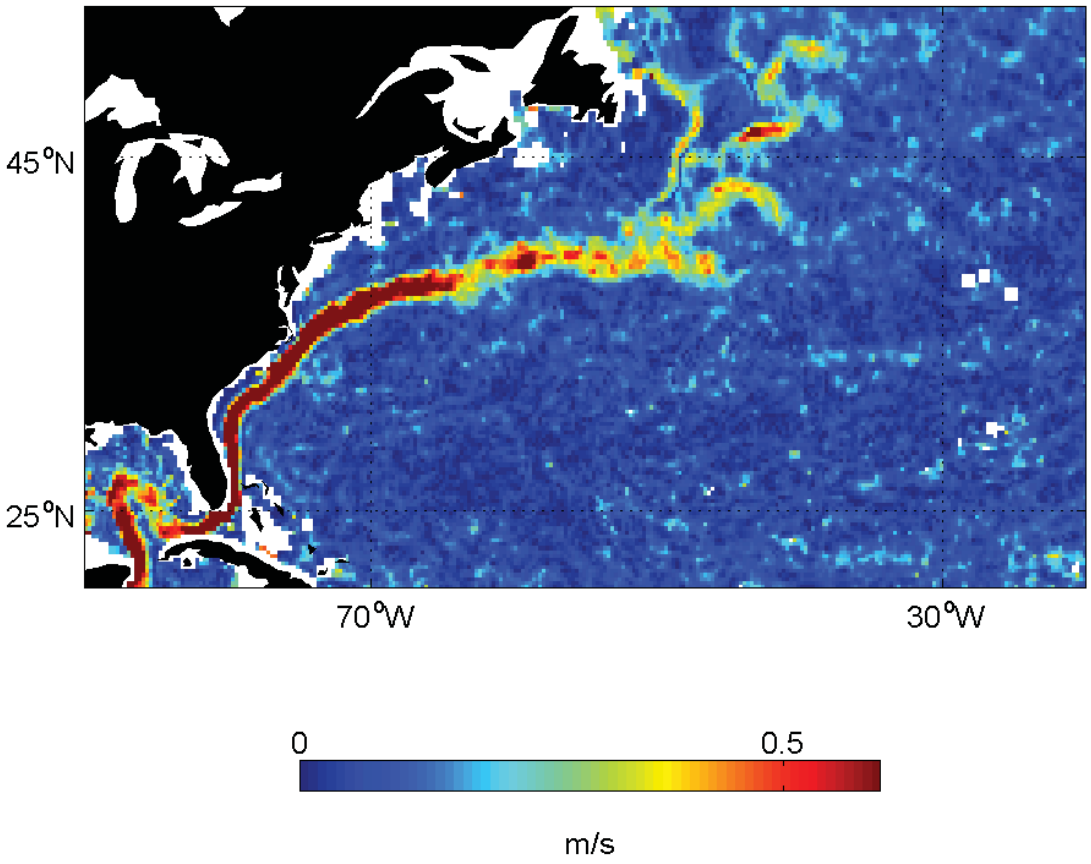

Figure 6.5: Total mean surface geostrophic current speed in the North Atlantic subtropical gyre region derived from drifter observations of the Global Drifter Program from 2000 to 2007. The observations are corrected for Ekman drift.

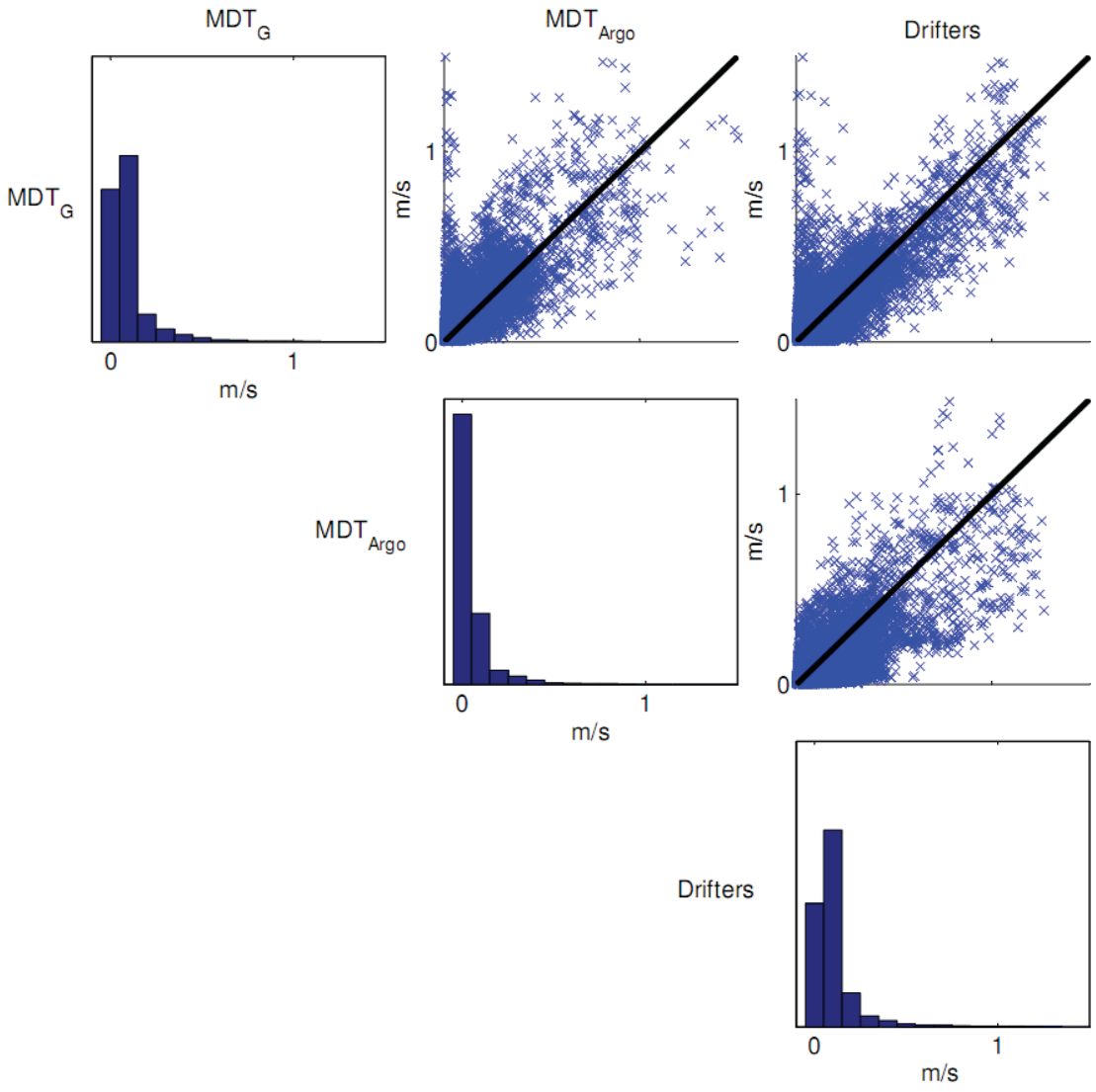

Figure 6.6: Diagonal panels: Histograms of current speed estimates at all gridpoints within the domain 20-50°N, 90-20°W, for MDT_G (top), MDT_{Argo} (middle) and drifters (bottom). Off-diagonal panels: Scatter plots comparing co-located speed estimates from MDT_G and MDT_{Argo} (top centre), MDT_G and drifters (top right), and MDT_{Argo} and drifters (middle right). The black line shows the 1:1 relationship.

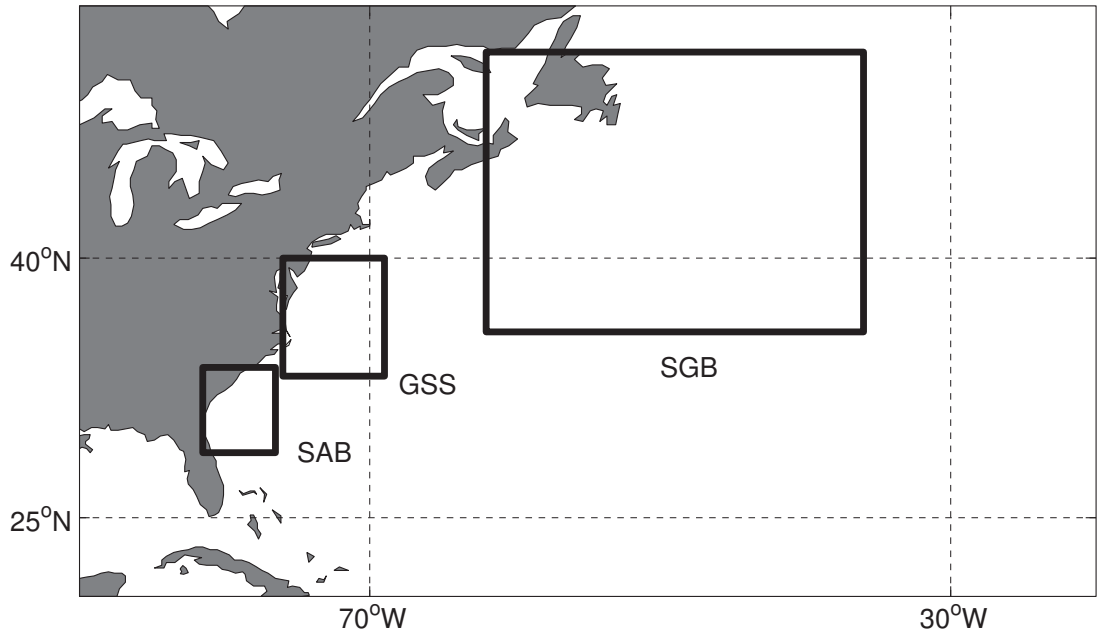

Figure 6.7: Location of the subregions examined in Section 6.3: South Atlantic Bight (SAB), the Gulf Stream separation (GSS) and the southern Grand Banks (SGB).

In order to provide a more-detailed comparison of the estimates, a number of smaller regions will now be examined. These regions are shown in Figure 6.7. Additionally there will be some comments regarding the Azores Current, which forms one of the pathways to close the subtropical gyre circulation.

6.3.1 The South Atlantic Bight

The South Atlantic Bight (SAB) is the shelf region between Cape Canaveral in Florida and Cape Hatteras. Travelling northward from the Straits of Florida, the shelf width (measured as the shoreline to the 100 m isobath) increases from almost nothing at Miami to approximately 50 km at Cape Canaveral. It continues to widen toward the north, reaching a maximum of approximately 130 km near Savannah, Georgia. The Gulf Stream follows the shelf break, and so it moves increasingly further offshore from Miami northward to the middle SAB.

Around 32°N the Gulf Stream is observed to be deflected offshore (e.g. *Brooks and Bane* [1978]). The deflection is associated with a topographic feature on the continental slope

called the Charleston Bump. This feature is evident in the isobaths plotted in Figure 6.8, clearest in the middle panel. Whereas the shelf break, marked by the 100 m isobath, follows the coastline, the 400 m isobath moves offshore between 32°N and 33°N. The deflection of the Gulf Stream is bimodal in nature (*Bane Jr and Dewar* [1988]), with weakly and strongly deflected modes. Weakly deflected is defined as the inner sea surface temperature front of the Gulf Stream remains inshore of the 600 m isobath, with strong deflections taking the front beyond the 600 m isobath for some tens of kilometres downstream.

South of 32°N, the geodetic estimate of the mean circulation (MDT_G, Figure 6.8, top left panel) shows the strongest flow of the Gulf Stream just offshore of the 100 m isobath. Current speeds are in excess of 100 cms^{-1}, lower than the measurements of, for example, *Leaman et al.* [1989] of 190 cms^{-1} at 29°N. The drifter estimate is very similar to the geodetic estimate and follows a near identical path (Figure 6.8, top right panel). The ocean model estimate produced using the Argo-period climatology (MDT_{Argo}, Figure 6.8, middle panel) is located further offshore and with speeds peaking at about 90 cms^{-1}. The reasons for this shift offshore are not clear but the ocean model estimate produced using the WOA01 climatology (not shown) is similar.

These results are illustrated by the section across the Gulf Stream (Figure 6.8, bottom panel). Although all of the speed estimates are lower than in situ measurements, this is likely due to the narrowness of the core of the jet. For example the measurements by *Leaman et al.* [1989] showed the maximum speeds to be in a region approximately 5 km across. All of the new estimates shown here have a horizontal resolution of $\frac{1}{4}^\circ$ but average across $\frac{1}{2}^\circ$, approximately 50 km at this latitude. Averaging the measurements of *Leaman et al.* [1989] across a 50 km width of the current yields an estimate that is less than 150 cms^{-1}.

Near 32°N MDT_G shows the Gulf Stream to move sharply offshore, approximately following the 400 m isobath. The middle of the strongest flow approximately follows the 600 m isobath (not shown on the figure) between 32°N and 33°N. This marks the position of the Charleston Bump, and is in agreement with the observations of *Brooks and Bane* [1978]. The path of the Gulf Stream along the 600 m isobath marks a mean pathway

between the two modes identified by *Bane Jr and Dewar* [1988]. The drifter estimate shows a similar deflection offshore, whilst the MDT_{Argo} estimate shows the deflection further to the south.

To provide a quantitative comparison statistics are provided for MDT_G and MDT_{Argo} (Table 6.1). There is a high correlation between MDT_{Argo} and MDT_G (ρ=0.96). Both MDT_{Argo} and MDT_G have a high standard deviation (32.6 cm and 30.5 cm respectively) but the standard deviation of the differences is much lower (8.6 cm), again indicating that there is good agreement between the estimates. Statistics are also included for MDT_{WOA}, and these show that MDT_{Argo} is only a slight improvement over the WOA01 estimate. For example the standard deviation of the differences between MDT_{Argo} and MDT_G is 10.2 cm compared with a difference of 11.7 cm between MDT_{WOA} and MDT_G

Statistics of comparison are similarly calculated for the along-current component of the speeds derived from MDT_G and the drifter estimates (Table 6.2, see caption for details of the along-current direction). The correlation between the drifters and MDT_G is high (r=0.92), and both the mean and the standard deviation of the differences is less than for the individual estimates.

In summary there is good agreement between the estimates, although small differences are noted. This agreement is not surprising because the current is tightly constrained by bathymetry in this area. The agreement between the geodetic estimate and the drifters is particularly striking. An interesting observation from the MDT_G estimate is that there are mean currents on the continental shelf which vary in direction along the shelf. Around

---

Figure 6.8 *(following page)*: Estimates of the mean surface geostrophic flow for part of the Florida Current (29-34°N, 81.5-76.5°W, labelled SAB on Figure 6.7). Top left, middle left and top right: Velocity vectors derived from the spatial gradients of MDT_G and MDT_{Argo} and from surface drifter observations respectively. Vector size and colour are related to speed. The straight black line shows the position of the section plotted in the bottom panel. The thin black lines are the 100 m isobath, indicating the location of the shelf break, and the 400 m isobath, which shows the Charleston Bump. Bottom: Mean surface current speed normal to the section plotted on the previous panels derived from the gradients of MDT_G (blue) and MDT_{Argo} (red) and from the surface drifters (black). The grey shaded area is the error for the drifter estimate, calculated as two times the standard error of the sample mean. The bathymetry and distance from shore is plotted beneath.

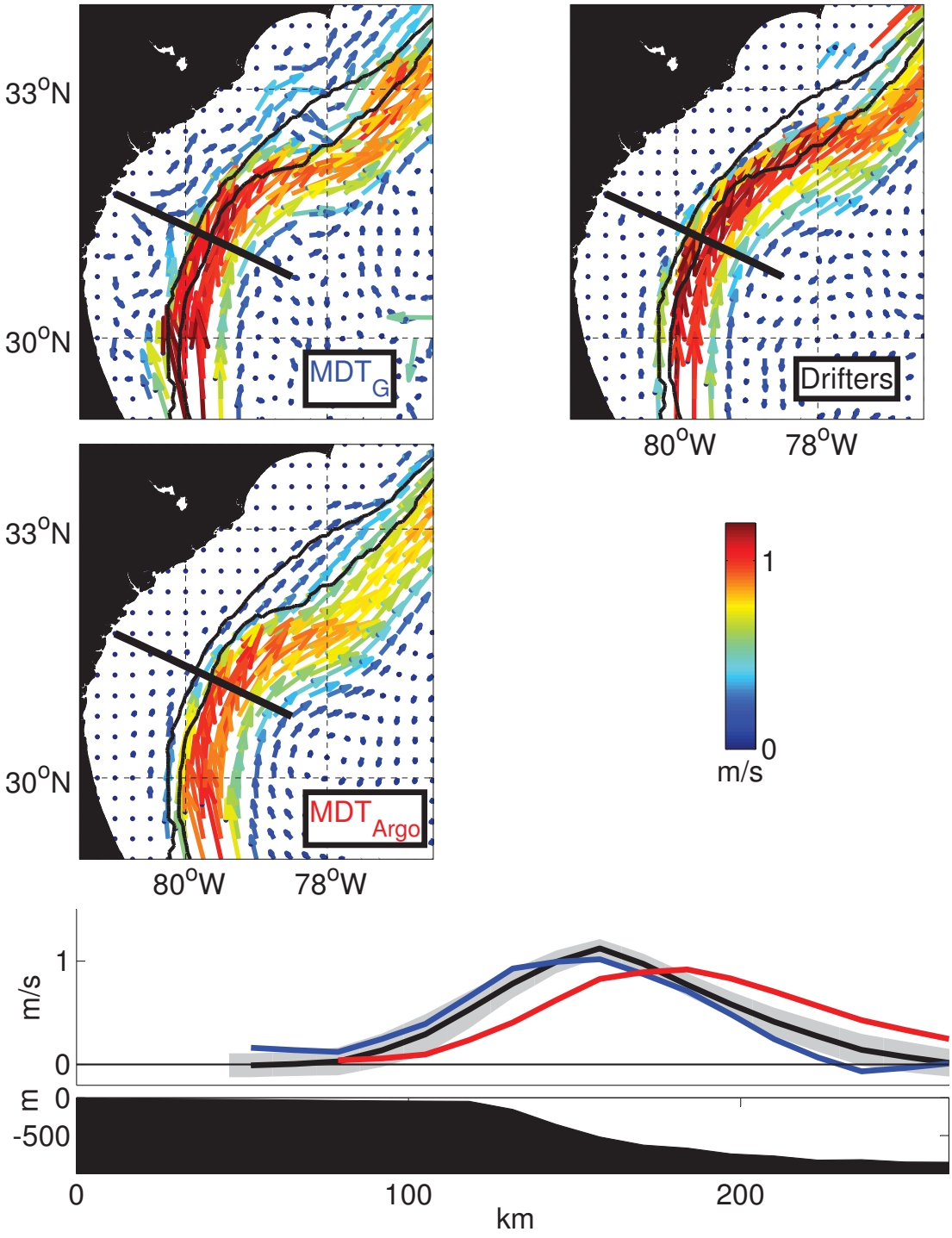
33°N
30°N
MDT G
Drifters
80°W
78°W
33°N
30°N
MDT Argo
80°W
78°W
1
0
m/s
m/s
1
0
m
0
-500
0
100
200
km

Table 6.1: Comparisons of the sea surface topography MDT_G with MDT_{Argo} and MDT_{WOA} for each of the subdomains described in Section 6.3. The first five columns show the standard deviation (cm) of all gridpoints within each subdomain for MDT_{Argo}, MDT_{WOA} and MDT_G and their differences. The final two columns are the correlations of MDT_{Argo} and MDT_{WOA} with MDT_G. The subdomains are shown in Figure 6.7.

	MDT_{Argo}	MDT_{WOA}	MDT_G	MDT_{Argo} -MDT_G	MDT_{WOA} -MDT_G	$\text{r}_{Argo,G}$	$\text{r}_{WOA,G}$
SAB	32.6	32.7	30.5	8.6	9.7	0.96	0.95
GSS	38.6	36.5	42.8	10.2	11.7	0.97	0.97
SGB	29.7	30.3	33.8	8.6	8.3	0.97	0.97

Table 6.2: Statistics of fit for the along-current component of the speeds estimated from drifters and from MDT_G for each of the subdomains described in Section 6.3. The first three columns show the mean and standard deviation (cms^{-1}) of along-current speed at all gridpoints within each subdomain for drifters, and MDT_G and for their differences. Standard deviations are shown in parentheses. The final column is the correlation of along-current speed between drifters and MDT_G. The subdomains are shown in Figure 6.7. Along-current is defined as a bearing of 300° for SAB, 330° for GSS, and 0° for SGB (i.e. zonal flow).

	Drifters	MDT_G	Drifters-MDT_G	$\text{r}_{D,G}$
SAB	26.8 (35.3)	28.1 (33.9)	-0.2 (13.8)	0.92
GSS	20.3 (36.5)	15.9 (33.5)	2.6 (11.5)	0.95
SGB	7.6 (13.3)	5.2 (12.5)	2.2 (7.5)	0.83

30°N there appears to be a weak southward flow close to shore. In comparison the drifters and MDT_{Argo} show little or no flow on the shelf. This may be due to errors in the geodetic estimate close to shore, but this subject will be discussed in more detail in the next chapter.

6.3.2 The Gulf Stream Separation

The Gulf Stream moves away from the continental shelf near Cape Hatteras at 35°N as a free jet. The point of departure shifts north and south both seasonally and interannually (*Frankignoul et al.* [2001]) but the excursions are small (20-30 km). Downstream meanders and rings form so there is considerable variability in the position of the jet, but this mostly occurs downstream of the New England seamounts around 69°W (*Talley et al.* [2011]). *Halkin and Rossby* [1985] measured the current off Cape Hatteras at 73°W between 1980 and 1983. Averaged along their transect they found maximum surface current speeds in excess of 100 cms^{-1}, and a current width (measuring the region where current speeds exceed 20 cms^{-1}) of approximately 160 km. They noted that the position of the Gulf Stream moved during the observation period, and recalculating the speeds in a stream coordinate system which tracks the centre of the jet, they estimated maximum mean speeds in excess of 150 cms^{-1} and a width of about 140 km.

The geodetic estimate (MDT_G, Figure 6.9, top left panel) shows the Gulf Stream departing the coast at Cape Hatteras with maximum mean speeds of around 100 cms^{-1}. The current width is between 150 km and 200 km, and this is in good agreement with the measurements of *Halkin and Rossby* [1985]. The zero skewness contour, produced from satellite altimeter sea surface height anomalies for the period 2000–2007, is plotted. This contour can be used to identify the mean path of unstable ocean jets (*Thompson and Demirov* [2006]). There is good agreement between the zero skewness contour and the fastest part of the current.

The drifter estimate (Figure 6.9, top right panel) shows the Gulf Stream following a similar path to the MDT_G estimate with comparable speeds. The oceanographic estimates (MDT_{Argo} and MDT_{WOA}, Figure 6.9, middle panels) both show a Gulf Stream that is slower than the other estimates. MDT_{WOA} has a maximum speed of about 75 cms^{-1} as the current passes Cape Hatteras, quickly decreasing to less than 50 cms^{-1}. MDT_{Argo} does

better, with speeds around 85 cms^{-1} and 70 cms^{-1} respectively. The main path of the Gulf Stream in both plots is further south than the other estimates and than the zero skewness contour. The MDT$_{WOA}$ estimate also shows a partial overshoot of the separation point, with a flow continuing into the Middle Atlantic Bight.

Statistics of comparison for MDT$_G$, MDT$_{Argo}$ and MDT$_{WOA}$ are provided in Table 6.1. These show a high correlation between both oceanographic estimates and the geodetic estimate (r=0.97). The standard deviation of the differences is much lower than the standard deviation of the individual fields. Similar statistics of comparison between MDT$_G$ and the drifters (Table 6.2) show the mean along-current speed estimate from drifters to be slightly higher than the MDT$_G$ estimate (20.3 cms^{-1} for drifters and 15.9 cms^{-1} for MDT$_G$) but there is a high correlation between the estimates (r=0.95).

A further difference between the estimates relates to the recirculations to the north and south of the Gulf Stream. These are visible in the MDT$_G$ and drifter plots. The oceanographic estimates, MDT$_{Argo}$ and MDT$_{WOA01}$, have the southern recirculation but no sign of the northern one. These recirculations can be seen in the section plot as negative speeds across the section either side of the main current.

6.3.3 The Southern Grand Banks

As the free jet flows eastward meanders develop. These meanders become larger past the New England seamounts, and rings are formed to both the north and the south. *Auer* [1987] analyzed weekly satellite sea surface temperature observations to estimate the position of the Gulf Stream landward surface edge (GSLSE) over a period of 5 years. He plotted the

---

Figure 6.9 *(following page)*: As for Figure 6.8 but for the Gulf Stream separation region (33.5-40°N, 76-69°W, labelled GSS on Figure 6.7). Additionally the velocity vectors derived from the spatial gradients of MDT$_{WOA}$ are plotted (middle right). The bottom panel includes the mean surface current speed normal to the section derived from the gradients of MDT$_{WOA}$ (green). The zero skewness contour is shown by the dashed line on the top four panels, calculated from altimeter sea surface height anomalies for the period 2000–2007. The thin black line shows the approximate position of the 700 m isobath, indicating the shelfbreak. The bathymetry depths for the section (bottom panel) are plotted on a log scale.

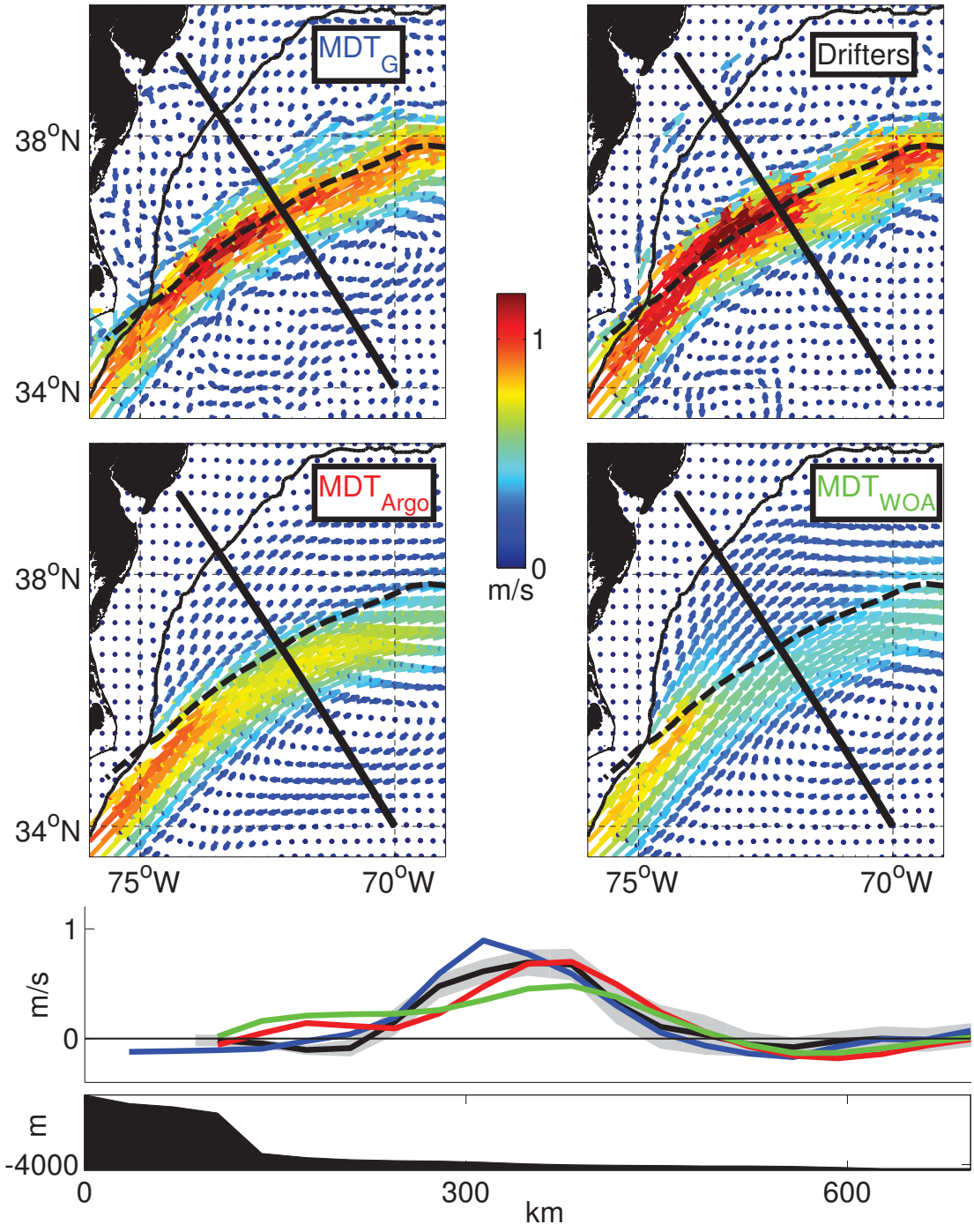
MDT G
Drifters
MDT Argo
MDT WOA
38°N
34°N
75°W
70°W
1
0
m/s
m/s
m
-4000
0
300
600
km

mean position of the GSLSE with a one standard deviation envelope and extreme positions to the north and south of the mean (his Figure 3). The mean path continues eastwards to approximately 48°W, where it turns to the northwest. The one standard deviation envelope, and the extreme envelope, widens noticeably downstream of 70°W. Between 60°W and 50°W the range is approximately $\pm 1^\circ$ latitude (one standard deviation) and $\pm 2\frac{1}{2}^\circ$ latitude (extreme values), equivalent to approximately 100 km and 250 km either side of the mean path respectively.

Rossby [1996] described the bifurcation of the Gulf Stream after it passes 50°W. As the Gulf Stream flows along the Southeast Newfoundland Rise it splits, with part turning to the north and mixing with cold Labrador Current water to form the North Atlantic Current, and part feeding a somewhat diffuse recirculation around the subtropical gyre including the Azores Current. Unlike the section of the Gulf Stream before the bifurcation, the meanders in this region are essentially permanent features. *Krauss et al.* [1990] estimated that the Gulf Stream splits approximately two-thirds to the North Atlantic Current and one-third to the Azores Current and other recirculations. They noted the importance of the Mann Eddy (*Mann* [1967]), a permanent anticyclonic eddy located near 41°N 44°W, in feeding waters from the North Atlantic Current branch back to the Azores Current branch.

Clarke et al. [1980] described surveys of the region to the south and east of the Grand Banks. They measured surface speeds of approximately 90 cms^{-1} before the bifurcation and 50 cms^{-1} in the North Atlantic Current at 42°N. *Krauss et al.* [1990] produced corresponding estimates of 118 cms^{-1} and 70 cms^{-1} respectively.

The MDT_G estimate of the circulation (Figure 6.10, top left panel) shows the Gulf Stream flowing eastwards at approximately 40°N as far as 46°W, following the zero skewness contour. The main current has a width of about 2° of latitude, although the eastward flow extends over a much broader width. This is likely because of the meandering of the jet, and the total width of about 400 km that can be seen on Section A (Figure 6.10, bottom left panel) is comparable with the current envelope identified by *Auer* [1987]. Gulf Stream speeds are variable in this estimate, but peak at about 50 cms^{-1}.

The drifter estimate shows a similar spatial pattern but with speeds exceeding 60 cms^{-1} in a few places. The oceanographic estimates, MDT$_{Argo}$ and MDT$_{WOA}$ (middle panels), show a northward meander to the Gulf Stream around 52°W which is not apparent in either the geodetic estimate or the drifters. Speeds are between 40 and 50 cms^{-1} for MDT$_{Argo}$ and lower for MDT$_{WOA}$, especially toward the east. The plot of speeds across Section A shows the northward displacement of the Gulf Stream compared to the other estimates.

The northward flowing branch of the Gulf Stream, the origin of the North Atlantic Current, is clearly seen in all of the estimates. The flow in each estimate is broken, with faster sections as the current meanders, but generally follows the zero skewness contour. For example the flow around the northwestern side of the Mann Eddy is particularly fast, with MDT$_G$ and the drifters showing speeds around 50 cms^{-1}. These estimates are comparable with the measurements by *Clarke et al.* [1980] and *Krauss et al.* [1990]. The oceanographic estimates are slower in places but follow a similar pathway. Flow around the east and south of the Mann Eddy can be seen in the MDT$_G$ and drifter estimates, but is not apparent in the oceanographic estimates.

Further north, the Labrador Current can be seen in all of the estimates, following the shelf break. The flow splits near Flemish Cap (47°N 45°W), with part of the current flowing through Flemish Pass and part around Flemish Cap. The northward flow of the North Atlantic Current passes close to the southward flow of the Labrador Current around

---

Figure 6.10 *(following page)*: Estimates of the mean total surface geostrophic speed for the southern Grand Banks region (36-50°N, 62-36°W, labelled SGB on Figure 6.7). Top left, middle left, middle right and top right: Velocity vectors derived from the spatial gradients of MDT$_G$, MDT$_{Argo}$ and MDT$_{WOA}$ and from surface drifter observations respectively. The straight black lines shows the position of the two sections plotted in the bottom panels and the thin black lines are the 700 m isobath (representative of the shelf break). The zero skewness contour is shown by the dashed line, calculated from altimeter sea surface height anomalies for the period 2000–2007. Bottom left and bottom right: Mean surface current speed normal to the sections plotted on the previous panels derived from the gradients of MDT$_G$ (blue), MDT$_{Argo}$ (red) and MDT$_{WOA}$ (green) and from the surface drifters (black). The grey shaded area is the error for the drifter estimate, calculated as two times the standard error of the sample mean. The bathymetry and distance from shore is plotted beneath, with the depth plotted on a log scale.

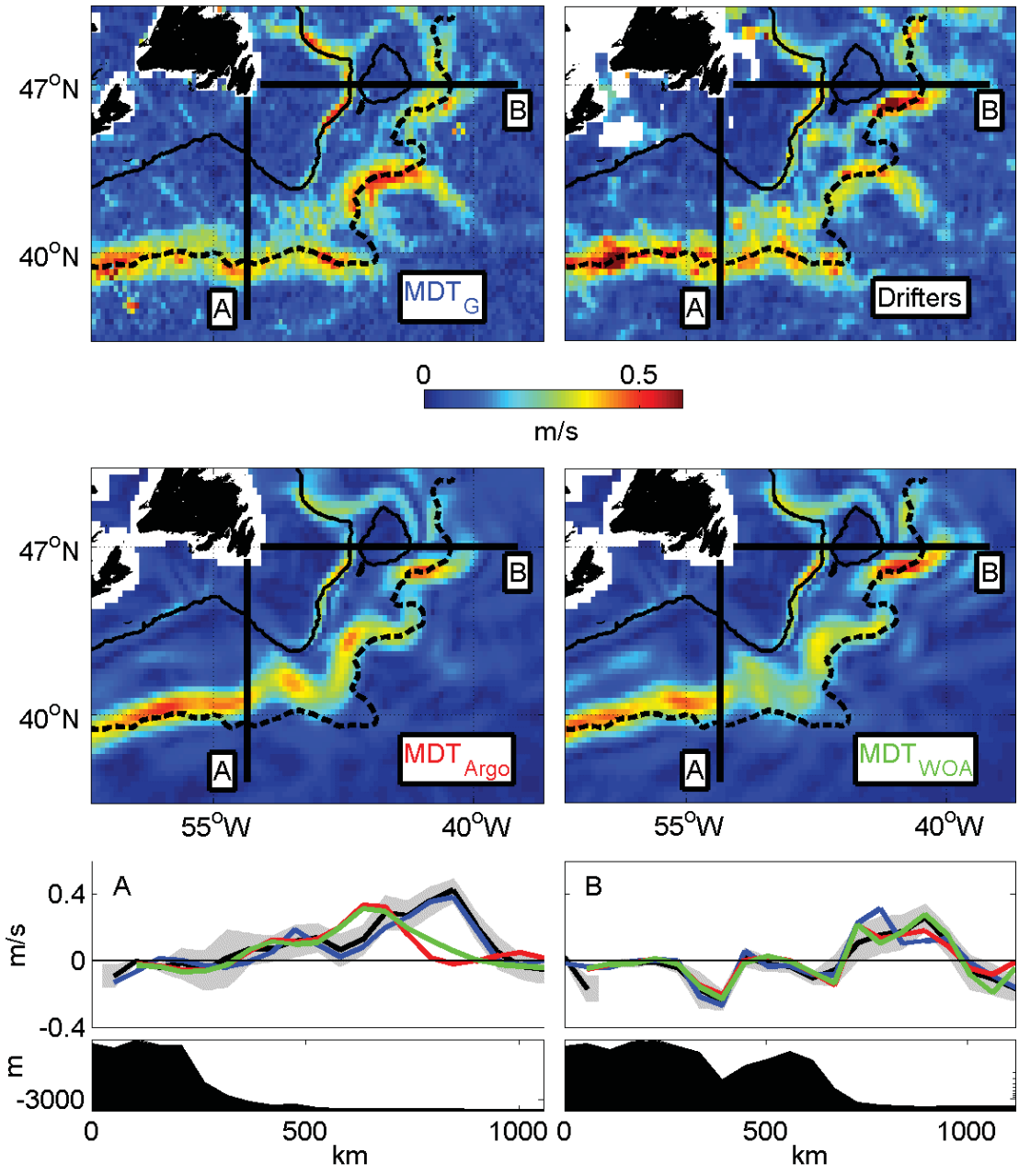
47°N
40°N
B
A
MDT G
Drifters
0
0.5
m/s
MDT Argo
MDT WOA
55°W
40°W
A
B
0.4
0
-0.4
m/s
m
-3000
0
500
1000
km

Flemish Cap, and this is clearly visible in Section B (Figure 6.10, bottom right panel) at approximately 700 km offshore. The speed estimates and pathways are in good agreement for the bathymetrically-constrained Labrador Current, but there are some differences in speed and position for the North Atlantic Current.

The statistics of comparison for the MDT estimates (Table 6.1) show good agreement between both oceanographic estimates and the geodetic estimate (r=0.97 in each case). The comparison of the geodetic and drifter estimates of zonal speed (Table 6.2) also shows good agreement (r=0.83) and the mean and standard deviation of the differences is much lower than for either of the individual estimates.

6.3.4 The Azores Current

The Azores Current forms part of the North Atlantic subtropical gyre, transporting water eastward from the Gulf Stream to recirculate southwards and eventually westwards back to the source regions of the Gulf Stream. *Klein and Siedler* [1989] showed the Azores Current to flow eastwards between 32°N and 35°N. Although the current has its origins in the Gulf Stream at the Newfoundland Rise, the pathway is seasonally varying and, at times, quite diffuse.

Figure 6.11 shows speed estimates from MDT_G (top panel), MDT_{Argo} (middle panel) and the drifters (bottom panel) for the region of the Azores Current, with the colour scale chosen to ensure that the relatively slow Azores Current is visible. All three plots suggest a current flowing zonally at around 35°N between 50°W and 20°W, as expected. Current speeds are around 10-20 cms^{-1} in all of the estimates, although the MDT_G and drifter estimates are noisy. There is no clear flow from the Gulf Stream bifurcation region in any of the estimates, but this is not surprising given the variability of the pathway described by *Klein and Siedler* [1989]. All three plots also show a weaker zonal flow to the north of the Azores. This corresponds with the description by *Talley et al.* [2011] of another branch from the Gulf Stream flowing eastward at 42°N and weakening as it passes to the north of the Azores.

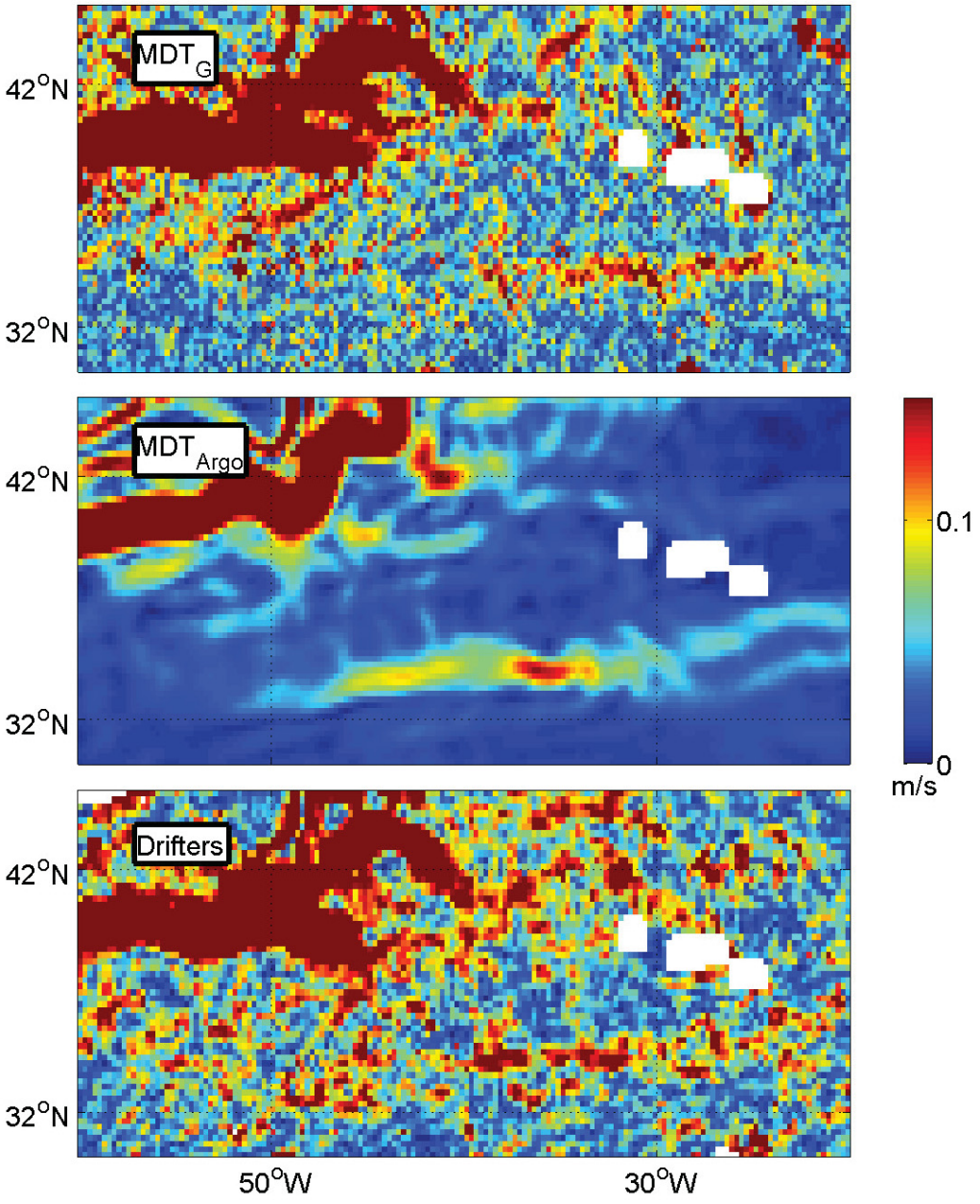

Figure 6.11: Estimates of the mean surface current speed for the Azores Current from MDT_G (top panel), MDT_{Argo} (middle panel) and the drifters (bottom panel). The colour scale is chosen to ensure that the relatively slow speeds of the Azores Current can be seen. The Gulf Stream and the southern Grand Banks are located at the top left corner of each plot. The Azores are located around 40°N 30°W, where the speed estimates are masked.

6.4 Discussion

In this chapter new geodetic and oceanographic estimates of the MDT and the mean surface circulation of the subtropical gyre of the northwest Atlantic are presented. The estimates are evaluated and compared with surface drifter estimates and other independent observations.

The geodetic estimate incorporates data from the GOCE satellite gravity mission. Earlier geoid models relied on terrestrial gravity measurements to provide the short wavelength detail but GOCE contributes the detail for features down to lengthscales of 170 km (subsequent releases of GOCE will reduce this lengthscale further). This should improve the accuracy of the geodetic estimate in regions where terrestrial gravity measurements are sparse. A comparison with drifter estimates and the oceanographic estimates suggests that the geodetic estimate provides a good estimate of the Gulf Stream system circulation. All of the main oceanographic features of the circulation are present, and current speeds are close to expected values. Spurious features that were seen in an earlier geodetic estimate (Figure 6.2, top panel), such as those around the Bahamas, are no longer present. The Gulf Stream's separation at Cape Hatteras and its subsequent pathway around the Grand Banks are in good agreement with other estimates.

The oceanographic estimate is produced using a new Argo-period climatology which reduces the aliasing that is a problem in multi-decadal climatologies. A comparison of this estimate with one produced using the WOA climatology shows some improvements in the Gulf Stream separation and current speeds downstream of the separation. However some errors remain in the path of the current near the Grand Banks, and this may be because of the model configuration rather than the climatology.

Reproducing the Gulf Stream separation has been a long time problem with ocean circulation models (e.g. *Chassignet and Marshall* [2008]). Whilst high resolution models ($\frac{1}{10}^\circ$ and better) are often able to reproduce the separation, lower resolution models frequently fail to do so unless they incorporate data assimilation. The geodetic estimate, MDT_G, is a useful tool for validating such ocean model estimates. The oceanographic estimates, MDT_{Argo} and MDT_{WOA}, demonstrate that ocean models that are spectrally

nudged to a TS climatology can reproduce the separation and the downstream path of the Gulf Stream fairly well. However the results are dependent on the climatology, with MDT_{Argo} producing slightly more realistic results.

In conclusion the geodetic estimate produces a realistic estimate of the MDT and the mean surface circulation. Generally known oceanographic features are well reproduced, including relatively small features such as the deflection of the Gulf Stream by the Charleston Bump. The geodetic estimate performs considerably better than the oceanographic ones, although the oceanographic estimate produced using the Argo-period climatology is a little better than one produced using the WOA climatology. In the South Atlantic Bight the proximity of the current to the coastline limits the utility of this technique, and in the next chapter an alternative approach for studying the coastal zone is investigated.

CHAPTER 7

UNDERSTANDING SEA LEVEL VARIABILITY ALONG THE COAST OF THE SOUTH ATLANTIC BIGHT

In the previous chapter a geodetic estimate of MDT and the mean surface circulation was compared with oceanographic estimates, surface drifter estimates and in situ measurements from the ocean. The geodetic estimate produces a realistic mean surface circulation with a good representation of the Gulf Stream system.

The first section of the Gulf Stream, the Florida Current, passes very close to the U.S. coastline in the Straits of Florida. The geodetic estimate of MDT becomes less accurate within approximately 25 km of the coastline because of errors in the altimeter-derived mean sea surface. For this reason the geodetic estimate was masked to avoid spurious circulation features close to shore and this masking conceals part of the Florida Current.

As the Florida Current flows northward into the South Atlantic Bight the shelf widens and the main current moves away from the masked region. The geodetic circulation estimate shows current features on the shelf, varying in the alongshore direction, but these features are not apparent in the oceanographic or surface drifter estimates. If this alongshore variability of the MDT on the shelf is real, it is not clear whether the variability is linked to the main Florida Current flow, or whether the shelf is insulated from the open ocean and the MDT is simply responding to local forcing acting over the shallower shelf regions.

Although the altimeter-derived MDT is unreliable in the coastal zone, an alternative source of sea surface height information is available from coastal tide gauges. In this chapter tide gauge data are referenced to a geoid model to construct an estimate of the alongshore tilt of the MDT. In order to understand the mean tilt, statistical relationships between the temporal variability of the tilt and processes in the open ocean are explored. Finally an ocean circulation model is used to investigate the sensitivity of the tilt to some of these processes and thereby understand the physical causes of the coastal sea level variability.

An important practical objective of this chapter is to establish whether the coastal tide gauges can be used as an indicator of what is happening in the ocean beyond the shelf i.e., to assess the value of the tide gauges as a useful component of an ocean monitoring system.

7.1 Background

The physical oceanography of the South Atlantic Bight and some earlier investigations into the alongshore tilt of sea level are described in the following sections.

7.1.1 The Circulation of the South Atlantic Bight

The South Atlantic Bight (SAB) extends from Cape Canaveral, Florida in the south to Cape Hatteras, North Carolina, in the north. The Gulf Stream, often referred to as the Florida Current in this region, is the dominant feature of the circulation. It has its origins in the Loop Current in the Gulf of Mexico, exiting through the Straits of Florida to the North Atlantic (e.g. *Talley et al.* [2011]). The flow is constrained by the narrow channel, which is only 80 km across near Miami. The peak mean surface current speed was measured at 180 cms^{-1} by *Leaman et al.* [1987], only 20 km from the Florida coastline.

Through the SAB the current follows the shelf break, which moves further offshore between Miami and the middle SAB. *Cadden et al.* [2009] estimated the surface geostrophic speed of the Gulf Stream between 31°N and 32°N from 1992 to 2004 using satellite altimeter sea surface height anomalies calibrated using in situ measurements. They found

speeds varying between 1.5 and 2.5 ms^{-1}, with the main flow just offshore of the 200 m isobath.

The continental shelf increases from approximately 50 km wide near Cape Canaveral to about 130 km wide near Savannah, Georgia. The shelf is relatively shallow, with typical depths less than 60 m. *Atkinson et al.* [1983] described the climatology of the SAB shelf. Generally they found that the hydrographic properties of the shelf waters point to a strong influence of the Gulf Stream on the outer shelf and river runoff and atmospheric forcing on the inner shelf. Winds are typically from the south or southwest during the summer (and upwelling favourable), from the northeast in the fall, and from the northwest during the winter. They found the mean flow in the upper water column at the shelf break to be northward, with speeds of 65 cms^{-1} during winter and spring, and 54 cms^{-1} during summer and fall. On the shelf they suggested that the surface currents are related to the local wind forcing, with surface currents toward the north during the winter and spring (17 cms^{-1} at the 45 m isobath and 4 cms^{-1} at the 30 m isobath). In the summer and fall they found currents toward the south at the 45 m isobath (5 cms^{-1}) and toward the north at the 30 m isobath (1 cms^{-1}).

Lee and Brooks [1979] analyzed data from two current meters deployed on the Georgia shelf during a single winter. One mooring was near the shelfbreak, in a water depth of 100 m, and the other was in 50 m water on the middle shelf. They found that current variability was a response to both local wind forcing and Gulf Stream variability, with the influence of the Gulf Stream decreasing with distance from the shelfbreak.

Castelao [2011] investigated the intrusion of Gulf Stream waters onto the SAB shelf. These intrusions are related to either Gulf Stream meanders and eddies or Ekman transport due to northerly winds. He found that they occur either at the surface or at depth, depending on the stratification of the shelf waters. They were observed more frequently in the north and the south, where the shelf is narrower, and only infrequently were they observed to extend to the coast.

7.1.2 The Alongshore Tilt of Sea Level

There is a long history of attempts to relate the alongshore tilt of sea level to the Gulf Stream. These studies are described below.

Montgomery [1938] examined the low frequency variability of sea level at Miami and Charleston and suggested that dynamic and steric effects dominate, with an additional local wind contribution at Charleston. He estimated the mean speed of the Florida Current using the difference in sea level between the east and west coasts of Florida and Torricelli's theorem, a particular case of Bernoulli's principle, which balances the loss of potential energy with the gain of kinetic energy, to give

$$v = \sqrt{2gh} \tag{7.1}$$

where h is the head and g is the acceleration due to gravity. Using a sea level difference of 19 cm, measured by levelling across Florida, he estimated the mean current speed at 193 cms^{-1}. He considered this a realistic estimate but later revisited the calculation (*Montgomery* [1941]), to take into account the fact that the upstream flow was not stationary. The mean sea level difference between Key West and Miami, measured by tide gauges and geodetic levelling, was 4.9 cm whereas his calculations suggested the head should be 7.0 cm. The monthly variability was greater than the expected current speed variability and he concluded that it was not possible to use the alongshore sea level tilt as an indication of the strength of the Gulf Stream.

Wunsch et al. [1969] also examined tide gauge records at Key West and Miami. They confirmed the results of *Montgomery* [1941] and went on to establish an absence of spectral coherence between the records. They speculated that this may be related to the narrowing of the channel between the two stations, and this may be the reason why Montgomery's calculation failed.

Sturges [1974] examined the large scale tilt of sea level along the east coast of North America. From steric height calculations he estimated a tilt of 2.5 $\pm$ 0.5 cm/deg on the inside edge of the Gulf Stream system between 12°N and 36°N. He also examined the

across-stream momentum balance, which he took to be a simple geostrophic balance between the Coriolis force and the across-stream pressure gradient

$$fv = g\frac{\partial \eta}{\partial x} \tag{7.2}$$

where v is the downstream current speed, η is the sea level and x is the across-stream coordinate. He integrated (7.2) across the stream and then differentiated with respect to y, the along-stream coordinate, to give

$$\frac{\partial \Delta h}{\partial y} = \frac{f}{g}\frac{\partial \overline{v} X}{\partial y} + \frac{\overline{v} X}{g}\frac{\partial f}{\partial y} \tag{7.3}$$

where Δh is the across-stream change in sea level, $\overline{v}$ is the mean surface along-stream speed and X is the current width. This is the along-stream change in the cross-stream geostrophic balance. He neglected the first term on the right, arguing there is little along-stream change in the surface transport of the Gulf Stream, and found a meridional change in Δh of 2.8 cm/degree. Subtracting the contribution from the offshore edge of the Gulf Stream he concluded with an estimate of 2.0 $\pm$ 0.4 cm/deg for the sea level tilt on the inshore edge of the current, in good agreement with his steric height estimate.

Sturges [1974] noted that, at the time that he was writing, geodetic levelling pointed to an alongshore tilt in the opposite direction to his estimates. The error associated with geodetic levelling has limited the ability to absolutely compare sea level between tide gauges, and most studies have considered only the variability. For example *Blaha* [1984] studied the seasonal cycle of Gulf Stream intensity by identifying coherent variability at tide gauge stations along the east coast of the U.S.

7.1.3 The Alongshore Tilt of Coastal Sea Level

Montgomery [1938] and *Sturges* [1974] simplified the alongshore tilt problem by adopting approaches that do not specifically consider the balance of forces at the coast. For example they ignored the contribution of wind and lateral and bottom friction. This subsection will focus on the sea level tilt at the coast. This introduces some simplifications (e.g. there is no flow normal to the coast and the steric effect goes to zero), but it also introduces some complexities.

The momentum equation in vector form, following for example *Batchelor* [1967] (Equation 5.1.1), can be written as

$$\frac{\partial \mathbf{v}}{\partial t} + \frac{1}{2}\nabla(|\mathbf{v}|^2) - (\zeta + f)\hat{k} \times \mathbf{v} = \frac{-1}{\rho_0}\nabla p + g + \mathcal{F} \tag{7.4}$$

where ζ is relative vorticity, $\hat{k}$ is the unit vector in the vertical, g is the acceleration due to gravity (assumed aligned with the z coordinate direction) and $\mathcal{F}$ represents the frictional terms.

By separating the pressure term into a surface component and a depth integrated density related component

$$p = \rho_0 g\eta + \int_z^0 \rho g dz \tag{7.5}$$

where η is the surface displacement, the momentum equation can be rewritten as

$$\frac{\partial \mathbf{v}}{\partial t} + \frac{1}{2}\nabla(|\mathbf{v}|^2) - (\zeta + f)\hat{k} \times \mathbf{v} = -g\nabla\eta - g\nabla \int_z^0 \rho g dz + g + \mathcal{F} \tag{7.6}$$

Within this framework it is now clear that *Montgomery* [1938] assumed a balance between the second and fourth terms, the gradient of kinetic energy and the surface pressure gradient. This reduces to Torricelli's theorem (7.1). *Sturges* [1974] considered the across-stream geostrophic relation, a balance of the third and fourth terms, the Coriolis force and the across-stream pressure gradient. He integrated this balance across the stream, and then differentiated in the alongstream direction to give (7.3).

Each of these earlier studies considered the alongshore balance but did not consider the forces specifically at the coast. In this subsection a more complete balance of forces at the coast is considered. A number of terms equal zero because a steady state is assumed, there is no flow normal to the coast, and the depth integrated pressure term tends to zero. Aligning the y-axis with the coast, so the v component of flow is downstream, the momentum equation in the alongshore direction at the coast (where the water depth tends to a small value) becomes

$$\frac{\partial \eta}{\partial y} = \frac{\mathcal{F}}{g} - \frac{1}{2g}\frac{\partial}{\partial y}|v|^2 \tag{7.7}$$

representing a balance between the alongshore pressure gradient, a friction term (including the effect of lateral and bottom friction and wind stress) and a kinetic energy term.

The observed tilt and its variability will be considered within this framework later in this chapter.

7.2 Estimates of the Alongshore Tilt

With improved geoid models it is now feasible to compare absolute sea levels between tide gauges and hence measure the alongshore tilt of sea level. The tide gauge results can be validated by comparing the tilts with those obtained from an ocean model (in this case an ocean reanalysis product which assimilates observations), and with the geodetic MDT.

7.2.1 Tilts from Tide Gauges

Tidal records date back to the 18th Century in a few locations, and records spanning the past century are fairly widespread in Europe and North America, although less so elsewhere. The method of measurement varies, with a range of technologies including tide staffs, float gauges, and newer pressure, acoustic and radar gauges.

For this study seven tide gauge records are used, detailed in Table 7.1. Their locations are shown in Figure 7.1, left panel. Monthly mean sea level data were obtained from the Permanent Service for Mean Sea Level (PSMSL, www.psmsl.org). The seven stations were selected because they have complete data for at least 90% of the study period, they have no data gaps for periods longer than 4 months, and because ellipsoidal heights are available for the tide gauge benchmarks, allowing the sea level data to be referenced to the geoid model. Initially data were obtained for the period 1993 to 2009, corresponding to the period of the Glorys2v1 ocean reanalysis (see below), but this was subsequently revised to the period January 1995 to December 2009 because of large data gaps during 1993 and 1994. Short data gaps are filled by linear interpolation (see Table 7.1).

The tide gauge sea level records are corrected for the inverse barometer effect using NCEP/NCAR atmospheric reanalysis sea level pressure data (*Kalnay et al.* [1996]). The NCEP Reanalysis data were obtained from NOAA/OAR/ESRL PSD, Boulder, Colorado, USA (http://www.esrl.noaa.gov/psd/). The horizontal resolution of this reanalysis is coarse (approximately 210 km). Finer-resolution reanalysis products are available (e.g. the North

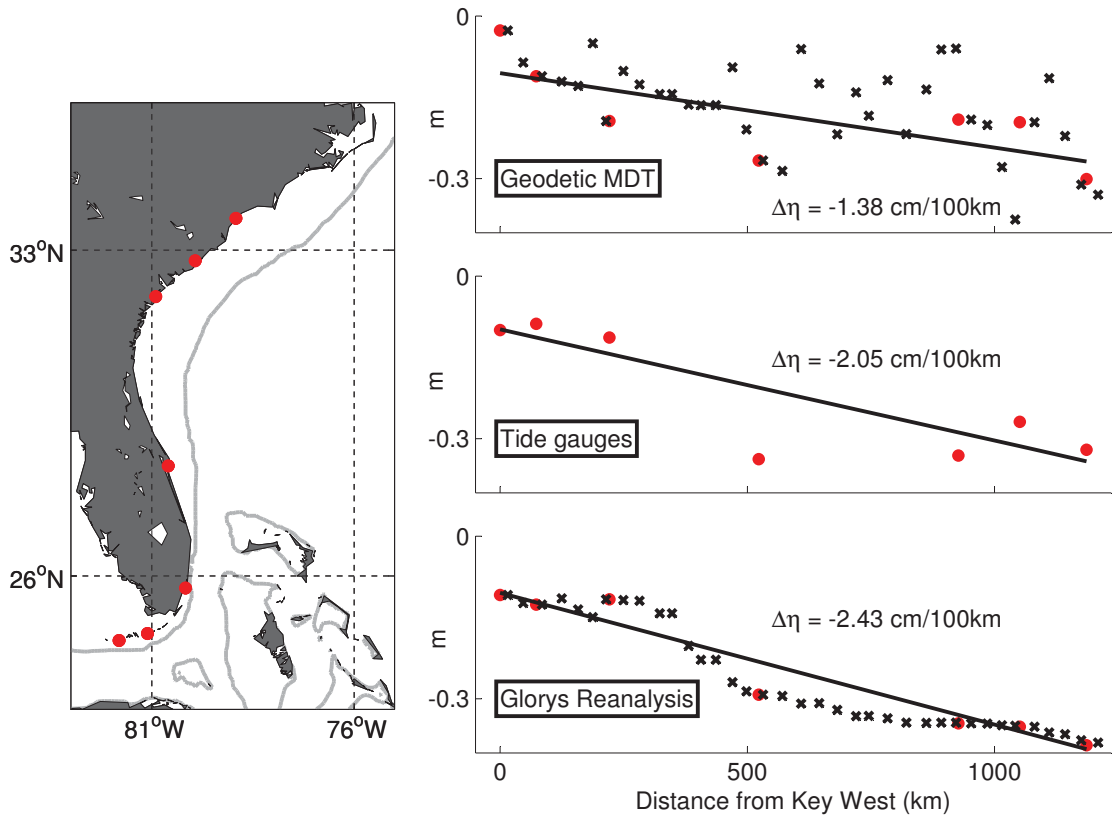

Figure 7.1: Estimates of the mean alongshore tilt of sea level in the South Atlantic Bight. (Left panel) The location of the tide gauge records used in this study. The grey line shows the position of the 200 m isobath, indicating the shelf break. (Right panels) Estimates of MDT at the tide gauge locations (red circles) and intermediate points (black crosses) plotted against alongshore distance from the first tide gauge, at Key West, Florida. The estimates are calculated using the altimeter mean sea surface referenced to the CGG2010 geoid (top panel), the tide gauges referenced to the CGG2010 geoid (middle panel) and from the Glorys2v1 ocean reanalysis product (bottom panel). The black line shows the linear regression using only the sea level estimates at the tide gauge locations. The slope of the regression ($\Delta\eta$) is marked.

Table 7.1: Details of the tide gauge records used to calculate the alongshore tilt of mean sea level. The final column shows data completeness, expressed as the percentage of months with mean sea level data out of the 180 months from January 1995 to December 2009.

Station Name	Latitude (°N)	Longitude (°W)	Data (%)
Key West	24.55	81.81	97.8
Vaca Key	24.71	81.11	95.0
Virginia Key (Miami)	25.73	80.16	99.4
Trident Pier (Cape Canaveral)	28.42	80.59	98.3
Savannah	32.03	80.90	98.9
Charleston	32.78	-79.92	100
Springmaid Pier (Myrtle Beach)	33.65	78.92	94.4

American Regional Reanalysis, *Mesinger et al.* [2006]) but for adjustment of monthly mean values the NCEP reanalysis is sufficiently detailed.

The corrected tide gauge data are converted to ellipsoidal heights using information on the tide gauge benchmarks obtained from the Center for Operational Oceanographic Products and Services of the National Oceanic and Atmospheric Administration (http://tidesandcurrents.noaa.gov/index.shtml). Data were transformed to the same reference ellipsoid and permanent tide system as the CGG2010 geoid model. The MDT is then calculated as the difference between the adjusted mean sea level and the CGG2010 geoid model (Figure 7.1, middle right panel).

7.2.2 Tilts from an Ocean Reanalysis

The Glorys2v1 ocean reanalysis is distributed by the MyOcean project (www.myocean.eu). The reanalysis is performed with the NEMO v3.1 global ocean model in a 0.25° configuration with 75 vertical levels. Atmospheric forcing is provided by the ERA-Interim atmospheric reanalysis. The model includes a sea ice model and data assimilation of along track satellite altimeter sea surface height anomalies, sea surface temperatures, and in situ profiles of temperature and salinity. The sea surface height anomalies are referenced to a

MDT product (the CNES-CLS09 MDT, *Rio et al.* [2011]) which incorporates geodetic information.

The reanalysis has been produced for the period from 1993 to 2009 but here the data from 1995 to 2009 are used to correspond with the time period of the tide gauge data described above. Monthly mean sea surface height values are extracted for the ocean gridpoints nearest to each of the seven tide gauge locations, and the temporal mean is calculated. Values are also extracted for intermediate alongshore points to give a more complete picture of the alongshore tilt (Figure 7.1, bottom right panel).

7.2.3 The Geodetic MDT

The geodetic topography, MDT_G, is described in Section 2.3. The geoid model that is used is the CGG2010 model, which was earlier shown to be more accurate in the South Atlantic Bight region than the PCG08I model.

Although MDT_G is included here for comparison, it is known that the geodetic MDT is not accurate in the coastal region because of errors in the satellite altimeter-derived mean sea surface (see Section 2.2). Elsewhere in this thesis MDT_G is masked in the coastal region, but for this section the MDT value at the ocean gridpoint nearest each tide gauge location is extracted from an unmasked version of the MDT (Figure 7.1, top right panel). Values are also extracted at intermediate points corresponding to those used to extract Glorys2v1 values.

7.3 Comparing the Estimates of Tilt

The mean alongshore tilt ($\overline{\Delta\eta}$) is calculated as the slope coefficient of the linear regression of the MDT onto the alongshore distance from the first station, at Key West (Figure 7.1, right panels).

All three estimates show a downward tilt from Key West to Springmaid Pier, although the magnitude of the tilt varies between estimates. The tide gauge ($\overline{\Delta\eta}_{tg}$) and Glorys reanalysis ($\overline{\Delta\eta}_{model}$) estimates are close to estimates by *Sturges* [1974], although these new estimates are at the coast and his estimates were at the inside edge of the current.

The geodetic MDT estimate ($\overline{\Delta\eta}_{altimeter}$) is lower but there is scatter in the data because of the known errors in MDT_G in the coastal region. The tide gauge data points and the corresponding values from the Glorys reanalysis show similar alongshore patterns, with a sharp drop in sea level between the third and fourth stations (Virginia Key, Miami and Trident Pier, Cape Canaveral). The intermediate data points from the Glorys reanalysis illustrate that the fall in sea level occurs over a distance of approximately 150 km south of Cape Canaveral. This corresponds with the region where the shelf develops.

The differences between the first three tide gauge stations (Key West, Vaca Key and Virginia Key, Miami) are small in both the tide gauge and Glorys reanalysis estimates, with almost no difference between Key West and Miami. These are the two stations where *Montgomery* [1941] found a sea level difference and tried to relate it to the current speed.

With good agreement in the mean, it is appropriate to look at the seasonal and temporal variability of $\Delta\eta_{tg}$ and $\Delta\eta_{model}$ to see whether there is consistent agreement between the estimates. The seasonal cycle of the tilt (Figure 7.2, top panel) shows good agreement with maxima in spring and fall, and minima in summer and winter. The monthly time series (Figure 7.2, bottom panel) again shows good agreement (correlation coefficient r=0.69).

The variability of both $\Delta\eta_{tg}$ and $\Delta\eta_{model}$ is plotted in the spectral domain in Figure 7.3. This shows that the variability has highest power at the higher frequencies in both estimates of the tilt, although the time series is not long enough to resolve decadal variability. The bottom panel shows that the two time series are coherent at all frequencies that are plotted.

7.4 Statistical Analysis of the Variability of the Alongshore Tilt

With good agreement between $\Delta\eta_{tg}$ and $\Delta\eta_{model}$, the Glorys2v1 reanalysis product can be used to identify statistical linkages between the variability of $\Delta\eta_{tg}$ and variability in the open ocean. Identifying the processes which contribute to the variability of $\Delta\eta_{tg}$ may help to identify the processes responsible for the mean tilt.

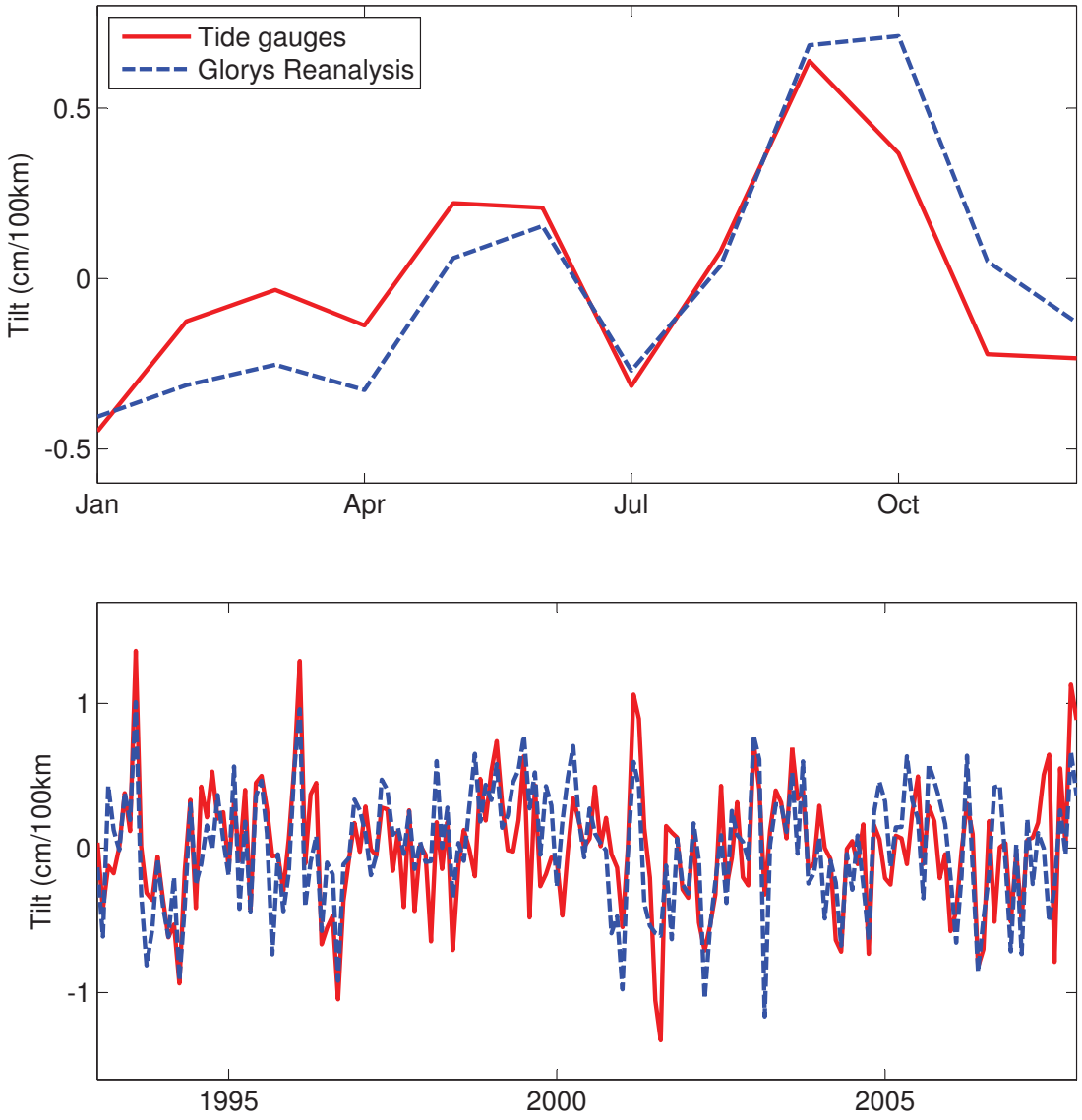

Figure 7.2: The temporal variability of the alongshore tilt of sea level. The seasonal (top) and monthly with seasonal cycle removed (bottom) variability of the tilt of sea level between Key West, Florida, and Springmaid Pier (Myrtle Beach), South Carolina, calculated from tide gauge heights referenced to the CGG2010 geoid (solid red line) and from the Glorys2v1 ocean reanalysis product (dashed blue line). In each case the tilt is calculated as the linear regression of sea level at the seven tide gauges shown in Figure 7.1 onto alongshore distance from Key West. The mean has been subtracted from each dataset.

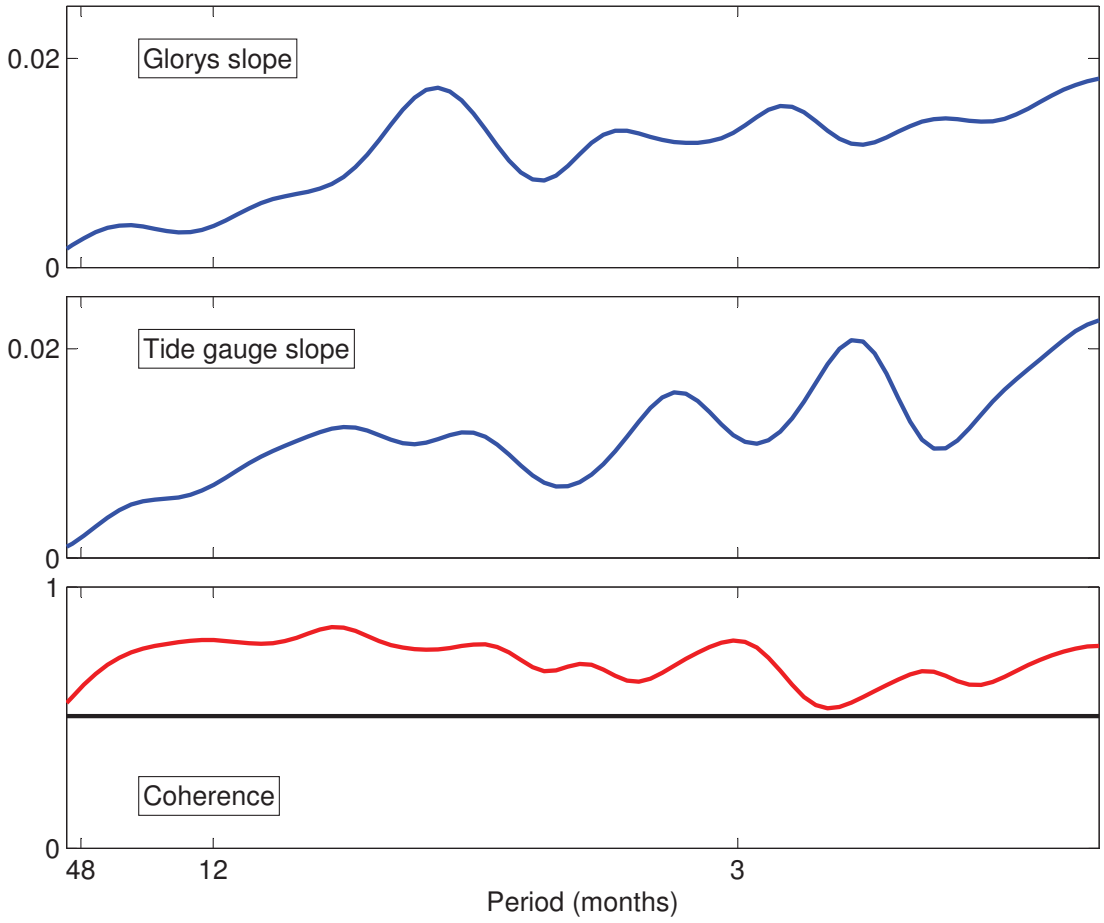

Figure 7.3: Spectral analysis of the temporal variability of the tilt of sea level. (Top panel) Power spectral density for the time series of monthly values of $\Delta\eta_{model}$ with the seasonal cycle removed. (Middle panel) The same power spectral density plot for the monthly values of $\Delta\eta_{tg}$, also with the seasonal cycle removed. (Bottom panel). The spectral coherence between $\Delta\eta_{model}$ and$\Delta\eta_{tg}$. The solid horizontal line indicates the 5% significance level.

7.4.1 Sea Level

A linear regression between the monthly sea surface height time series at each of the ocean model reanalysis grid points and the time series of $\Delta\eta_{tg}$ is shown in Figure 7.4. The seasonal cycle has been removed from each time series before calculating the regression. Slope regression coefficients that are significant at the 10% level are shown in the top panel, indicating the sign and magnitude of the relationship between sea level and $\Delta\eta_{tg}$. The squared correlation coefficient is also plotted for each gridpoint where a significant regression coefficient exists (Figure 7.4, bottom panel), indicating the strength of the relationship.

The correlation coefficient plot shows, not surprisingly, that the relationship is strongest along the SAB shelf and the correlation coefficient becomes larger closer to shore. The relationship is also strongest in the northern SAB shelf region, suggesting that the tilt is determined primarily by variability in the northern tide gauge stations with variability at the southern stations largely unrelated to changes in the tilt. It is therefore not surprising that the regression coefficient shows that sea level near the northern SAB coast falls when the tilt increases.

Away from the SAB shelf most of the correlations are very weak. The exception is the shelf of the southern Middle Atlantic Bight (MAB), which indicates that coastal sea level north of Cape Hatteras is correlated with coastal sea level to the south. This will be discussed later in this chapter.

7.4.2 Surface Currents

A similar linear regression is shown in Figure 7.5 for the Glorys2v1 reanalysis surface currents and $\Delta\eta_{tg}$. The meridional and zonal components of the surface currents are regressed separately onto $\Delta\eta_{tg}$. The results are combined in Figure 7.5 with the two sets of slope regression coefficients plotted as vectors (top panel). The squared correlation coefficients are weighted by their contribution to the total variance and then combined (bottom panel). The regression coefficient vectors show that the increased alongshore tilt is associated with an increase in northward flow along the shelf (onshore of the 200 m

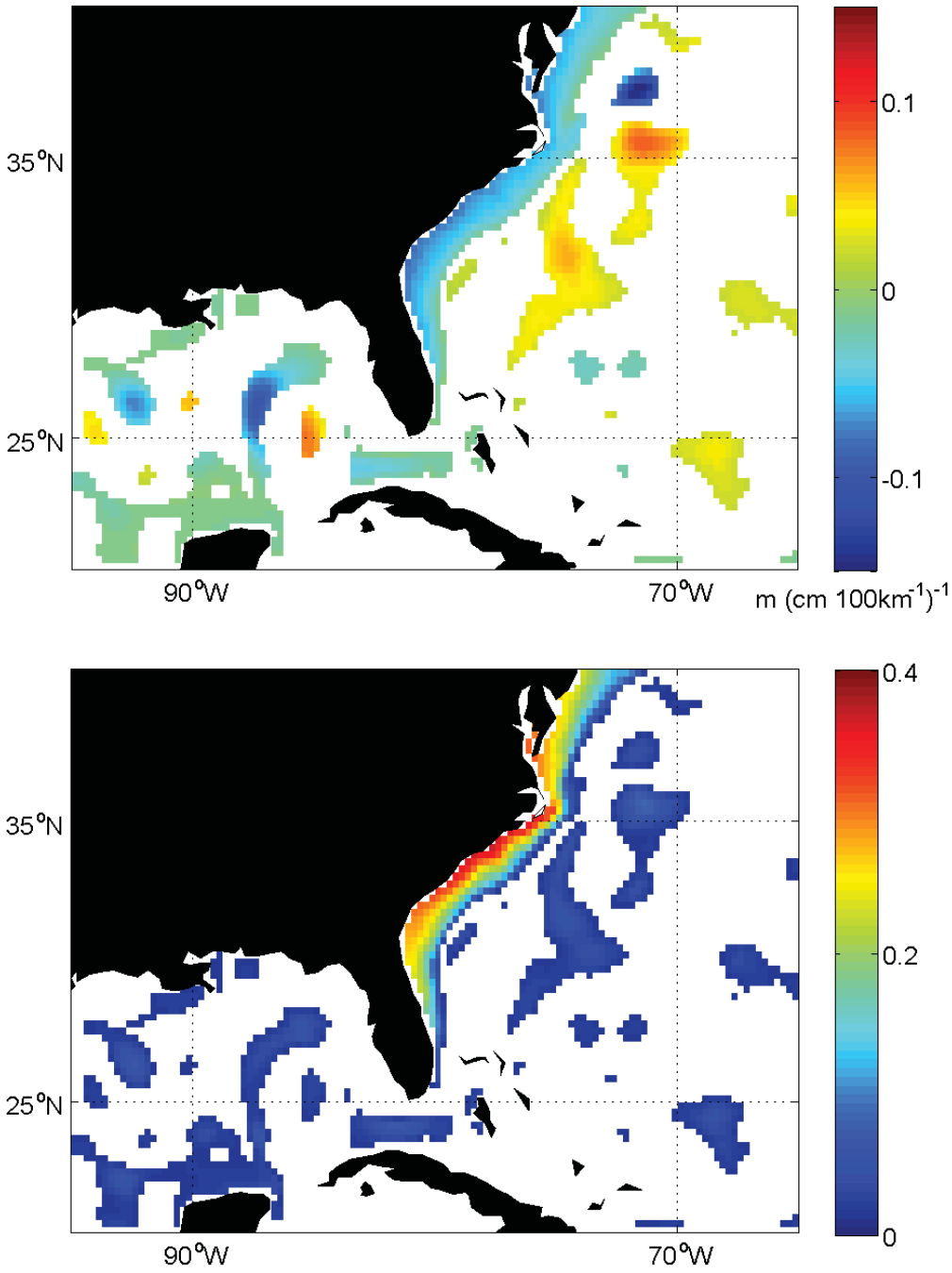

Figure 7.4: The statistical relationship between sea level tilt and sea surface height. (Top panel) The slope coefficients of linear regressions of the monthly mean sea surface height at each gridpoint of the Glorys2v1 ocean reanalysis onto the monthly mean sea level tilt measured by tide gauges. The seasonal cycle and the trend has been removed from each dataset. Only coefficients that are significant at the 10% level are shown. (Bottom panel) The squared correlation coefficient, r^2, between the tide gauge sea level tilt and the sea surface height time series at each gridpoint.

isobath) and a somewhat larger increase in the Gulf Stream (offshore of the 200 m isobath). Interestingly the relationship on the shelf extends all the way southwards to the beginning of the SAB shelf around 28°N. This suggests that variability of the flow onto the shelf may be a factor in the variability of $\Delta\eta_{tg}$. This is confirmed by a comparison of the mean monthly northward surface current speed on the shelf (<200 m depth) with $\Delta\eta_{tg}$ (correlation coefficient r^2=0.22), which indicates that the tilt becomes steeper as flow onto the shelf increases.

7.4.3 Density

A further regression, between density calculated from the Glorys2v1 temperature and salinity fields and $\Delta\eta_{tg}$, is shown in Figure 7.6. This shows the slope regression coefficients (top panel) and the correlation coefficients (bottom panel) for the density field along a section running offshore at 33.5°N. The correlation is low, but there is a hint of a relationship between dense waters on the shelf and an increase in $\Delta\eta_{tg}$.

7.4.4 Surface Wind and Wind Stress Curl

Having established statistically significant relationships between $\Delta\eta_{tg}$ and the Glorys2v1 reanalysis fields, the next step is to consider what might be driving the sea level and current variability. *Atkinson et al.* [1983] suggested that the currents of the middle and inner SAB shelf were related to local wind forcing, with the influence of the Gulf Stream increasing toward the shelf break. The variability of the Florida Current and Gulf Stream is believed to be strongly influenced by the wind force curl field (e.g. *DiNezio et al.* [2009]). Accordingly a similar statistical analysis is preformed using both the wind and the wind stress curl fields used to force the ocean model.

The results of the linear regression between surface winds and $\Delta\eta_{tg}$ is shown in Figure 7.7. The regression is performed separately for the zonal and meridional components of the wind field. The results are combined by plotting the vectors of the regression coefficients (top panel) and by combining the squared correlation coefficients weighted by their contribution to the total variance (bottom panel). The relationships are more widespread than the ocean relationships, which is expected because the wind field has a

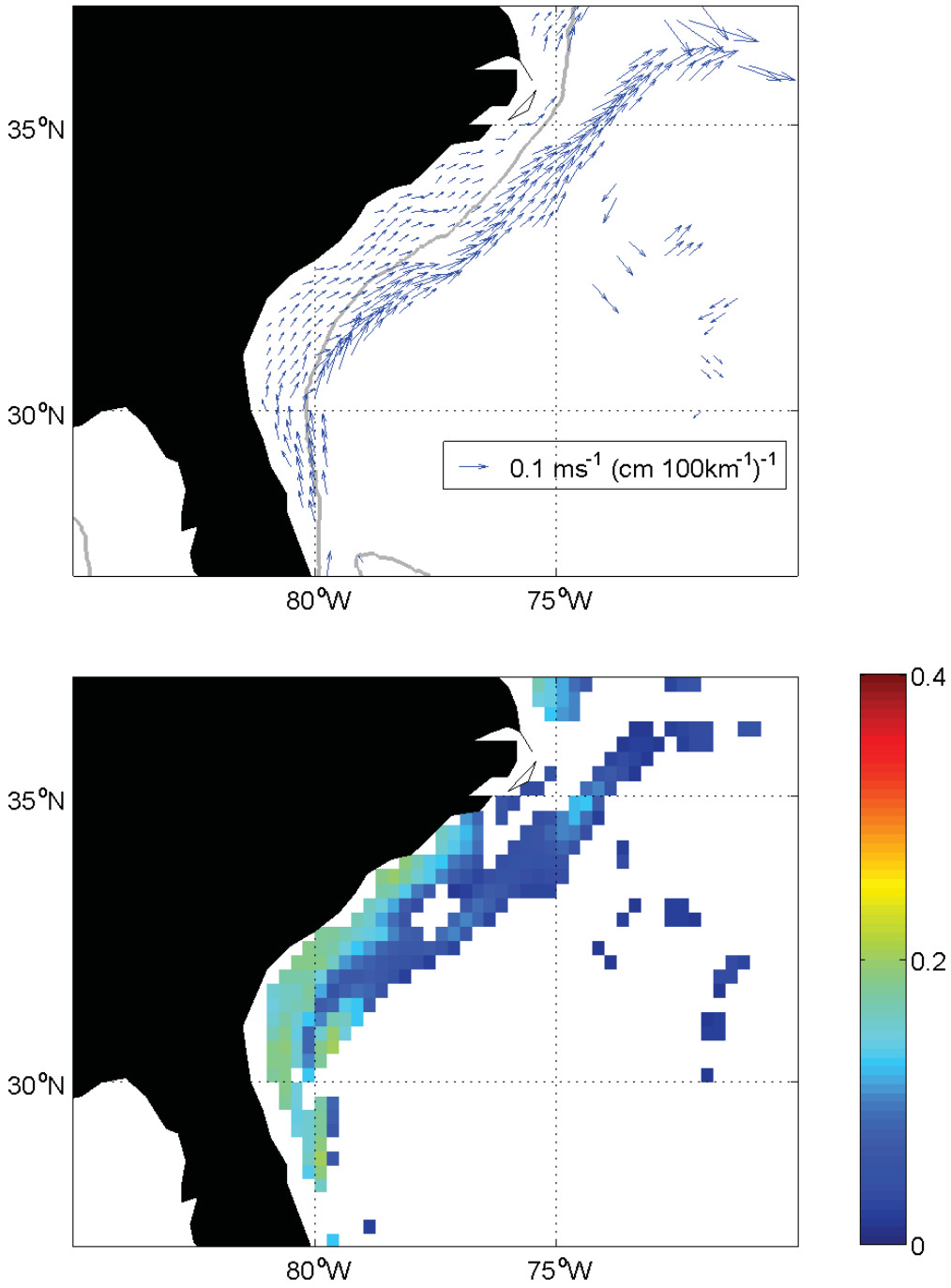

Figure 7.5: The statistical relationship between sea level tilt and surface currents. As for Figure 7.4 but for the regression of Glorys2v1 monthly mean surface currents onto the tide gauge monthly mean sea level tilt, shown for a reduced area covering the South Atlantic Bight. The regression is performed separately for the meridional and zonal currents, and the two regression coefficients plotted as a vector. The grey line on the upper panel shows the position of the 200 m isobath.

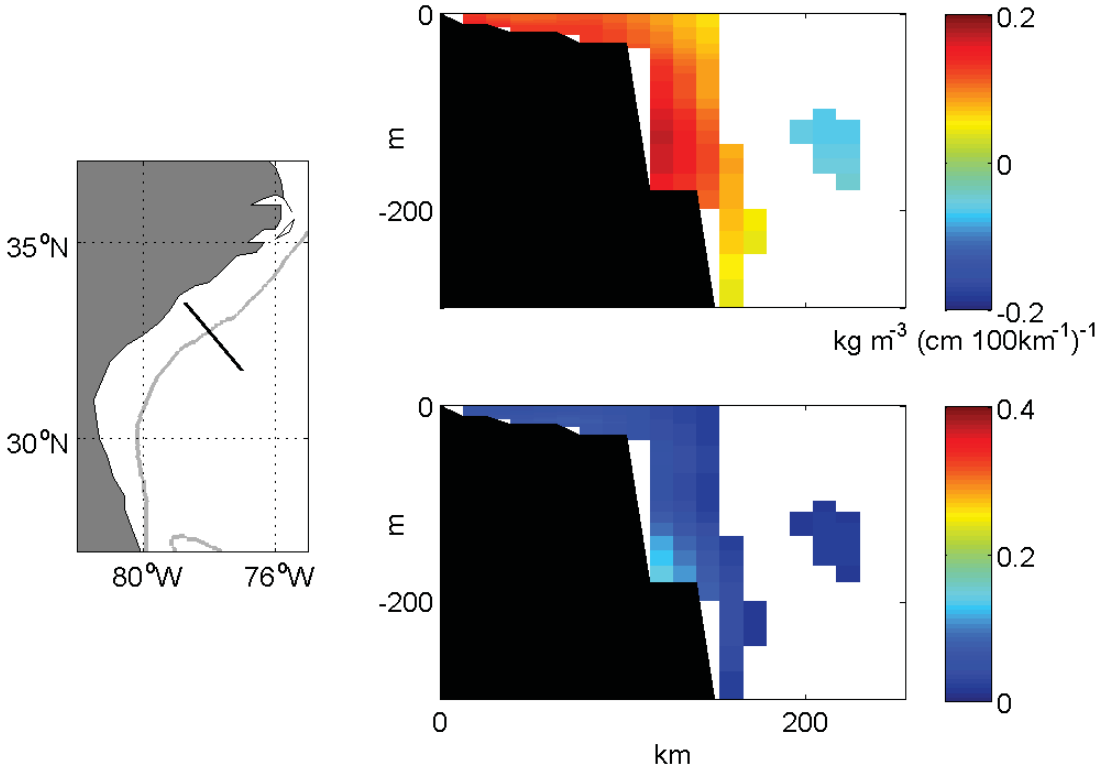

Figure 7.6: The statistical relationship between sea level tilt and density. As for Figure 7.4 but for the regression of density, calculated from Glorys2v1 monthly mean temperature and salinity fields, onto the tide gauge monthly mean sea level tilt for a section shown by the black line in the left panel. The grey line on the left panel shows the position of the 200 m isobath. The top right panel shows the significant slope regression coefficients and the bottom right panel shows the corresponding correlation coefficients.

larger spatial scale, so these plots are extended to cover the western North Atlantic. The wind data used for this regression are NCEP/NCAR reanalysis monthly mean surface winds (*Kalnay et al.* [1996]), obtained from NOAA/OAR/ESRL PSD, Boulder, Colorado, USA (http://www.esrl.noaa.gov/psd/). The correlation coefficients show the strongest relationship over the northern SAB, extending toward the northeast. The regression coefficient wind vectors are toward the northeast i.e. southwesterly wind anomalies over the northern SAB are statistically correlated with increases in the downward tilt from Key West to Springmaid Pier.

The final regression, between the wind stress curl and $\Delta\eta_{tg}$, is shown in Figure 7.8. Wind stress curl is calculated from the NCEP/NCAR reanalysis monthly mean surface wind stress fluxes, again obtained from NOAA/OAR/ESRL PSD in Boulder, Colorado. The correlation coefficient (bottom panel) is weak across most regions. There are a few patches of stronger correlations, mostly over the SAB. The slope regression coefficients (top panel) associated with these patches are negative, showing a statistical correlation between negative wind stress curl and an increase in the downward tilt of sea level toward the northern SAB.

7.4.5 Summary of Statistical Analysis

The statistical analysis is of limited value because, for example, the wind field may be correlated across a wide area beyond the region where the wind is playing a role in forcing the coastal tilt. However, there are two mechanisms that are consistent with the statistical relationships described in this section and which could explain the variability of $\Delta\eta_{tg}$. The observed variability of $\Delta\eta_{tg}$ could be caused by either one of these mechanisms, or some combination of both.

The first of these mechanisms is a shelf process brought about by surface wind stress. This could take the form of a barotropic response to the wind (i.e. wind setup), with southwesterly winds over the northern SAB lowering the sea level at the coast relative to southern Florida, thereby increasing $\Delta\eta_{tg}$. Alternatively the response could be baroclinic, with alongshore winds producing upwelling at the coast, which brings more dense water to

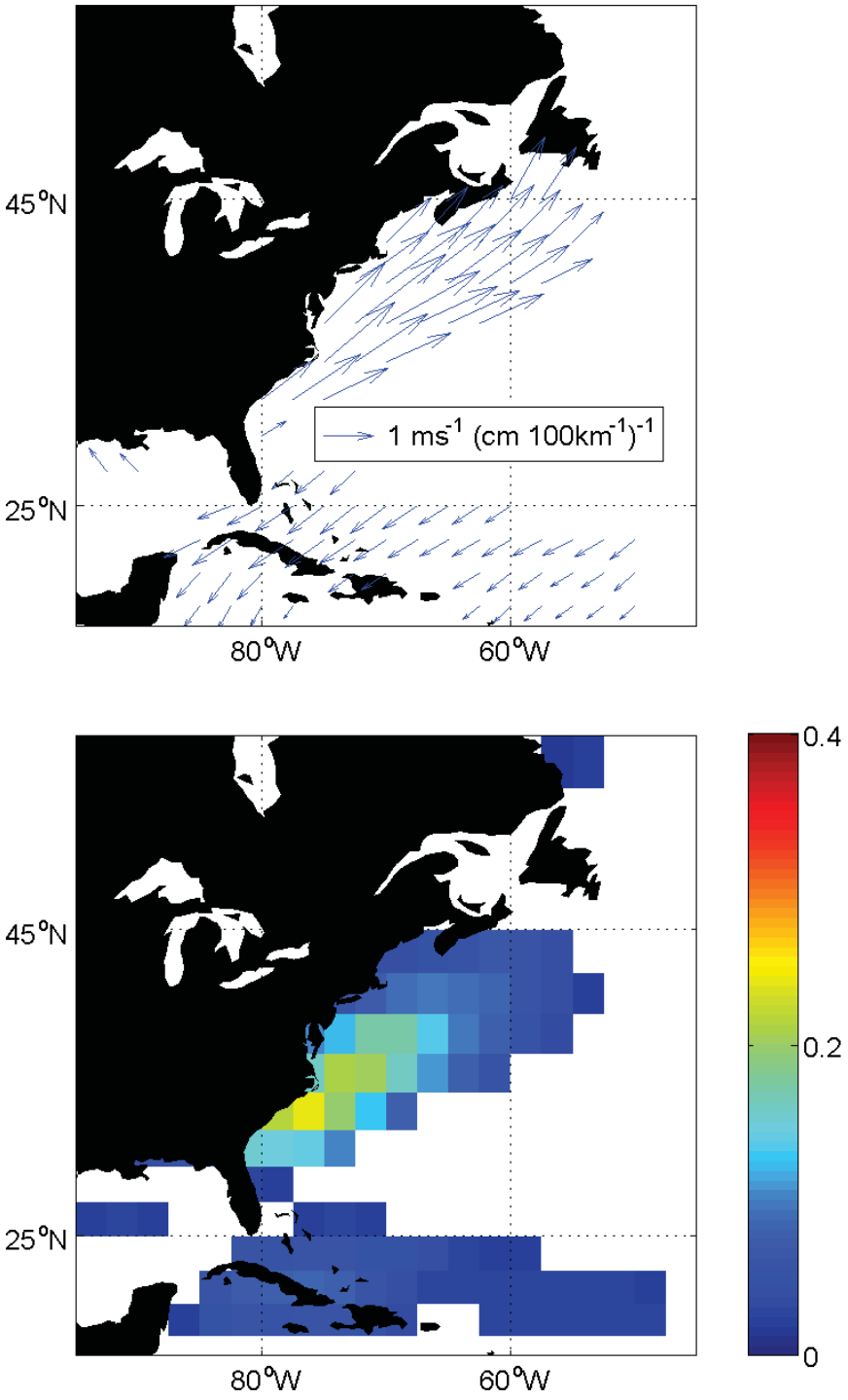

Figure 7.7: The statistical relationship between sea level tilt and surface wind. As for Figure 7.4 but for the regression of NCEP/NCAR atmospheric reanalysis monthly mean surface wind vectors onto the tide gauge monthly mean sea level tilt, shown for an enlarged domain covering the western North Atlantic. Regression vectors (top panel) are only plotted over the ocean.

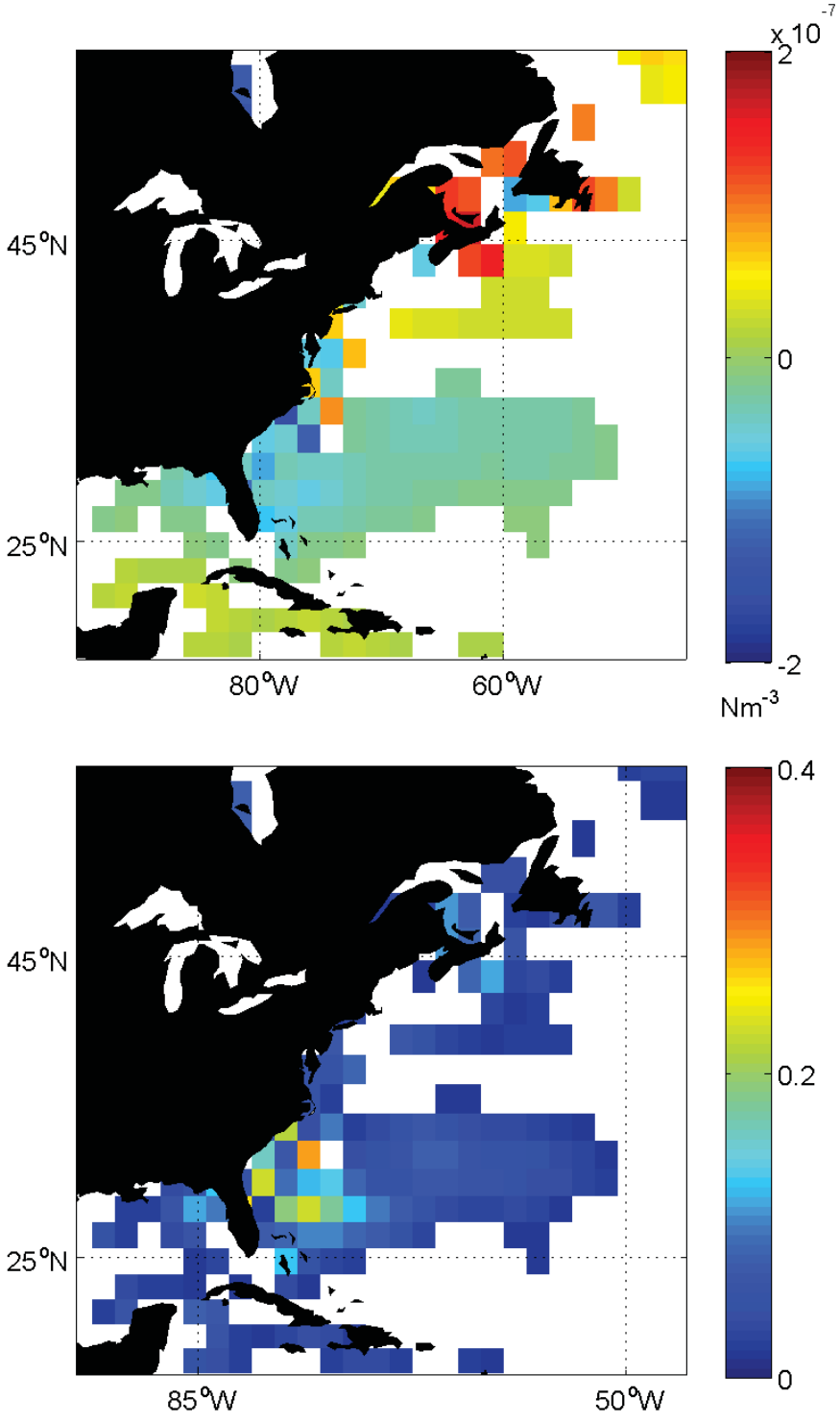

Figure 7.8: The statistical relationship between sea level tilt and wind stress curl. As for Figure 7.7 but for the regression of wind stress curl, calculated using NCEP/NCAR atmospheric reanalysis surface wind stress fluxes, onto the tide gauge sea level tilt.

the coast, lowers sea level and increases $\Delta\eta_{tg}$. Remote wind forcing could also influence $\Delta\eta_{tg}$, and this is discussed later in this chapter.

The second mechanism is a deep ocean process linked to variability in the speed and position of the Gulf Stream. Some of this variability may be related to changes in the wind stress curl field. The Gulf Stream is known to drive flow on the shelf and this flow may vary with the speed and position of the Gulf Stream. On the shelf there is an alongshore momentum balance between friction and the alongshore pressure gradient (7.7). As flow on the shelf increases, the corresponding increase in friction will be balanced by an increase in $\Delta\eta_{tg}$.

7.5 Diagnosing the Processes Contributing to the Mean Tilt

Having identified mechanisms that could account for the variability of $\Delta\eta_{tg}$, the contribution of the mechanisms to the mean tilt, $\overline{\Delta\eta}_{tg}$, is now tested by performing a set of ocean circulation model sensitivity studies.

7.5.1 The Ocean Circulation Model

The ocean model is the same model and configuration used to produce the oceanographic estimates of the MDT and the circulation, based on version 2.3 of NEMO (Nucleus for European Modelling of the Ocean) with ocean dynamics (OPA, *Madec et al.* [1998]) and sea-ice (LIM, *Fichefet and Maqueda* [1997]) components. OPA is configured here to use z-level coordinates and the model permits partial cells at the bottom. The modelled equations include the horizontal momentum equations, the hydrostatic equation, the continuity equation, tracer equations for temperature and salinity, and the thermodynamic equation of state, with parameterizations for small scale physics.

The model grid is a North Atlantic subset (5-68°N, 100°W-34°E) of a global tri-polar grid with nominal $\frac{1}{4}^\circ$ resolution. There are a maximum of 46 z-levels in the vertical, with level thickness of approximately 6 m at the surface increasing to 250 m at the bottom.

The model is forced by 10m wind, air temperature and specific humidity, and surface radiation and precipitation from the CORE normal-year data set (*Large and Yeager* [2009]).

Surface fluxes are calculated by the model using bulk formulae. Ocean temperature, salinity and transport are prescribed at the open boundaries from a global $\frac{1}{4}^\circ$ model.

The model incorporates spectral nudging (*Thompson et al.* [2006]) to suppress model bias and drift. The model is nudged toward a TS climatology in the climatologically important frequencies of 0 and 1 cycles per year but allowed to evolve prognostically in other frequency bands. This brings to the model state back toward the TS climatology at longer timescales, reducing drift, but does not suppress higher frequency features such as eddies.

7.5.2 The Sensitivity Experiments

Four runs are performed. In each case the model is run for 4 years from 2001 to 2004, using the same spin up from 1993 to 2000 as was used for producing the oceanographic estimates of the MDT. The details of the runs are as follows:

1. A control run. This uses the same TS climatology for spectral nudging as used during the spin up, the CORE atmospheric forcing is unperturbed and the boundary conditions are unchanged.

2. A remote wind perturbation run. This is the same as the control run except that the CORE 10 m wind fields are perturbed as shown in Figure 7.9 (top panel). This perturbation is chosen to approximate the pattern of the regression coefficients in the region of high correlation between wind and $\Delta\eta_{tg}$ shown in Figure 7.7. The extent of the perturbation is 34°N-45°, 80°W-65°W, restricted to areas where the ocean depth is less than 3000 m. The perturbation is 2 ms^{-1} zonally and 1 ms^{-1} meridionally, giving a total speed perturbation of approximately 2.2ms^{-1}. This is approximately the same magnitude as the annual mean wind in this region. The perturbation is smoothed at the boundary over a distance of 1 gridpoint to suppress spurious wind stress curl effects.

3. A density perturbation run. The wind stress curl is perturbed by altering the wind field, making it difficult to separate the effect of the wind stress curl from the wind perturbation. However a negative wind stress curl perturbation, corresponding to the regression shown in Figure 7.8, will lead to Ekman convergence and depress the isopycnals. To introduce this effect without perturbing the wind field a perturbation is applied to the TS climatology that is used for spectral nudging. The climatology perturbation comprises a circular region with a radius of 750 km centred at 28.5°N, 72.5°W (Figure 7.9, lower panel). The downward displacement of the TS fields is a maximum of 50 m at a depth of 530 m, decreasing linearly to zero at approximate depths of 100 m and 1300 m. The perturbation is also smoothed toward zero from a radius of 500 km to the maximum radius of 750 km.

4. A local wind perturbation run. The remote wind perturbation and density perturbation experiments perturb the model in regions identified by the statistical analysis and are designed to understand the variability of $\Delta\eta_{tg}$. To understand the effect of local wind on the mean tilt the wind is set to zero over the South Atlantic Bight (23°N-36°N, 84°W-74°W, Figure 7.12, top panel). The perturbation is smoothed at the boundary over a distance of 1 gridpoint to suppress spurious wind stress curl effects.

The 4 year mean sea level is output for each of the model runs.

7.5.3 The Remote Wind Perturbation Experiment Results

This experiment tests the hypothesis that wind forcing on the northern SAB shelf influences $\Delta\eta_{tg}$ variability and hence contributes to the observed mean tilt.

Figure 7.10 (top left panel) shows the difference between the mean sea level from the wind perturbation run and from the control run. The shelf response is largest over the southern MAB, where mean sea level is almost 10 cm lower in the wind perturbation run. At this point the wind perturbation is directed approximately offshore resulting in wind setdown. Along the SAB shelf a smaller reduction in sea level can be seen, with a maximum difference of approximately 5 cm in the north and decreasing toward the south.

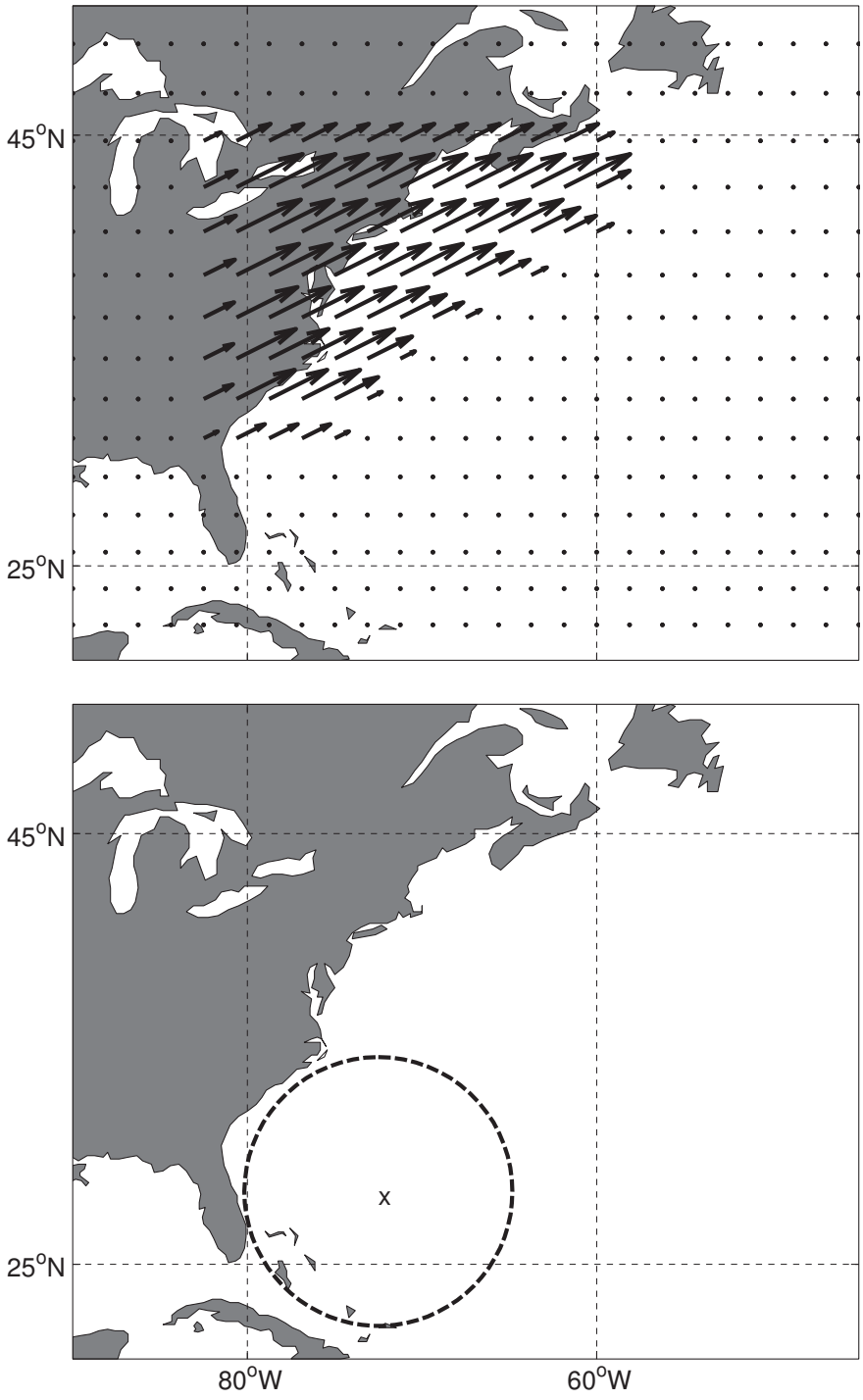

Figure 7.9: Forcing perturbations for the model sensitivity study. (Top) The wind field perturbation applied to the model forcing for the wind stress sensitivity test. (Bottom) The "X" marks the centre of the isopycnal displacement applied to simulate a wind stress curl effect. The dashed line shows the maximum spatial extent of the perturbation.

Offshore larger differences can be seen, related to shifts in the position of the Gulf Stream separation and eddies.

The mean surface geostrophic flow calculated from the gradients of the differences of mean sea level (Figure 7.10, top right panel) shows an alongshore flow anomaly in both the Gulf Stream (just offshore of the 200 m isobath) and on the shelf. There is increased flow onto the shelf at its southern edge. This result is encouraging because the pattern of flow anomalies is similar to the results of the regression between Glorys2v1 reanalysis surface currents and $\Delta\eta_{tg}$ (Figure 7.5, top panel).

The SAB shelf response, for both sea level and surface alongshore flow, extends to the south of the region where the wind perturbation is applied i.e., there is a remote effect. Wind-induced sea level and alongshore current signals can be propagated along a shelf by coastal trapped waves (e.g. *Gill and Schumann* [1974], *Brink* [1991]). These waves travel with the coastline on the right in the northern hemisphere (i.e. southwards for this coastline) and the amplitude decays with distance from the coast. The wavelength of wind-induced coastal waves is O(100s km), related to the length scale of the atmospheric system that generates the perturbations, and they travel the length of the SAB shelf in a matter of days. *Mysak and Hamon* [1969] and *Yuan* [2006] describe observations of such waves on the SAB shelf using tide gauge data.

The change in mean sea level at the SAB coast is illustrated in Figure 7.10 (bottom panel). This sea level anomaly tilts in the same direction as the mean tilt observed by tide gauges and from the Glorys2v1 reanalysis (Figure 7.1, middle right and bottom panels), but the slope is only one-tenth of the observed mean value.

7.5.4 The Density Perturbation Experiment Results

This experiment tests for the effect of deep ocean processes, introducing isopycnal displacements that are expected to be produced by a negative wind stress curl. This corresponds to the regression results shown in Figure 7.8.

The difference between the mean sea level from the density perturbation run and from the control run (Figure 7.11, top left panel) shows a large anomaly in the open ocean off

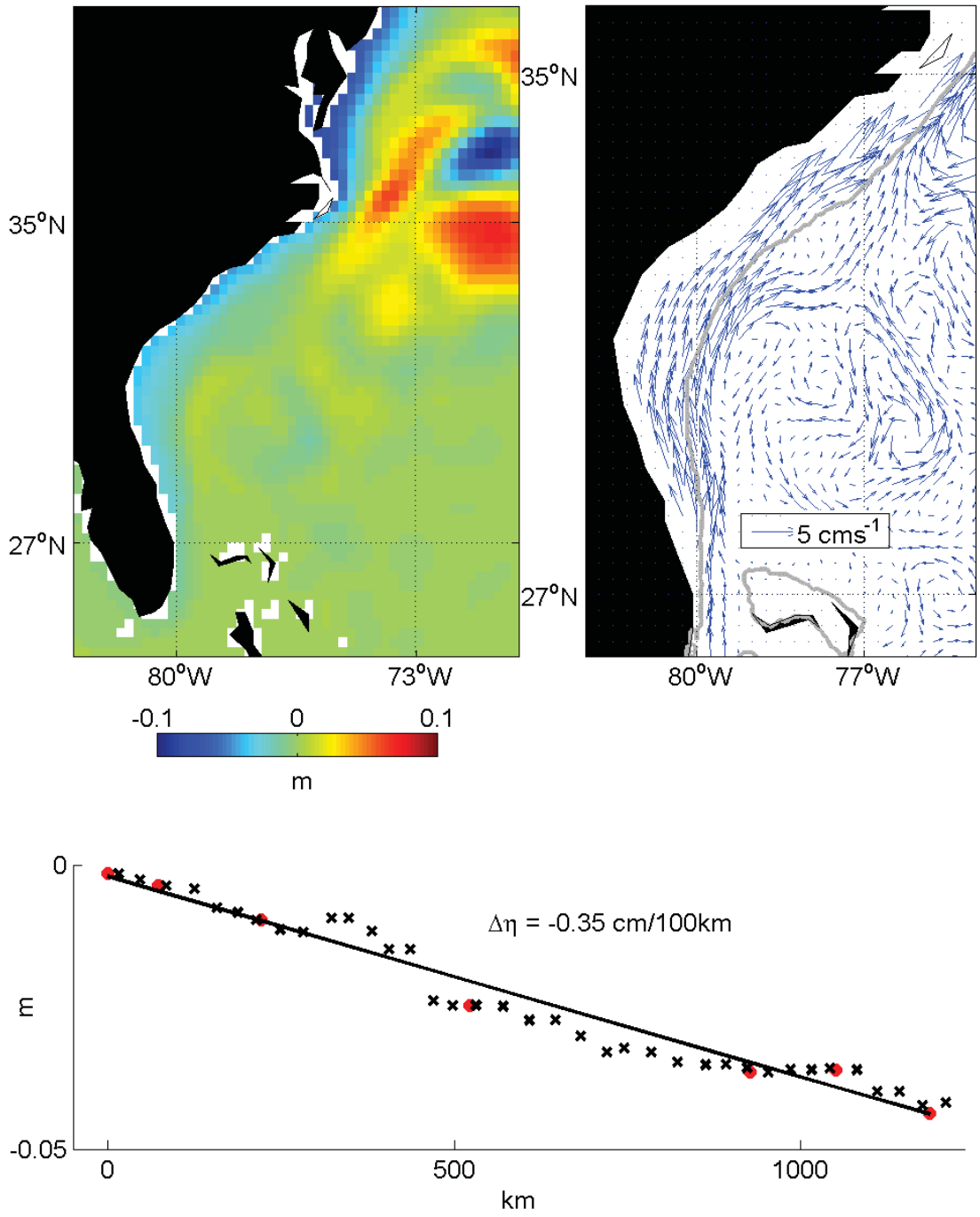

Figure 7.10: Sea level and current anomalies from the remote wind perturbation experiment. (Top left) The difference in mean sea level between the wind-perturbed run and the control run. (Top right) The mean surface geostrophic current calculated from the mean sea level difference, shown for a reduced domain. The grey line shows the position of the 200 m isobath, indicating the shelfbreak. (Bottom) The mean sea level from the top left panel at the tide gauge locations (filled red circles) and intermediate points (black crosses), plotted against alongshore distance from Key West. The black line shows the linear regression using only the tide gauge values. The slope of the regression ($\Delta\eta$) is marked.

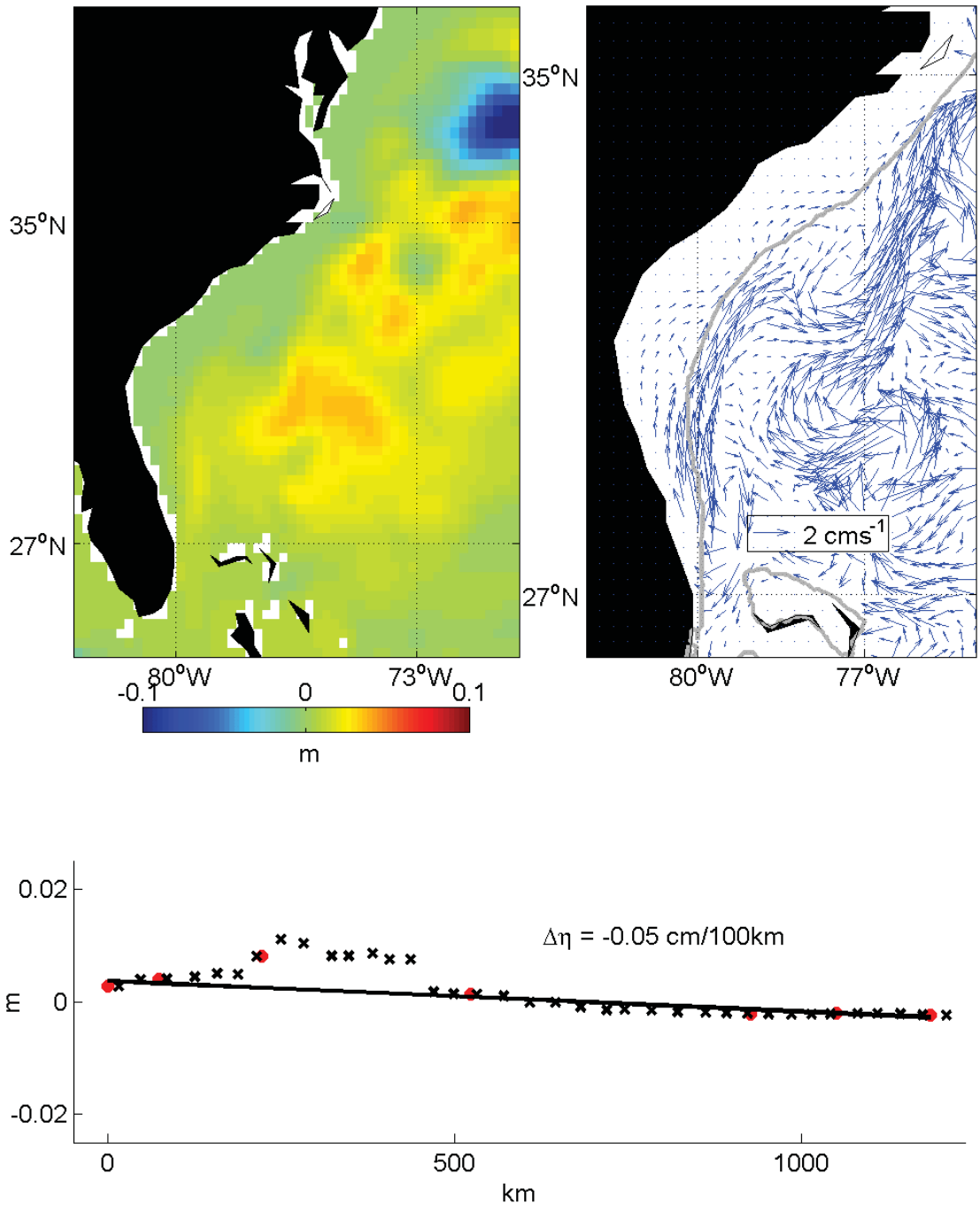

Figure 7.11: Sea level and current anomalies resulting from the density perturbation experiment. As for Figure 7.10 but for the density perturbation run.

of Cape Hatteras, related to a shift in the position of the Gulf Stream separation and its recirculations. However the difference on the shelf of the SAB and the MAB is negligible.

The mean surface geostrophic velocity anomalies (Figure 7.11, top right panel) show an increase in the speed of the Gulf Stream, offshore of the 200 m isobath, but little or no change on the shelf. There is a correspondingly small change in coastal sea level (bottom panel), with a negligible alongshore slope. This run was repeated with different perturbations centred further from the shelf, but the result is not sensitive to the size or position of the perturbation.

It is worth noting that this experiment only tests the effect of near-local density forcing. The Gulf Stream is influenced by basin scale changes but these processes are not fully resolved by this relatively short run. It is also possible that the spectral nudging in the ocean model suppresses the propagation of disturbances.

7.5.5 The Local Wind Perturbation Experiment Results

The density perturbation experiment produces minimal change to $\Delta\eta$ and the remote wind perturbation increases the tilt, but by only about one-tenth of the mean signal. This raises the question of what is causing the larger mean tilt?

The alongshore mean sea level from the local wind perturbation experiment is shown in Figure 7.12, for both the control run (middle panel) and the zero-wind run (bottom panel). South of about 27°N, in the Straits of Florida and along the Florida Keys, there is almost no difference between the sea level from the two runs. North of 27°N, however, there is less of a downward tilt toward the north in the zero-wind run. Linear regressions of sea level onto distance from Key West are undertaken using only the tide gauge stations south of 27°N and north of 27°N . These show that south of 27°N the slope ($\Delta\eta_S$) is almost identical but north of 27°N the slope ($\Delta\eta_N$) in the perturbed run is less than half of the value from the control run. For comparison the regression is also shown using all tide gauge locations ($\Delta\eta_{total}$). A physical interpretation of these results is presented in the next section.

7.6 Discussion

Previous studies have suggested that there is a tilt in sea level along the coast of the South Atlantic Bight, downwards toward the north. However geodetic levelling has not been sufficiently accurate in the past to directly observe this tilt.

By referencing tide gauge measurements to a new, more accurate geoid model it is shown that a tilt in mean sea level exists, and the slope of the tilt agrees with earlier estimates. The mean tilt is reproduced by the Glorys2v1 ocean reanalysis, and there is good agreement between the tide gauge observations and the ocean reanalysis for the seasonal and monthly variability of the tilt.

In order to understand the mean tilt, its variability is investigated by quantifying the statistical relationships between the tilt ($\Delta\eta$) and sea level, surface currents and density using the ocean reanalysis. The main relationships are with sea level along the shelf, with alongshore surface currents on the shelf, and with the Gulf Stream surface speed. Similar statistical relationships are quantified between the tilt and the surface wind fields and the surface wind stress curl. The tilt is related to southwesterly winds over the northern SAB, and with negative wind stress curl over the adjacent deep ocean.

Two mechanisms are identified that are consistent with the statistical analysis and may contribute to the observed variability of $\Delta\eta$: Remote shelf wind stress, and Gulf Stream variability related to deep ocean processes. The contribution of these mechanisms to the mean tilt is explored using an ocean model sensitivity study.

Figure 7.12 *(following page)*: Alongshore sea level for the local wind perturbation experiment. (Top panel) The black line shows the extent of the region for which the wind forcing is set to zero. The filled red circles show the location of the tide gauges, and the grey line shows the position of the 200 m isobath, indicating the shelfbreak. (Middle panel) Mean coastal sea level from the control run at tide gauge locations (filled red circles) and intermediate points (black crosses). The black lines show the linear regressions using only the sea level at the tide gauge locations from Key West to Cape Canaveral, and from Cape Canaveral to Myrtle Beach. The dashed line shows the linear regression using all tide gauge locations. The slope of the regression is shown for each line ($\Delta\eta_S$, $\Delta\eta_N$ and $\Delta\eta_{total}$ respectively). (Bottom panel) As for the panel above, but for the zero-wind run.

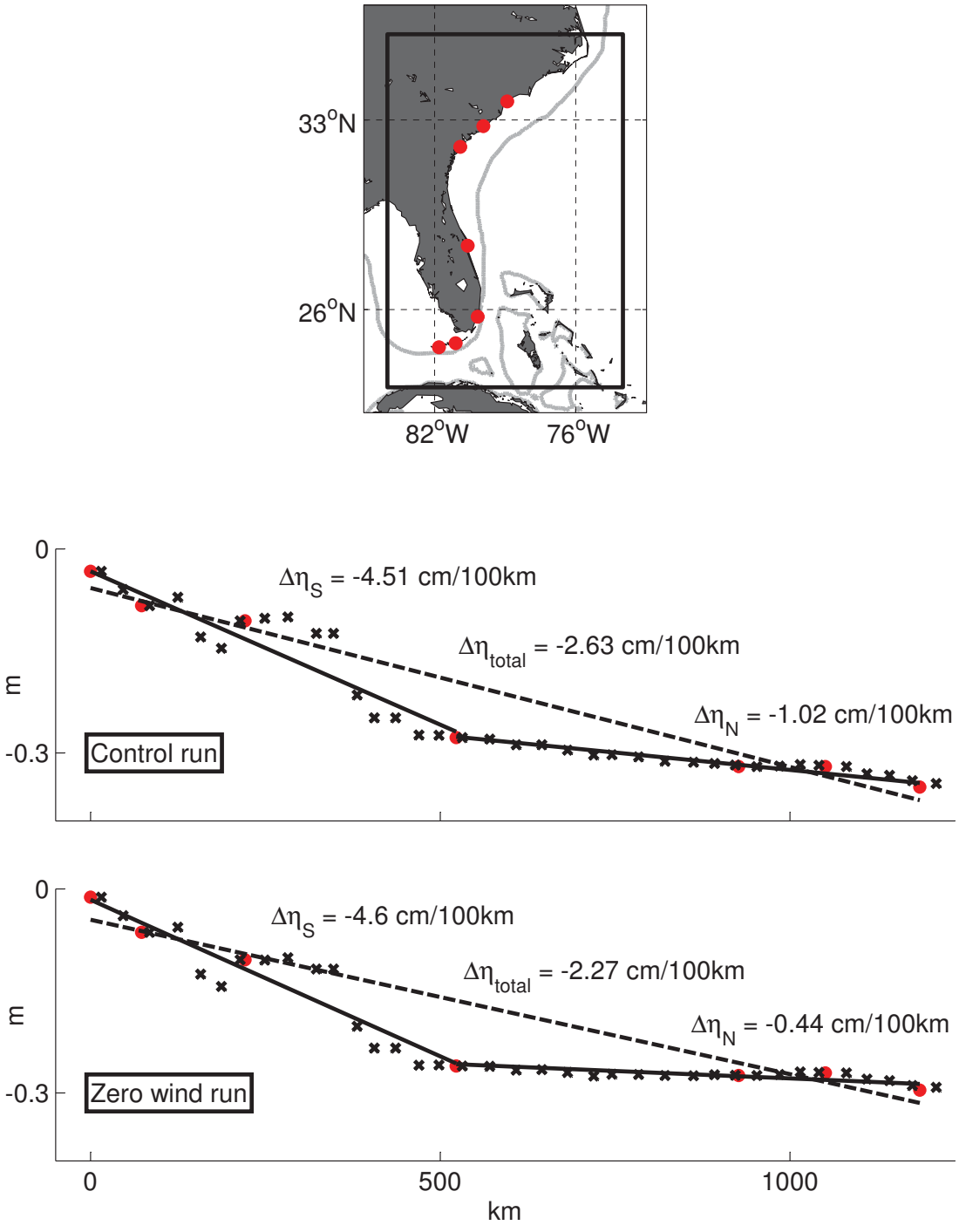
33°N
26°N
82°W
76°W
0
-0.3
m
Δη_S = -4.51 cm/100km
Δη_total = -2.63 cm/100km
Δη_N = -1.02 cm/100km
Control run
0
-0.3
m
Δη_S = -4.6 cm/100km
Δη_total = -2.27 cm/100km
Δη_N = -0.44 cm/100km
Zero wind run
0
500
1000
km

The remote wind perturbation experiment examines the effect of a southwesterly wind perturbation over the northern SAB and the MAB. The mean sea level anomaly at the coast is similar to the observed mean tilt, although the magnitude of the slope is much less. Mean surface current speeds are increased on the shelf and in the Gulf Stream. The effect propagates to the south of the region where the wind perturbation is applied, consistent with observations of coastal trapped waves propagating southward in earlier studies. The process by which the wind influences sea level could be barotropic, with simple wind setup, or baroclinic, with the alongshore wind producing upwelling. The statistical relationship between density and $\Delta\eta_{tg}$ hints at dense waters moving onto the bottom of the shelf, which is consistent with upwelling. However the rapid propagation of the sea level signal southwards along the shelf is more likely barotropic.

The density perturbation experiment uses isopycnal displacements to represent one of the effects of a change in the wind stress curl. This influences the Gulf Stream surface speed, as expected from previous studies (e.g. *DiNezio et al.* [2009]), but the effect on the shelf is weak. From Miami (the third tide gauge record) northward, the slope of the mean sea level anomaly is almost flat. This suggests that either the Gulf Stream does not have a significant effect on the mean tilt, wind stress curl influences the circulation and the tilt in some way other than through the displacement of isopycnals in the ocean interior, or spectral nudging in the model is supressing the response.

The remote wind perturbation and the density perturbation experiments are designed to test the effect of these mechanisms on the mean tilt. Whilst the results help to understand the observed variability in $\Delta\eta_{tg}$, the experiments produce sea level responses that are too small to account for the observed mean tilt. However the final sensitivity study, setting the local wind to zero, helps to understand the mean tilt.

Alongshore sea level north of the Straits of Florida tilts downward toward the north in the control run. The alongshore flow is very weak ($< 0.1\text{ms}^{-1}$ on the shelf, and somewhat less at the coast). The alongshore momentum balance (7.7) is between the alongshore pressure gradient (the tilt) and the friction and advection terms. For a weak flow these terms will be small, and the tilt is correspondingly small. The tilt response produced by the

earlier remote wind experiment is comparable with this tilt. When the wind is turned off (Figure 7.12), the tilt almost disappears. This suggests that the observed mean alongshore tilt is related to the weak currents produced by local and remote shelf wind forcing. The Gulf Stream does not play a major role in driving the mean tilt, probably because the continental shelf provides an insulating effect.

At the southern end of the study region, between Key West and Cape Canaveral, there is a much steeper sea level tilt. This can be seen in mean sea level from the zero wind runs (Figure 7.12), in the Glorys ocean reanalysis and in the tide gauge observations (Figure 7.1). The magnitude of the tilt is around 4 cm 100km^{-1}. In this area the Florida Current passes close to shore and there is little or no continental shelf to insulate the coast. As a result the current speed at the coast is relatively high. Returning to the momentum balance (7.7), the friction and advection terms are much larger than for the weak alongshelf flow further north, and these terms are balanced by a higher alongshore pressure gradient i.e. a steeper tilt.

The tilt of mean sea between Key West and Cape Canaveral varies in the alongshore direction in all of the estimates, with the steepest tilt between Miami and Cape Canaveral. The width of the shelf varies alongshore, and there are corresponding changes in the speed of the current near the shore, but the full reasons for the observed alongshore variability in the tilt are not clear. This is an area for further investigation using a higher resolution ocean model.

Returning to the temporal variability of the tilt, analysis using the Glorys2v1 ocean reanalysis product shows that the monthly tilt between Key West and Cape Canaveral is correlated with the maximum speed of the Florida Current at 26°N (r=0.68 with the seasonal cycle removed from both time series). This indicates that there is potential to use the coastal tide gauges as part of a Gulf Stream observing system, but it is only the alongshore tilt of sea level through the Florida Straits that is important.

In conclusion there are different processes that contribute to the tilt north and south of Cape Canaveral. To the north, where the shelf insulates the coast from the Gulf Stream, a small alongshore tilt is associated with weak alongshore flow forced by local and remote

alongshore winds. To the south of Cape Canaveral, where the shelf is much narrower, the mean tilt is larger and related to the main Gulf Stream flow. Variability of $\Delta\eta_{tg}$ is correlated with the variability of the Gulf Stream speed, which is forced at the basin scale. This suggests that the southern tide gauges, from Key West to Cape Canaveral, hold some value as part of an ocean observing system.

CHAPTER 8

DISCUSSION

New oceanographic and geodetic observations and a new ocean observation correction technique are used to produce estimates of the mean surface circulation of the North Atlantic. The new estimates are compared and evaluated using independent observations, statistical analysis and an ocean model. A summary of the thesis is given below, followed by a discussion about the significant contributions from this work.

8.1 Summary of Thesis

Two new North American geoid models are described in Chapter 2. Both incorporate terrestrial, altimeter and GRACE satellite gravity measurements, and one additionally includes data from the GOCE satellite gravity mission. The geoid models are combined with satellite altimeter-measured mean sea surface height fields to produce new estimates of the MDT (Objective 2, as outlined in Section 1.5). The mean surface geostrophic circulation is calculated from the gradients of the MDT fields. Qualitatively both geoid models produce realistic estimates of the mean circulation, although the one that incorporates GOCE data includes fewer spurious short wavelength features.

In Chapter 3 an improved estimate of the mean state of the temperature salinity (TS) structure of the North Atlantic is described (Objective 1). A new technique was developed for removing mesoscale variability from oceanographic temperature and salinity (TS) profile measurements. This technique combines subsurface hydrographic information with co-located surface measurements from satellite altimeters. Measured TS profiles are

corrected for the effect of vertical water column displacements associated with mesoscale eddies.[1] Reducing the variance of TS measurements allows a TS climatology to be produced using a shorter dataset than has traditionally been necessary, thereby reducing the misrepresentation of low frequency variability associated with conventional multi-decadal climatologies. The technique is applied to TS profiles measured by the Argo network of drifting profilers, and used to produce a new TS climatology for the North Atlantic relating specifically to the period 2000 to 2007. It is shown that the new period-specific climatology produces a more realistic representation of the MDT gradients across the Gulf Stream as it moves offshore from Cape Hatteras.

The new Argo-period climatology is used in Chapter 4 to produce improved oceanographic estimates of the MDT and hence the mean circulation relating specifically to the Argo period (Objective 2). Estimates are produced using both a conventional steric height approach and using an ocean circulation model that is spectrally nudged toward the new climatology. A comparison of the two approaches illustrates that the ocean model method produces a more complete estimate of the mean circulation. A comparison with similar estimates produced using the World Ocean Atlas 2001 (WOA01) climatology shows differences in the Gulf Stream region which are evaluated later.

In Chapter 5 the new geodetic and oceanographic estimates of the mean circulation are compared for the subpolar gyre region.[2] The estimates are evaluated against estimates of the mean circulation from ocean drifters and from other in situ ocean measurements (Objective 3). It is shown that the geodetic estimate is a significant improvement over earlier geodetic estimates because of improvements in the representation of high wavenumber features of the geoid. The geodetic MDT produces a mean circulation estimate that is realistic, comparing well qualitatively and quantitatively against other measurements including an

[1] A version of this chapter has been published as: Higginson, S., K.R. Thompson, and Y. Liu, Estimating ocean climatologies for short periods: A simple technique for removing the effect of eddies from temperature and salinity profiles, *Geophysical Research Letters*, 36, L19602, 2009.

[2] A version of this chapter has been published as: Higginson, S., K.R. Thompson, J. Huang, M. Véronneau, and D.G. Wright, The mean surface circulation of the North Atlantic subpolar gyre: A comparison of estimates derived from new gravity and oceanographic measurements, *Journal of Geophysical Research, Oceans*, 116, C08016, 2011.

estimate of the mean derived from surface drifter data. Small scale features such as the East Greenland Coastal Current are visible in the estimate, although the quality of the estimate degrades close to shore because of increased errors in the altimeter-derived mean sea surface. The oceanographic MDT produces a reasonably realistic estimate of the mean circulation but frequently the current speeds are lower than for other estimates.

A similar comparison of the new estimates is undertaken in Chapter 6 for the Gulf Stream system (Objective 3). The geodetic estimate used in this Chapter is based on a geoid that additionally includes gravity data from the GOCE satellite mission. It is shown that there is a significant improvement in the geodetic estimate for this region compared with the estimate using the pre-GOCE geoid (Objective 4). The comparison of the new geodetic estimate of the surface circulation with drifter estimates shows good agreement, and where the current is constrained by bathymetry the estimates are almost identical. The oceanographic estimate, produced using the new Argo-period climatology, is an improvement over an estimate produced using a multi-decadal climatology, although the improvement is not as large as expected. The new estimate is in reasonable agreement with other estimates where the current is constrained by bathymetry, but there are some differences in the path of the currents in deep water.

Although the geodetic estimates are realistic in the open ocean, it is shown that there are problems close to the coast because of the reduced accuracy of mean sea surface height fields derived from satellite altimeter measurements. In Chapter 7 a complementary approach is investigated, using tide gauge records from Florida and the South Atlantic Bight (SAB) in place of the altimeter sea surface heights (Objective 5). Whilst the tide gauge records lack the spatial coverage of altimeter measurements they provide accurate long-term measurements of mean sea level at the coast. Historically it has been difficult to compare absolute sea level between tide gauges because of the errors in geodetic levelling between stations. In this work the tide gauge records are referenced to the new geoid model and the alongshore tilt of mean sea level is estimated between Key West, Florida and Myrtle Beach, South Carolina. This compares favourably with earlier estimates of the alongshore tilt, including ocean model estimates.

The temporal variability of the alongshore tilt in the SAB is used to investigate the processes contributing to the observed tilt. Statistical methods are used to investigate relationships between temporal variability of the tilt and sea surface height, density and surface currents in an ocean model reanalysis. A similar approach is used to investigate relationships with surface wind stress fields from an atmospheric model reanalysis. This shows a relationship between the temporal variability of the tilt and remote wind forcing over the northern SAB and over the Middle Atlantic Bight (MAB). Ocean model sensitivity experiments are used to investigate the influence of this remote wind forcing on the mean tilt. These experiments show that, whilst the remote wind forcing does influence the temporal variability of the tilt, with evidence pointing to coastal trapped waves propagating southward, the effect is limited to the relatively small tilt north of the Straits of Florida. A further experiment has the local wind switched off over the SAB shelf. In this experiment the mean tilt along the SAB shelf disappears, but a mean tilt remains in the Straits of Florida. It is suggested that this is likely the result of a dynamical balance between friction and the alongshore pressure gradient as the Gulf Stream passes through the Straits.

8.2 Discussion

Although the surface circulation of the North Atlantic has been extensively measured and mapped, differences between the various estimates remain. Two factors may account for these differences. Firstly different observing systems have been used at different times, ranging from simple ship drift measurements to advanced satellite remote sensing techniques. Each has different biases, resolution and spatial and temporal distributions. Secondly the ocean is a non-stationary system, and the mean for one period may differ from the mean for a different period. The conventional approach of defining a long-term climatology is really not appropriate for such a system.

In this thesis two new estimates of the mean circulation are described, one from geodetic data and one from oceanographic data. Each uses a different observing system with different approaches to maximize the spatial and temporal homogeneity of the measurements contributing to the estimates. And each estimate relates specifically to the relatively short period from 2000 to 2007, rather than trying to define the mean for a multi-decadal period.

The geodetic approach is shown to produce realistic estimates of the mean circulation that compare favourably with other estimates. This estimate has the most temporally and spatially homogeneous observations, and the fewest biases of the various estimates produced or compared in this thesis. Satellite altimeter measurements are near global and high resolution with regular and frequent resampling, subject only to accuracy issues in the coastal region and biases in ice-covered waters. The geoid model is constructed from gravity measurements which are not temporally uniform, but the magnitude of the geoid changes over this relatively short time period are small. The terrestrial gravity measurements are spatially inhomogeneous but new satellite gravity measurements, especially from the GOCE mission, reduce the influence of this inhomogeneity.

The oceanographic estimate is produced from a new period-specific TS climatology. The new de-eddying technique described in Chapter 3 is key to producing this climatology. The technique reduces the variance of the TS measurements, so the mean can be defined from a smaller dataset. Reducing the variance of the observations by half is equivalent to increasing the number of observations by a factor of four. Another important contribution toward this new oceanographic estimate is the Argo network of drifting profilers. This network is global with reasonably uniform coverage of the oceans where the depth is greater than 2000 m. The resolution is high compared to many other in situ ocean measurements with a target of one profiler in every 3° box on average. The spatial homogeneity is also high although temporally there is a bias toward the end of the analysis period.

Compared to these two new estimates, many other measurements of the ocean circulation are simple snapshots at a given time and location. Although some long time series exist, such as measurements of the Gulf Stream in the Straits of Florida, these are relatively rare. The Global Drifter Program maintains global coverage but analysis in the course of this study has shown that the results in some areas are prone to large variations depending on the averaging period chosen. Spatial coverage is also not uniform with concentrated deployments in some areas related to specific regional studies.

The geodetic approach has yielded new estimates of the mean flow in the coastal currents of the poorly sampled subpolar gyre. Earlier observations in this region have been strongly

biased toward the summer months. The new geodetic estimate has a bias in some areas because of ice coverage, but this bias is shown to be of relatively limited spatial extent. The mean flow is broadly in agreement with the drifter estimate, but faster in some areas. The drifter estimate is often based on relatively few observations, and as such there is frequently a seasonal or other temporal bias which could account for the difference in estimated current speeds. In the Gulf Stream system there is also good agreement between the geodetic and drifter estimates of the mean circulation. This region is frequently sampled by drifters, with little temporal or spatial bias. The level of agreement between the drifter estimate and the geodetic estimate illustrates how well the geodetic approach is performing.

The oceanographic estimate in the high variability Gulf Stream region is shown to be an improvement over estimates based on multi-decadal TS climatologies. Conventional climatologies smooth the gradient across the Gulf Stream, leading to poor estimates of the speed and position of the mean flow. It is shown that this is improved using the new period-specific climatology but there are still differences in the Gulf Stream separation and the path of the free jet. This is perhaps an indication of the difficulty of measuring this highly variable part of the ocean with sufficient observational density in time and space.

Whilst the new TS climatology may not produce estimates of the mean circulation that are as good as the geodetic approach, it does highlight changes in the heat content of the ocean. The WOA01 climatology is produced using observations collected over more than a century. The MDT from the new Argo-period climatology shows an increase in height compared to WOA01, especially in the subpolar gyre region. This points to warming of the water column compared to the earlier climatology, and is consistent with observations by, for example, *Hakkinen and Rhines* [2009]. With additional observations in future years both the oceanographic and geodetic approaches can be applied to other specific time periods. This will lead to new estimates of the low frequency changes in the ocean, which can be validated by comparison with each other.

The coastal region is problematic for the geodetic approach because of errors in the altimeter measurements. Although new altimeter products are in development there are not yet sufficient data to improve the geodetic estimates of the mean circulation. The

alternative approach described in Chapter 7, replacing altimeter measurements with tide gauge measurements, yields interesting results. Tide gauges provide accurate long term measurements of sea level at the coast but it has not been possible to directly compare measurements between gauges because of errors in geodetic levelling. In this thesis the new geoid model is used with the tide gauges to produce an estimate of the mean alongshore tilt that agrees well with earlier indirect estimates and with estimates from ocean models.

Statistical and modelling approaches are used to investigate the alongshore tilt, and this highlights how these two approaches are different but complementary. Statistical analysis identifies relationships between the temporal variability of the tilt and remote wind forcing. However the ocean model sensitivity studies show that, whilst the remote wind forcing contributes to the temporal variability it does not have a significant impact on the mean tilt. The mean tilt in the Straits of Florida is shown to be independent of the wind, and likely related to the speed of the Florida Current. With an understanding of the physics there is potential to use tide gauges as part of a monitoring system for the Florida Current. This is an area that requires further investigation.

In conclusion, the accuracy of the geoid models is now sufficient that the geodetic approach yields realistic and useful estimates of the mean surface circulation that are superior to those obtained using oceanographic data. This is a realization of the long time dream of oceanographers to be able to observe the mean circulation from space. Future improvements in the accuracy of the geoid, through incorporation of additional data from the GOCE satellite mission or from terrestrial measurements, will likely improve the resolution of the estimates and allow improved mapping of small scale mean circulation features. However the accuracy and resolution of the geoid models is approaching the point at which improvements to the resolution of altimeter measurements will be required in order to further improve estimates of the mean ocean circulation.

APPENDIX A

CALCULATION OF THE PCG08I GEOID MODEL

There are two main steps in creating the geoid model: The realization of the marine gravity grid, and the computation of the geoid model. In the following sections I will look at each of these steps, and the resolution and error estimate for the PCG08I geoid model.

A.1 The Marine Gravity Grid

The marine gravity field of PCG08I is defined on a 2 minute by 2 minute grid. It incorporates shipboard gravity data, six gravity models derived from satellite altimetry and the Arctic Gravity Project 2008 (ArcGP08) dataset (http://earth-info.nga.mil/GandG/wgs84/agp/readme_new.html). The six altimetry-derived gravity models are: GSFC00 (*Wang* [2001]), CLS01 (CLS, France), NTCU01 (*Hwang et al.* [2002]), KMS02 (*Andersen et al.* [2005]), DNSC08 (*Andersen et al.* [2010]), and Sandwell and Smith v9 (*Sandwell and Smith* [2009]).

The realization of the marine gravity grid, carried out by NRCan, follows a multi-step approach. There are seven steps, and grid points retain their values at each step, i.e., only undefined grid points are filled at each step. The steps are:

1. The shipboard gravity data are compared to each of the altimetry-derived gravity models. If the difference is 2 mGal or less the mean of the two values is assigned to the grid point.

2. For remaining gaps along the Atlantic coast of Canada (Labrador, Newfoundland, Nova Scotia), shipboard gravity data are used where available.

3. The eight gravity datasets (shipboard, six altimetry-derived models and ArcGP08) are averaged and, if the range of the eight data are equal to or less than 5 mGal, the mean is assigned to the grid point.

4. The three datasets (Shipboard, ArcGP08 and DNSC08), covering most of the Arctic region, are averaged and used if the range is equal to or less than 5 mGal.

5. The mean of the six altimetry-derived grids is used if the range of the six values at a grid point is 3 mGal or less.

6. The mean of ArcGP08 and DNSC08 is used if the difference is 5 mGal or less.

7. Finally the remaining grid points over the oceans are filled using the DNSC08 altimetry-derived gravity model.

Hence the resulting gravity grid is a comprehensive combination of the different gravity datasets. Along the east coast of Canada the gravity values are generally shipboard measurements or the mean of shipboard and altimeter-derived values. Around the coasts of Greenland the values are generally either the mean of shipboard, altimeter and ArcGP08 data, or altimeter-derived values. In the open ocean the altimeter-derived values dominate.

A.2 Computation of the Geoid Model

The geoid model is calculated by blending the marine gravity grid and terrestrial land gravity observations with GRACE data using the Stokes-Helmert method (e.g. *Huang and Véronneau* [2005]). The following is based primarily on the description in *Thompson et al.* [2009].

The basic idea of this method is to first "condense" the Earth's topography onto an infinitesimally thin layer coincident with the geoid, then solve a geodetic boundary value

problem to find the Helmert geoid, and finally correct for the height difference between the Helmert geoid and the true geoid. This can be summarized as

$$N = c + N_H + \delta N_{pite} \tag{A.1}$$

where N is the true geoid height, c is the sum of 3 corrections terms, N_H is the Helmert geoid height, and δN_{pite} is the primary indirect topographic effect (a correction for errors caused by the condensation, related to the Earth's topography).

The Helmert geoid is derived from the GRACE data and the marine/land gravity grid using

$$N_H = N_H^S + \frac{R}{4\pi\gamma}\int_\Omega S^W(\psi)(\Delta g^{TH} - \Delta g^{SH})d\Omega \tag{A.2}$$

where N_H^S is the Helmert geoid from a satellite model, R is the radius of the Earth, γ is the normal gravity on the reference ellipsoid, Δg^{TH} is the observed terrestrial gravity anomalies and Δg^{SH} is the observed satellite gravity anomalies. The region of integration, Ω, is a spherical cap centred on the point of interest, and $S^W(\psi)$ is a weighted degree-banded Stokes kernel function which varies only with angular distance ψ from the point of interest.

For PCG08I N_H^S and Δg^{SH} are from the EGM2008 model (*Pavlis et al.* [2012]), truncated to degree/order 360, and Δg^{TH} comes from the land/marine gravity grid. The weighting scheme adopted for the Stokes integral allows the geoid to be determined predominantly from EGM2008 at low degrees (up to degree 60, or a half wavelength of 333 km), and predominantly from the land/marine gravity grid at higher degrees (above degree 90, or a half wavelength of 222 km). EGM2008 is dominated by GRACE data up to degree 90, so the low-degree part of PCG08I is similarly dominated by the GRACE contribution.

The region of integration of the Stokes function is a spherical cap of 6 arc degrees (corresponding to a radius of approximately 660 km). The far zone contribution is entirely from EGM2008.

The model is defined on a grid with a resolution of 2 arc minutes ($\frac{1}{30}^\circ$), although the true resolution of the geoid depends on the density of the terrestrial gravity measurements.

Where there is no terrestrial data, the resolution is limited to the satellite contribution (degree 90).

A.3 Error estimation

There are three main sources of error in a geoid model computed using this approach. Firstly there is the commission error in the the EGM2008 model. The full covariance matrix of the error coefficients is not publicly available, but the error of low-degree components (less than degree 90) is less than 3 cm. The second source of error is the error in terrestrial gravity anomalies. These range from a few centimetres to decimetres, with the lowest values close to the Canadian east coast where the shipboard gravity observations are most dense. The final source of error is the far field contribution from EGM2008, which is estimated at approximately 0.4 cm. This gives a total geoid error that is typically between 1 cm and 5 cm over the northwest Atlantic Ocean. The approach for estimating geoid error is described in *Huang et al.* [2007].

APPENDIX B

AN OPTIMAL INTERPOLATION TECHNIQUE

B.1 Optimal Interpolation

Optimal interpolation (OI) or objective analysis was introduced to oceanography by *Bretherton et al.* [1976]. OI estimates a variable X from a weighted linear combination of observations Y which are irregularly located in space and time (*Wilkin et al.* [2002]). The weights minimize the total mean squared error. The estimate at a grid of locations is given by

$$X(x, y) = CA^{-1}Y \tag{B.1}$$

where C is the covariance vector of the estimated variable with the observations, and A is the covariance matrix of the observations with each other.

B.2 The Correlation Function

The OI technique requires estimates of the covariance, C and A.

For the covariance of the estimated variables with the observations C, a form of compactly supported correlation function is used which was originally constructed by *Gaspari and Cohn* [1999] and was described by *Gneiting* [2002]. The function used here takes the form

$$\psi(t) = \frac{\phi}{(1 + (t/L)^2)} \tag{B.2}$$

where L is a scale parameter, t is the distance between points and

$$\phi(t) = \begin{cases} 1 - \frac{20}{3}T^2 + 5T^3 + 8T^4 - 8T^5 & 0 \leq T \leq \frac{1}{2} \\ \frac{1}{3}T^{-1}(8T^2 + 8T - 1)(1 - T)^4 & \frac{1}{2} \leq T \leq 1 \end{cases} \tag{B.3}$$

where T is the ratio of the distance t to the scale distance L.

The covariance of the observations with each other is composed of two parts, since an observation Y can be considered as

$$Y = S + \epsilon \tag{B.4}$$

where S is the "signal" or true value and ϵ is the measurement error. The covariance estimate is made up of the covariance of the true values with each other and the covariance of the measurement errors. Assuming that the errors are uncorrelated the total covariance estimate is given by

$$A = \Sigma_S + \Sigma_\epsilon \tag{B.5}$$

where Σ_S is the covariance of the signal, estimated using the compactly supported correlation function described above, and Σ_ϵ is the covariance of the errors, given by a diagonal matrix. The value of the diagonal is determined by the signal-to-noise ratio in the observations, with a diagonal value near 0 producing an interpolated field that passes close to the observed values.

B.3 Application to TS Observations

In this study the OI technique is used to map a TS climatology from irregularly located TS profiles. A background is chosen, in this case the WOA01 climatology, and the observations (Y) and estimates (X) are expressed in terms of anomalies relative to WOA01. The anomaly fields are estimated using (B.1), with correlation functions C and A calculated as (B.2) and (B.5). The resulting estimates (or increments) are added to the background field, WOA01, to produce the new climatology.

APPENDIX C

SEASONAL BIAS IN OBSERVATIONS

Most in situ observations of the circulation of the northwest Atlantic subpolar gyre have been made during the summer months when there is little or no ice coverage. Where observations have been year-round seasonal variations in current speed have been observed. For example *Lazier and Wright* [1993] observed seasonal variability in the Labrador Current with a maximum in October and a minimum in April. The alongshore surface current speed varies by a factor of two between the minima and maxima and they speculated that this is caused by buoyancy forcing with ice melt and river runoff contributing freshwater to the system during the spring and summer. It is possible that the current descriptions of the circulation, largely being based on summer observations, incorporate a seasonal bias.

Both the geodetic estimate (MDT_G) and the oceanographic estimate (MDT_{Argo}) are intended to represent the temporal mean dynamic topography and hence the mean surface circulation. Since the circulation does vary seasonally, it is important to understand whether the estimates really are seasonally unbiased.

MDT_G is derived from the geoid and the altimeter-derived mean sea surface. Seasonal changes in the currents will be reflected in changes in the mean sea surface height measured by the altimeters. Since altimeters operate from space, and the observation record has been continuous since 1992, it is easy to assume that there is no seasonal bias to the observations. But satellite altimeters are unable to measure sea surface height where there is old, multi-year sea ice and so there will be fewer sea surface height measurements in areas of sea ice than in ice-free areas.

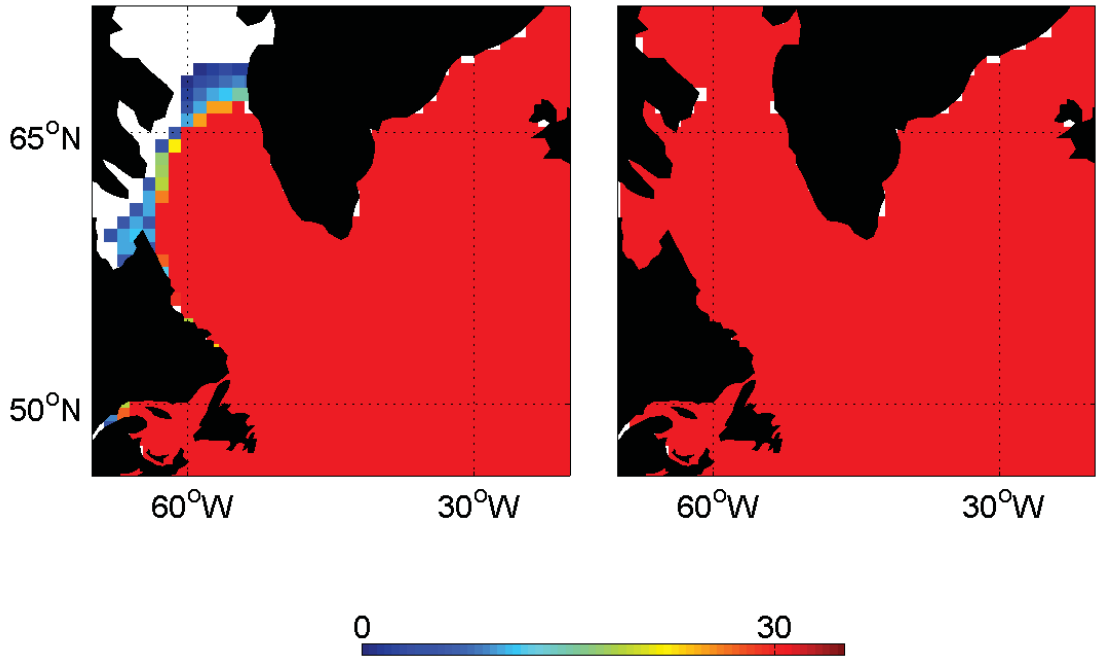

Figure C.1: (Left panel) Number of daily measurements from the Aviso Delayed Time $\frac{1}{4}^\circ$ gridded sea surface height anomaly product during March 2000. (Right panel) The same plot for September 2000.

The seasonal differences in altimeter observations for the subpolar gyre is illustrated by comparing the Aviso daily gridded sea surface height anomaly fields (http://www.aviso.oceanobs.com) for the months of March 2000 and September 2000, representing the ice season and the ice-free season respectively. Figure C.1, left panel, shows the total number of observations in each $\frac{1}{4}^\circ$ gridpoint for the month of March. This shows that, with the exception of the northern Labrador Sea, there is almost complete coverage. Figure C.1, right panel, shows a similar plot for September 2000, and there are no regions without coverage.

It is interesting to note that, looking at the coverage of individual altimeter tracks, there is less complete coverage along the coasts of Labrador and eastern Greenland during March. This indicates that sea ice was present and was restricting the availability of sea surface height measurements. However altimeters are frequently able to measure sea surface height in gaps in the ice, and the gridded product interpolates these measurements in space and time to provide more complete coverage.

Turning to the oceanographic estimate, MDT_{Argo}, there are two potential sources of seasonal bias. Firstly the Argo TS profiles may be less abundant in ice covered areas during the winter compared with the summer. However, since these floats are restricted to the largely ice-free waters deeper than 2000 m seasonal ice should not be a significant issue. Secondly the background field used in the optimal interpolation (WOA01) may include an inherent seasonal bias, but this is difficult to assess.

Finally it is noted that the independent oceanographic observations that are used for validation (surface drifters and in situ measurements) are also prone to the seasonal bias. For earlier regional studies, such as those cited in the text of Chapter 5, this is usually stated. For surface drifters, which are not restricted to deep waters in the same way as Argo floats, the bias in observation density is illustrated in Figure C.2. The left panel shows the density of observations from the Global Drifter Program (*Lumpkin and Pazos* [2007]), plotted as the total number of observations in $\frac{1}{4}^{\circ}$ bins, for all years from 1992 to 2009 during the months of January to June, when sea ice is typically present along the east coast of Greenland and the coast of Labrador. The right panel shows a similar plot for the months of July to December, when sea ice is typically not present. Some of the shelf regions along the coast of Greenland are poorly sampled during the winter, and the Labrador shelf is poorly sampled throughout the year. However, many of the shelfbreak regions where the main currents are located (shown by the 700 m isobath), are sampled in both summer and winter.

Although there is clearly some seasonal bias in the observation datasets, there is no evidence of an effect on the resulting estimates. The quantitative comparison of each of the topographies and the resulting estimates of surface circulation has been repeated using only data from the ice-free season and this shows little change to the results. Although there may be a seasonal bias in the observational data, it seems that, at the scales considered in this study, seasonality is not an issue. For future work at finer resolution this may become a concern, particularly for studies of the coastal currents on the shelves where ice forms.

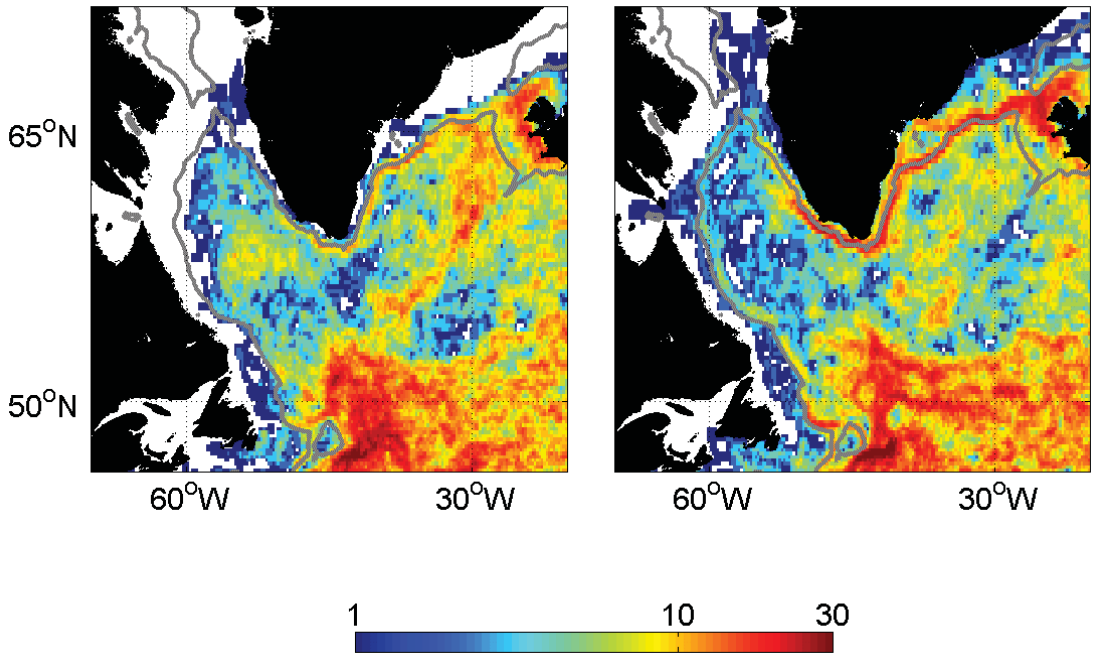

Figure C.2: (Left panel) Number of observations from the Global Drifter Program, plotted on a log scale in $\frac{1}{4}^{\circ}$ bins, during the months from January to June for all years from 1992 to 2009. (Right panel) The same plot for the months from July to December. The grey line shows the approximate position of the 700 m isobath, which approximates the shelf edge.

BIBLIOGRAPHY

Amalvict, M., and J. Boavida, The geoid: From geodesy to geophysics and from geophysics to geodesy, *Surv. Geophys.*, *14*, 477–494, 1993.

Andersen, O., P. Knudsen, and R. Trimmer, Improved high resolution altimetric gravity field mapping (the KMS2002 Global Marine Gravity Field), in *A Window on the Future of Geodesy*, edited by F. Sanso, vol. 128 of *International Association of Geodesy Symposia*, pp. 326–331, Springer Berlin Heidelberg, 2005.

Andersen, O., P. Knudsen, and P. Berry, The DNSC08GRA Global Marine Gravity Field from double retracked satellite altimetry, *J. Geod.*, *84*, 191–199, 2010.

Atkinson, L., J. Blanton, W. Chandler, and T. Lee, Climatology of the southeastern United States continental shelf waters, *J. Geophys. Res.*, *88*, 4705–4718, 1983.

Auer, S., Five-year climatological survey of the Gulf Stream system and its associated rings, *J. Geophys. Res.*, *92*, 11709–11726, 1987.

Bacon, S., P. G. Myers, B. Rudels, and D. A. Sutherland, Accessing the inaccessible: Buoyancy-driven coastal currents on the shelves of Greenland and Eastern Canada, in *Arctic-Subarctic Ocean Fluxes: Defining the Role of the Northern Seas in Climate*, edited by R. R. Dickson, J. Meincke, and P. Rhines, chap. 28, pp. 703–722, Springer Netherlands, 2008.

Bane Jr, J., and W. Dewar, Gulf Stream bimodality and variability downstream of the Charleston Bump, *J. Geophys. Res.*, *93*, 6695–6710, 1988.

Baringer, M., and J. Larsen, Sixteen years of Florida Current transport at 27°N, *Geophys. Res. Lett.*, *28*, 3179–3182, 2001.

Batchelor, G., *An introduction to fluid dynamics*, Cambridge University Press, Cambridge, UK, 1967.

Benveniste, J., Radar altimetry: Past, present and future, in *Coastal Altimetry*, edited by S. Vignudelli, A. Kostianoy, P. Cipolline, and J. Benveniste, chap. 1, pp. 1–17, Springer-Verlag, 2011.

Bingham, R., and K. Haines, Mean dynamic topography: intercomparisons and errors, *Philosophical Transactions of the Royal Society A: Mathematical, Physical and Engineering Sciences*, *364*, 903–916, 2006.

Bingham, R., K. Haines, and C. Hughes, Calculating the oceans mean dynamic topography from a mean sea surface and a geoid, *J. Atmos. Ocean. Tech*, *25*, 1808–1822, 2008.

Blaha, J. P., Fluctuations of monthly sea level as related to the intensity of the Gulf Stream from Key West to Norfolk, *J. Geophys. Res.*, *89*, 8033–8042, 1984.

Bouffard, J., S. Vignudelli, P. Cipollini, Y. Menard, et al., Exploiting the potential of an improved multimission altimetric data set over the coastal ocean, *Geophys. Res. Lett.*, *35*, L10601, 2008.

Boyer, T., S. Levitus, H. Garcia, R. Locarnini, C. Stephens, and J. Antonov, Objective analyses of annual, seasonal, and monthly temperature and salinity for the world ocean on a 0.25° grid, *Int. J. Climatol.*, *25*, 931–945, 2005.

Boyer, T., J. Antonov, H. Garcia, D. Johnson, R. Locamini, A. Mishonov, M. Pitcher, O. Baranova, and I. Smolyar, *World Ocean Database 2005*, S. Levitus, Ed., NOAA Atlas NESDIS 60, U.S. Government Printing Office, Washington, D.C., 190pp., 2006.

Bretherton, F., R. Davis, and C. Fandry, A technique for objective analysis and design of oceanographic experiments applied to MODE-73, *Deep-Sea Res.*, *23*, 559–582, 1976.

Brink, K., Coastal-trapped waves and wind-driven currents over the continental shelf, *Annu. Rev. Fluid Mech.*, *23*, 389–412, 1991.

Brooks, D., and J. Bane, Gulf Stream deflection by a bottom feature off Charleston, South Carolina, *Science*, *201*, 1225, 1978.

Cadden, D. D., R. Styles, and B. Subrahmanyam, Estimates of geostrophic surface currents in the South Atlantic Bight, *Mar. Geod.*, *32*, 334–341, 2009.

Castelao, R., Intrusions of Gulf Stream waters onto the South Atlantic Bight shelf, *J. Geophys. Res.*, *116*, C10011, 2011.

Chassignet, E. P., and D. P. Marshall, Gulf Stream separation in numerical ocean models, in *Geophys. Monogr. Ser.*, vol. 177, pp. 39–61, AGU, Washington, DC, 2008.

Chelton, D., J. Ries, B. Haines, L. Fu, and P. Callahan, Satellite altimetry, in *Satellite altimetry and earth sciences: A handbook of techniques and applications*, edited by L. Fu and A. Cazenave, chap. 1, pp. 1–131, Academic Press, 2001.

Clarke, R., Transport through the Cape Farewell - Flemish Cap section, *Rapports et procès-verbaux des réunions, Conseil International pour l'Exploration de la Mer*, *185*, 120–130, 1984.

Clarke, R., H. Hill, R. Reiniger, and B. Warren, Current system south and east of the Grand Banks of Newfoundland, *J. Phys. Oceanogr.*, *10*, 25–65, 1980.

Colbourne, E., B. deYoung, S. Narayanan, and J. Helbig, Comparison of hydrography and circulation on the Newfoundland Shelf during 1990–1993 with the long-term mean, *Can. J. Fish. Aquat. Sci.*, *54*, 68–80, 1997.

Cooper, M., and K. Haines, Altimetric assimilation with water property conservation, *J. Geophys. Res.*, *101*, 1059–1078, 1996.

Cuny, J., P. B. Rhines, P. P. Niiler, and S. Bacon, Labrador Sea boundary currents and the fate of the Irminger Sea water, *J. Phys. Oceanogr.*, *32*, 627–647, 2002.

Dickson, R., B. Rudels, S. Dye, M. Karcher, J. Meincke, and I. Yashayaev, Current estimates of freshwater flux through Arctic and subarctic seas, *Prog. Oceanogr.*, *73*, 210 – 230, 2007.

DiNezio, P., L. Gramer, W. Johns, C. Meinen, and M. Baringer, Observed interannual variability of the Florida Current: Wind forcing and the North Atlantic Oscillation, *J. Phys. Oceanogr.*, *39*, 721–736, 2009.

Ducet, N., P. Le Traon, and G. Reverdin, Global high resolution mapping of ocean circulation from Topex/Poseidon and ERS1/EES2, *J. Geophys. Res.*, *105*, 19477–19498, 2000.

Ekman, M., Impacts of geodynamic phenomena on systems for height and gravity, *J. Geod.*, *63*, 281–296, 1989, 10.1007/BF02520477.

ESA, Steady-State Ocean Circulation Mission., *Reports for Mission Selection, The Four Candidate Earth Explorer Core Missions*, *SP–1233 (1)*, European Space Agency, 1999.

Fichefet, T., and M. A. M. Maqueda, Sensitivity of a global sea ice model to the treatment of ice thermodynamics and dynamics, *J. Geophys. Res.*, *102*, 12609–12646, 1997.

Frankignoul, C., G. de Coëtlogon, T. Joyce, and S. Dong, Gulf Stream variability and ocean-atmosphere interactions, *J. Phys. Oceanogr.*, *31*, 3516–3529, 2001.

Fratantoni, D., North Atlantic surface circulation during the 1990's observed with satellite-tracked drifters, *J. Geophys. Res.*, *106*, 22,067–22,093, 2001.

Fratantoni, P. S., and R. S. Pickart, The western North Atlantic shelfbreak current system in summer, *J. Phys. Oceanogr.*, *37*, 2509–2533, 2007.

Fu, L., E. Christensen, C. Yamarone Jr, M. Lefebvre, Y. Ménard, M. Dorrer, and P. Escudier, TOPEX/POSEIDON mission overview, *J. Geophys. Res.*, *99*, 24369–24382, 1994.

Gaspari, G., and S. E. Cohn, Construction of correlation functions in two and three dimensions, *Q. J. R. Meteorol. Soc.*, *125*, 723–757, 1999.

Gerdes, R., W. Hurlin, and S. M. Griffies, Sensitivity of a global ocean model to increased run-off from Greenland, *Ocean Modell.*, *12*, 416–435, 2006.

Gill, A., and E. Schumann, The generation of long shelf waves by the wind, *J. Phys. Oceanogr.*, *4*, 83–90, 1974.

Gill, A. E., *Atmosphere-Ocean Dynamics*, Academic Press, 1982.

Gneiting, T., Compactly supported correlation functions, *J. Multivariate Anal.*, *83*, 493 – 508, 2002.

Griesel, A., M. R. Mazloff, and S. T. Gille, Mean dynamic topography in the Southern Ocean: Evaluating Antarctic Circumpolar Current transport, *J. Geophys. Res.*, *117*, C01020, 2012.

Guinehut, S., P. Le Traon, G. Larnicol, and S. Philipps, Combining Argo and remote-sensing data to estimate the ocean three-dimensional temperature fields – A first approach based on simulated observations, *J. Marine Syst.*, *46*, 85–98, 2004.

Hakkinen, S., and P. Rhines, Decline of subpolar North Atlantic circulation during the 1990s, *Science*, *304*, 555–559, 2004.

Hakkinen, S., and P. B. Rhines, Shifting surface currents in the northern North Atlantic Ocean, *J. Geophys. Res.*, *114*, C04005, 2009.

Halkin, D., and T. Rossby, The structure and transport of the Gulf Stream at 73°W, *J. Phys. Oceanogr.*, *15*, 1439–1452, 1985.

Heiskanen, W., and H. Moritz, *Physical Geodesy*, W.H. Freeman and Company, 1967.

Heywood, K., E. McDonagh, and M. White, Eddy kinetic energy of the North Atlantic subpolar gyre from satellite altimetry, *J. Geophys. Res.*, *99*, 22,525–22,539, 1994.

Holland, W. R., and A. D. Hirschman, A numerical calculation of the circulation in the North Atlantic Ocean, *J. Phys. Oceanogr.*, *2*, 336–354, 1972.

Holliday, N. P., A. Meyer, S. Bacon, S. G. Alderson, and B. de Cuevas, Retroflection of part of the east Greenland current at Cape Farewell, *Geophys. Res. Lett.*, *34*, L07609, 2007.

Huang, J., and M. Véronneau, Applications of downward-continuation in gravimetric geoid modeling: Case studies in Western Canada, *J. Geod.*, *79*, 135–145, 2005.

Huang, J., G. Fotopoulos, M. Cheng, M. Véronneau, and M. Sideris, *International Association of Geodesy Symposia, Volume 130: Dynamic Planet*, chap. On the estimation of the regional geoid error in Canada, pp. 272–279, Springer, 2007.

Hughes, C., and R. Bingham, An oceanographers guide to GOCE and the geoid, *Ocean Sci.*, *4*, 15–29, 2008.

Hwang, C., H.-Y. Hsu, and R.-J. Jang, Global mean sea surface and marine gravity anomaly from multi-satellite altimetry: Applications of deflection-geoid and inverse Vening Meinesz formulae, *J. Geod.*, *76*, 407–418, 2002.

Jayne, S., Circulation of the North Atlantic Ocean from altimetry and the Gravity Recovery and Climate Experiment geoid, *J. Geophys. Res.*, *111*, C03005, 2006.

Johannessen, J., et al., The European Gravity Field and Steady-State Ocean Circulation Explorer Satellite Mission Its Impact on Geophysics, *Surv. Geophys.*, *24*, 339–386, 2003.

Johns, W. E., T. J. Shay, J. M. Bane, and D. R. Watts, Gulf Stream structure, transport, and recirculation near 68°W, *J. Geophys. Res.*, *100*, 817–838, 1995.

Kalnay, E., et al., The NCEP/NCAR 40-year reanalysis project, *Bull. Am. Meteorol. Soc.*, *77*, 437–471, 1996.

Klein, B., and G. Siedler, On the origin of the Azores Current, *J. Geophys. Res.*, *94*, 6159–6168, 1989.

Krauss, W., Currents and mixing in the Irminger Sea and in the Iceland Basin, *J. Geophys. Res.*, *100*, 10851–10871, 1995.

Krauss, W., R. H. K. Se, and H.-H. Hinrichsen, The branching of the Gulf Stream southeast of the Grand Banks, *J. Geophys. Res.*, *95*, 13089–13103, 1990.

Large, W., and S. Yeager, The global climatology of an interannually varying air–sea flux data set, *Clim. Dyn.*, *33*, 341–364, 2009.

Lavender, K. L., R. E. Davis, and W. B. Owens, Mid-depth recirculation observed in the interior Labrador and Irminger seas by direct velocity measurements, *Nature*, *407*, 66–69, 2000.

Lazier, J. R. N., and D. G. Wright, Annual velocity variations in the Labrador Current, *J. Phys. Oceanogr.*, *23*, 659–678, 1993.

Leaman, K., R. Molinari, and P. Vertes, Structure and variability of the Florida Current at 27°N: April 1982 to July 1984, *J. Phys. Oceanogr.*, *17*, 565–583, 1987.

Leaman, K., E. Johns, and T. Rossby, The average distribution of volume transport and potential vorticity with temperature at three sections across the Gulf Stream, *J. Phys. Oceanogr.*, *19*, 36–51, 1989.

Lee, T. N., and D. A. Brooks, Initial observations of current, temperature and coastal sea level response to atmospheric and Gulf Stream forcing on the Georgia Shelf, *Geophys. Res. Lett.*, *6*, 321–324, 1979.

Lemoine, F., N. Pavlis, S. Kenyon, R. Rapp, E. Pavlis, and B. Chao, New high-resolution model developed for Earth's gravitational field, *Eos T. Am. Geophys. Un.*, *79*, 113–113, 1998.

Levitus, S., J. Antonov, and T. Boyer, Warming of the world ocean, 1955–2003, *Geophys. Res. Lett.*, *32*, L02604, 2005.

Li, X., and H. Götze, Ellipsoid, geoid, gravity, geodesy, and geophysics, *Geophysics*, *66*, 1660, 2001.

Loder, J. W., B. Petrie, and G. Gawarkiewicz, The coastal ocean off northeastern North America: A large-scale view, in *The Global Coastal Ocean: Regional Studies and Syntheses*, edited by K. H. Brink and A. R. Robinson, chap. 5, pp. 105–133, John Wiley & Sons, Inc., 1998.

Lozier, M., W. Owens, and R. Curry, The climatology of the North Atlantic, *Prog. Oceanogr.*, *36*, 1–44, 1995.

Lumpkin, R., and M. Pazos, *Lagrangian Analysis and Prediction of Coastal and Ocean Dynamics (LAPCOD)*, chap. 2, pp. 39–67, Cambridge University Press, Cambridge, UK, 2007.

Madec, G., P. Delecluse, M. Imbard, and C. Lèvy, *OPA 8.1 Ocean General Circulation Model Reference Manual*, no. 11 in Notes du Pôle de Modélisation, Institut Pierre Simon Laplace (IPSL), France, 1998.

Mann, C., The termination of the Gulf Stream and the beginning of the North Atlantic Current, *Deep-Sea Res.*, *14*, 337–359, 1967.

Maximenko, N., P. Niiler, L. Centurioni, M.-H. Rio, O. Melnichenko, D. Chambers, V. Zlotnicki, and B. Galperin, Mean dynamic topography of the ocean derived from satellite and drifting buoy data using three different techniques, *J. Atmos. Ocean. Tech.*, *26*, 1910–1919, 2009.

Meinen, C., D. Luther, and M. Baringer, Structure, transport and potential vorticity of the Gulf Stream at 68°W: Revisiting older data sets with new techniques, *Deep-Sea Res. Pt. 1*, *56*, 41–60, 2009.

Meinen, C. S., M. O. Baringer, and R. F. Garcia, Florida Current transport variability: An analysis of annual and longer-period signals, *Deep-Sea Res. Pt. 1*, *57*, 835–846, 2010.

Mesinger, F., et al., North American regional reanalysis, *Bull. Am. Meteorol. Soc.*, *87*, 343–360, 2006.

Montgomery, R., Fluctuations in monthly sea level on eastern U.S. coast as related to dynamics of western North Atlantic Ocean, *J. Mar. Res.*, *1*, 165–185, 1938.

Montgomery, R., Sea level difference between Key West and Miami, Florida, *J. Mar. Res.*, *4*, 32–37, 1941.

Myers, P. G., C. Donnelly, and M. H. Ribergaard, Structure and variability of the West Greenland Current in summer derived from 6 repeat standard sections, *Prog. Oceanogr.*, *80*, 93–112, 2009.

Mysak, L., and B. Hamon, Low-frequency sea level behavior and continental shelf waves off North Carolina, *J. Geophys. Res.*, *74*, 1397–1405, 1969.

Niiler, P., and J. Paduan, Wind-driven motions in the northeast Pacific as measured by Lagrangian drifters, *J. Phys. Oceanogr.*, *25*, 2819–2830, 1995.

Pail, R., et al., Combined satellite gravity field model GOCO01S derived from GOCE and GRACE, *Geophys. Res. Lett.*, *37*, L20314, 2010.

Pail, R., et al., First GOCE gravity field models derived by three different approaches, *J. Geod.*, *85*, 819–843, 2011.

Pavlis, N. K., S. A. Holmes, S. C. Kenyon, and J. K. Factor, The development and evaluation of the Earth Gravitational Model 2008 (EGM2008), *J. Geophys. Res.*, *117*, B04406, 2012.

Petit, G., and B. Luzum, IERS Conventions (2010), *Tech. Rep. IERS Technical Note No. 36*, International Earth Rotation and Reference Systems Service, 2010.

Rapp, R. H., and Y. M. Wang, Geoid undulation differences between geopotential models, *Surv. Geophys.*, *14*, 373–380, 1993.

Reid, J., On the total geostrophic circulation of the North Atlantic Ocean: Flow patterns, tracers, and transports, *Prog. Oceanogr.*, *33*, 1–92, 1994.

Reigber, C., R. Schmidt, F. Flechtner, R. König, U. Meyer, K. Neumayer, P. Schwintzer, and S. Zhu, An Earth gravity field model complete to degree and order 150 from GRACE: EIGEN-GRACE02S, *J. Geodyn.*, *39*, 1–10, 2005.

Reigber, C., et al., A high-quality global gravity field model from CHAMP GPS tracking data and accelerometry(EIGEN-1 S), *Geophys. Res. Lett.*, *29*, 1692, 2002.

Reigber, C., et al., *Earth Gravity Field and Seasonal Variability from CHAMP*, chap. I, pp. 25–30, Springer, 2004.

Reverdin, G., P. Niiler, and H. Valdimarsson, North Atlantic Ocean surface currents, *J. Geophys. Res.*, *108*, 3002, 2003.

Richardson, P., R. Cheney, and L. Worthington, A census of Gulf Stream rings, Spring 1975, *J. Geophys. Res.*, *83*, 6136–6144, 1978.

Ridgway, K., and J. Dunn, Using satellite altimetry to correct mean temperature and salinity fields derived from Argo floats in the ocean regions around Australia, *Deep-Sea Res. Pt. 1*, *57*, 1137–1151, 2010.

Rio, M. H., S. Guinehut, and G. Larnicol, New CNES-CLS09 global mean dynamic topography computed from the combination of GRACE data, altimetry, and in situ measurements, *J. Geophys. Res.*, *116*, C07018, 2011.

Roemmich, D., et al., Argo: The global array of profiling floats, in *Observing the Oceans in the 21st Century*, edited by C. Koblinsky and N. Smith, pp. 248–258, GODAE Project Office and Bureau of Meteorology, Melbourne, Australia, 2000.

Rossby, T., The North Atlantic Current and surrounding waters: At the crossroads, *Rev. Geophys.*, *34*, 463–481, 1996.

Rummel, R., G. Balmino, J. Johannessen, P. Visser, and P. Woodworth, Dedicated gravity field missions – principles and aims, *J. Geodyn.*, *33*, 3–20, 2002.

Rummel, R., M. Horwath, W. Yi, A. Albertella, W. Bosch, and R. Haagmans, GOCE, Satellite Gravimetry and Antarctic Mass Transports, *Surv. Geophys.*, *32*, 1–15, 2011.

Sandwell, D. T., and W. H. F. Smith, Global marine gravity from retracked Geosat and ERS-1 altimetry: Ridge segmentation versus spreading rate, *J. Geophys. Res.*, *114*, B01411, 2009.

Sarmiento, J. L., and K. Bryan, An ocean transport model for the North Atlantic, *J. Geophys. Res.*, *87*, 394–408, 1982.

Schmidt, S., and U. Send, Origin and composition of seasonal Labrador Sea freshwater, *J. Phys. Oceanogr.*, *37*, 1445–1454, 2007.

Smith, R. S., and J. M. Gregory, A study of the sensitivity of ocean overturning circulation and climate to freshwater input in different regions of the North Atlantic, *Geophys. Res. Lett.*, *36*, L15701, 2009.

Stommel, H., *The Gulf Stream: A Physical and Dynamical Description*, second edition ed., Univ of California Press, 1972.

Stouffer, R. J., et al., Investigating the causes of the response of the thermohaline circulation to past and future climate changes, *J. Clim.*, *19*, 1365–1387, 2006.

Sturges, W., Sea level slope along continental boundaries, *J. Geophys. Res.*, *79*, 825–830, 1974.

Sudre, J., and R. Morrow, Global surface currents: A high-resolution product for investigating ocean dynamics, *Ocean Dynam.*, *58*, 101–118, 2008.

Sutherland, D. A., and R. S. Pickart, The East Greenland Coastal Current: Structure, variability, and forcing, *Prog. Oceanogr.*, *78*, 58–77, 2008.

Sverdrup, H., M. Johnson, and R. Fleming, *The Oceans: Their Physics, Chemistry and General Biology*, Prentice-Hall, Englewood Cliffs, N.J., 1942.

Talley, L., G. Pickard, W. Emery, and J. Swift, *Descriptive Physical Oceanography: An Introduction*, sixth edition ed., Elsevier, 2011.

Tapley, B., S. Bettadpur, M. Watkins, and C. Reigber, The gravity recovery and climate experiment: Mission overview and early results, *Geophys. Res. Lett.*, *31*, L09607, 2004.

Tapley, B., et al., GGM02–An improved Earth gravity field model from GRACE, *J. Geod.*, *79*, 467–478, 2005.

Thompson, K., and E. Demirov, Skewness of sea level variability of the world's oceans, *J. Geophys. Res.*, *111*, C05005, 2006.

Thompson, K., D. Wright, Y. Lu, and E. Demirov, A simple method for reducing seasonal bias and drift in eddy resolving ocean models, *Ocean Modell.*, *13*, 109–125, 2006.

Thompson, K., J. Huang, M. Véronneau, D. Wright, and Y. Lu, The mean surface topography of the northwest Atlantic: Comparison of estimates based on satellite, terrestrial gravity, and oceanographic observations, *J. Geophys. Res.*, *114*, C07015, 2009.

Tseng, Y., and M. Chien, Parallel Domain-decomposed Taiwan Multi-scale Community Ocean Model (PD-TIMCOM), *Comput. Fluids*, *45*, 77–83, 2011.

Wang, Y., GSFC00 mean sea surface, gravity anomaly, and vertical gravity gradient from satellite altimeter data, *J. Geophys. Res.*, *106*, 31167–31174, 2001.

Wilkin, J. L., M. M. Bowen, and W. J. Emery, Mapping mesoscale currents by optimal interpolation of satellite radiometer and altimeter data, *Ocean Dynam.*, *52*, 95–103, 2002.

Willis, J., D. Roemmich, and B. Cornuelle, Combining altimetric height with broadscale profile data to estimate steric height, heat storage, subsurface temperature, and sea-surface temperature variability, *J. Geophys. Res.*, *108*, 3292, 2003.

Wunsch, C., Low frequency variability in the sea, in *Evolution of Physical Oceanography: Scientific Surveys in Honor of Henry Stommel*, edited by B. A. Warren and C. Wunsch, pp. 342–374, The MIT Press, 1981.

Wunsch, C., and D. Stammer, Satellite altimetry, the marine geoid and the oceanic general circulation, *Annu. Rev. Earth Pl. Sc.*, *26*, 219–253, 1998.

Wunsch, C., D. Hansen, and B. Zetler, Fluctuations of the Florida Current inferred from sea level records, *Deep-Sea Res.*, *16*, 447–470, 1969.

Yashayaev, I., Hydrographic changes in the Labrador Sea, 1960-2005, *Prog. Oceanogr.*, *73*, 242–276, 2007.

Yuan, D., Dynamics of the cold-water event off the southeast coast of the United States in the summer of 2003, *J. Phys. Oceanogr.*, *36*, 1912–1927, 2006.